

**ELECTROMAGNETIC BAND GAP RESONATOR ANTENNAS:
FROM NARROWBAND TO EXTREMELY WIDEBAND**

by

Raheel Maqsood Hashmi



MACQUARIE
University

Dissertation submitted in fulfilment of the requirements

for the degree of

DOCTOR OF PHILOSOPHY

Department of Engineering
Faculty of Science and Engineering
Macquarie University
Sydney, Australia

December 2015

Copyright © 2015 Raheel Maqsood Hashmi

All Rights Reserved

MACQUARIE UNIVERSITY

APPROVAL OF THE EXAMINATION PANEL

for a Dissertation submitted by

Raheel Maqsood Hashmi

This dissertation has been recommended by each member of the following committee as satisfactory for award of the degree.

Prof Karu Esselle

Principal Supervisor, Macquarie University, Australia

09/12/2015

Prof Anja Skrivervik

Ecole Polytechnique Federale de Lausanne (EPFL), Switzerland

01/10/2015

Dr Peter de Maagt

European Space Agency (ESA), The Netherlands

02/10/2015

Dr Alexandros Feresidis

University of Birmingham, United Kingdom

10/11/2015

ABSTRACT

This dissertation introduces several novel Electromagnetic band gap (EBG) resonator antennas (ERAs) that are designed to have wide directivity bandwidths as well as significantly reduced footprints. ERAs are well known for their simple configuration and high directivity, as compared to other complex and bulky alternatives. Antennas of this type find numerous applications in modern communication systems including point-to-point links, sensor systems, and electronic warfare. Although these highly directive antennas are very attractive for their simplicity, their applications are increasingly limited due to their inherent narrowband behavior and large footprint. This dissertation investigates several ERA designs, both numerically and experimentally, to achieve large bandwidths alongside high directivity and small footprint areas. Half power directivity bandwidths exceeding 50% with broadside directivity ranging between 15-20dBi were successfully achieved, thereby representing an improvement of nearly two orders of magnitude over the 1-3% directivity bandwidth of classical ERAs.

Initially, a novel method is proposed to design single-feed high-gain wideband ERAs. Axial permittivity gradient (APG) was introduced to multi-layer 1-D EBG superstructures composed of unprinted dielectric slabs, and the thicknesses of each of these slabs were optimised to achieve a wideband defect mode using the Defect Cavity Model (DCM). By further investigating the 1-D scattering response of this superstructure, it was revealed that simultaneous use of defect cavity model (DCM) and superstructure reflection model (SRM) is imperative

to predict wideband performance in ERAs, specially with bandwidths exceeding 15%. Following this approach, a prototype ERA designed with a single feed and superstructure area as small as $1.5 \times 1.5\lambda_0^2$ was designed. It demonstrates a measured 3-dB directivity bandwidth of 22% at a peak gain of 18.2 dBi. Further studying the truncation of this three-layered superstructure, an extremely compact ERA was designed with a footprint of only $1.7\lambda_0^2$. To the best of the author's knowledge, no other planar antenna with such a small footprint presents a broadside gain greater than 15 dBi with a matched 3dB gain-bandwidth exceeding 25%. This ERA has a measured average aperture efficiency of 90% within the 3dB directivity bandwidth.

In contrast to the multi-layer 1-D superstructures having APGs, single dielectric-layer superstrates having transverse permittivity gradient (TPG) are introduced and investigated to design wideband ERAs. A relationship between broadband directivity enhancement of TPG superstrates and their aperture-field phase uniformity is established to provide valuable insight into the underlying principle of operation. Prototype ERAs were fabricated and the measurements validated the concept. A measured 3dB directivity bandwidth of 52.9% is demonstrated with a measured directivity of 16.4 dBi for an ERA that has a very small total footprint area of $1.54\lambda_0^2$. This represents an increase of 90% over the previous best measured ERA directivity bandwidth of 28%.

While designing these wideband ERAs, the finiteness of the ERA superstructures is found to be a vital contributor to the DBP as well as the overall antenna performance. To systematically quantify these effects, detailed case studies were conducted using a single layer as well as a two-layer dielectric superstructure with uniform permittivity in single-feed ERAs. It is found that even without any special treatment of the superstructure, the finiteness of the superstructure strongly

influences the DBPs. In particular, intriguing cases are observed when the dielectric layers in the two-layer superstructure are truncated to different finite sizes. Conventionally, although smaller superstructures yield wider bandwidths with reduced directivity, the truncation of superstructure layers to different finite sizes yielded more than 65% enhancement in the DBP, experimentally, while resorting to the same physical footprint. The detailed empirical relationships between the peak directivity, bandwidth, and the finiteness of the superstructure layers provide valuable physical insight into the operation of superstructures that have non-uniform reflection and transmission profiles, similar to the TPG superstrate.

STATEMENT OF CANDIDATE

I certify that the work in this dissertation has not previously been submitted for a degree nor has it been submitted as part of the requirements for a degree to any other university or institution other than Macquarie University. I also certify that the dissertation is an original piece of research and it has been written by me. In addition, I certify that all information sources and literature used are indicated in the dissertation.

..... Raheel Maqsood Hashmi

ACKNOWLEDGMENTS

Reverence to the Almighty for his never ending blessings upon myself. Special thanks to my principal supervisor, Prof. Karu Esselle, for supporting and guiding me throughout the duration of my candidature. Without his unconditional dedication, support and guidance, this dissertation would not have been possible. He is undoubtedly one of the best scholars, teachers, and persons I have ever had the honor of meeting and working with. Thanks to my family for their support, to all my friends, to all my teachers, and of course to my colleagues who contributed directly or indirectly to my research.

I would like to express my gratitude to the *Commonwealth of Australia* and *Macquarie University* for honouring me with the prestigious International Postgraduate Research Scholarship (IPRS No. 2012003); to the *Astronomy and Space Science Division of CSIRO, Australia* for the Office of Chief Executive Fellowship (N01759); to Dr. Stuart Hay, my adjunct supervisor from *CSIRO Computational Informatics* for his useful advice; to Prof. Filippo Capolino for hosting me in his research group at the Henry Samueli School of Engineering, during my stay at *University of California (Irvine), Los Angeles, USA*; to Prof. Ladislau Matekovits for hosting me at Department of Electronics and Telecommunications, *Politecnico di Torino, Turin, Italy*; and of course to Dr. Frank Demming for his fantastic support from *CST, Germany*. Thanks are in order to Dr. Carl Svensson, my friend and colleague, who helped me in various ways to compile and organize this dissertation. I would also like to acknowledge the support of *Rogers Incorporated*,

USA which provided some of the dielectric materials used in the experiments.

And last but not the least, a big thanks to Macquarie University for awarding me the fellowships that brought me to Sydney (NSW, Australia), a truly amazing city, and for awarding me the travel grants which allowed me to go around the world to present my research at these conferences: *ASA 2013* (NSW, Australia), *iWAT 2013* (NSW, Australia), *AP-S 2014* (TN, USA), *ANTEM 2014* (BC, Canada), *EuCAP 2015* (Lisbon, Portugal), *ASA 2015* (NSW, Australia), and to visit these institutions: *University of California (Irvine), USA* and *Politecnico di Torino (Turin), Italy*. In addition, this allowed me to visit some of the most astounding places around the globe including the Golden Gate Bridge (San Francisco, California), the Mississippi River (Memphis, Tennessee), Hollywood & the Universal Studios (Los Angeles, California), the Disney Land (Anaheim, California), Long Beach (Costa Mesa, California), Houston (Texas), Vancouver (British Columbia), Sidney (Canada), the Empress (Victoria Harbour, Canada), sail through Straits of Juan de Fuca and Haro (Washington, USA & British Columbia, Canada), Hieronymites Monastery (Lisbon, Portugal), the 25 de Abril Bridge (Almada, Portugal), Piazza del Duomo (Milan, Italy), Corso Buenos Aires & San Babila (Milan, Italy), the Vasco de Gama Bridge (Portugal), and the Mole Antonelliana (Turin, Italy).

To my loving wife, my naughty brothers, and our most amazing parents.

Contents

Table of Contents	xix
List of Figures	xxv
List of Tables	xxxv
1 Introduction	1
1.1 Overview	1
1.2 Challenges and Objectives	3
1.3 Main Contributions	5
1.4 Organization	6
1.5 Author's Contribution	8
1.6 Dissertation Outline	8
2 Background	11
2.1 Periodic Structures	11
2.2 EBG Resonator Antennas	13
2.3 Superstructure Types	16
2.3.1 Unprinted Superstructures	16
2.3.2 Printed Superstructures	18
2.4 Analytical Models	20

2.4.1	Ray-Tracing Approximation	20
2.4.2	EBG Defect Model	23
2.4.3	Transmission Line Model	26
2.4.4	Leaky-wave Model	27
2.5	Periodic Analysis: Unit-Cell Models	30
2.5.1	Superstrate Reflection Model (SRM)	30
2.5.2	Defect Cavity Model (DCM)	32
2.5.3	Limitations of Periodic Analysis	34
2.6	Directivity Bandwidth and Footprint	35
2.7	Composite Antenna Design	36
2.8	Reviewing the Literature on ERA Bandwidth Enhancement	40
2.8.1	Multi-layer Printed PRS-based ERAs	41
2.8.2	Variable Reflection Profile and Metamaterial-based ERAs	42
2.8.3	Multi-point Array-Fed ERAs	43
2.8.4	Complementary FSS-based ERAs	44
2.9	Potential Applications	46
2.10	Summary of Proposed Designs	48
3	Wideband ERAs with Multi-layer Dielectric Superstructures	51
3.1	Abstract	51
3.2	Introduction	52
3.3	Theoretical Basis and Unit-Cell Characterization	56
3.3.1	Forming a Wide Defect-Mode Cavity Resonator	57
3.3.2	Evaluating Feasibility as Antenna Superstrate	58
3.3.3	Inclusion Layer and Formation of S-II	60
3.4	Wideband ERA Design	60
3.4.1	Choice of the Permittivity Combinations	62

3.4.2	Superstructure Area and Directivity Bandwidth	64
3.4.3	Feed Antenna and Input Matching	66
3.5	Measurements and Results	66
3.5.1	Input Impedance Matching	68
3.5.2	Measured Directivity and ERA Gain	68
3.5.3	Radiation Patterns	72
3.6	Conclusion	72
4	Defect-Mode Superstructures for Wideband ERAs	75
4.1	Abstract	75
4.2	Introduction	76
4.3	Defect-Mode EBG Structures	79
4.3.1	Classical ERAs and Pattern Bandwidths	79
4.3.2	Unit-Cell Configuration	80
4.3.3	Design of Defect-Mode Structures	80
4.4	Antenna Design and Fabrication	82
4.5	Results and Discussion	86
4.6	Conclusion	88
5	Wideband ERAs with Dielectric Superstructures having Transverse Permittivity Gradients	91
5.1	Abstract	91
5.2	Introduction	92
5.3	STPG Configuration and Advantage	95
5.3.1	STPG and ERA Configurations	95
5.3.2	Transverse Reflectivity Variation	97
5.3.3	STPG vs. Uniform Superstrates	98

5.4	Superstrate Design	100
5.4.1	Effect of Quantization	100
5.4.2	Superstrate Thickness	102
5.5	Phase Distribution and Directivity Bandwidth	102
5.6	Prototype Design and Test Results	107
5.6.1	Design of ERAs with Feed Antenna	108
5.6.2	Prototype Construction	110
5.6.3	Measured Directivity and Gain	110
5.6.4	Radiation Patterns	113
5.6.5	Input Matching	114
5.7	Differentiating ERAs with STPG from Lens-based Antennas	116
5.7.1	Principle of Operation	116
5.7.2	Size and Bandwidth	116
5.7.3	Design Method	117
5.7.4	Feeding Technique	117
5.8	Conclusion	119
6	High Aperture Efficiency Wideband ERAs	121
6.1	Abstract	121
6.2	Introduction	122
6.3	ERA Design and Configuration	123
6.4	Numerical and Experimental Results	125
6.5	Discussion	129
6.6	Conclusion	131
7	Arrays of High Aperture Efficiency Wideband ERAs	133
7.1	Abstract	133

7.2	Introduction	134
7.3	Configuration of Antennas	135
7.4	Numerical Results	136
7.5	Discussion	138
7.6	Conclusion	140
8	Investigation into the Effects of Superstructure Finiteness in ERAs	141
8.1	Abstract	141
8.2	Introduction	142
8.3	Highly Reflective 1-D Dielectric Superstructure	144
8.3.1	Superstructure Characterization	145
8.3.2	Analytical Predictions	147
8.4	Effects of Superstructure Finiteness	147
8.4.1	Equal Area of Superstructure Layers	148
8.4.2	Unequal Area of Superstructure Layers	149
8.5	Experimental Results	152
8.6	Conclusion	158
9	Effective Truncation of Superstructures in ERAs	161
9.1	Abstract	161
9.2	Introduction	162
9.3	Aperture Size and Directivity-Bandwidth	163
9.4	Full-Wave Analyses	166
9.5	Results and Discussion	167
9.6	Conclusion	171
10	Conclusions and Future Work	173
10.1	Conclusions	173

10.2 Future Work	176
A Research Outcomes	179
A.1 Patent Applications	179
A.2 List of Publications	179
A.2.1 Journal Articles	180
A.2.2 Invited Articles	180
A.2.3 Conference Articles	181
B List of Acronyms	183
Bibliography	185

List of Figures

2.1	Block examples of (a) one-, (b) two- and (c) three-dimensional electromagnetic band gap structures [16].	13
2.2	The general structure of an EBG resonator antenna showing a metallic ground plane, a symbolic superstructure, and an example feed source. In EBG analysis, the superstructure is often characterized by its scattering profile which will be discussed thoroughly in Section 2.5.	14
2.3	Examples of ERAs with 1-D, 2-D and 3-D superstructures: (a) classical 1-D EBG superstructure made by 3 dielectric layers [8], (b) “defected” 1-D EBG structure [10], (c) multi-layer 2-D FSS superstructure [9], (d) single layer thin 2-D FSS superstructure [12], (e) 3-D woodpile EBG superstructure [41], (f) truncated 3-D woodpile EBG structure [7].	17
2.4	Conceptual model of the antenna proposed in [5] (a) The ray-tracing diagram of the Fabry-Perot type cavity formed between the PRS and the ground plane, (b) structural view of the proposed antenna.	21
2.5	Simple EBG structure made out of stack of dielectric layers (a) 3 layer EBG structure, each layer is quarter guided-wavelength thick ($d_1 = \lambda_0/(4\sqrt{\epsilon_{r1}})$) and spaced quarter free-space wavelength apart ($h_1 = \lambda_0/4$), (b) The same EBG structure with defect, the upper and lower half of the structure are dual in nature and have an image plane in the centre [86].	24

2.6	Band gap obtained with a 6 layer 1-D EBG structure in [8]. The defect-mode obtained by disturbing the periodicity is also shown here.	25
2.7	The transverse equivalent network model of an ERA derived from [90] (a) when fed using an electric dipole in the middle of the cavity at distance h_s , and (b) fed by a magnetic dipole (slot) on the ground plane of the antenna.	26
2.8	Circuit elements used to model the FSS that are implemented using (a) slots printed on a substrate, (b) patches printed on a substrate, (c) patches and slots printed above and below the substrate, and (d) reciprocal case of (c).	26
2.9	The leaky wave antenna model: (a) Multilayered LWA geometry with dipole excitation. The incident angle measured from the normal axis is $\theta_p = 0$ for broadside radiation (b) Steepest descent path corresponding to time dependence $e^{j\omega t}$. Saddle-point is present at $\xi = 0$ on real axis, and an example is given of leaky-wave pole and surface-wave pole captured by deformation from original path Γ to steepest descent path [39].	28
2.10	Unit-cell models used for computing 1D scattering from the periodic structures (a) superstructure reflection model, and (b) defect cavity model [81].	31
2.11	(a) Reflection phase computed using SRM showing an inverted phase gradient, calculated ideal phase for directivity enhancement over wideband is also shown, and (b) Band gap calculated using the DCM as well as the defected band gap are shown [96].	33
2.12	Computed peak directivity of two ERAs for increasing footprint area. The superstructures considered for these computations are square and aperture width denoted by λ_0 is the length of one side of the superstructure (a) 1-D EBG structure [8] and (b) 3-D woodpile EBG structure [7]	37

2.13	Peak broadside directivity computed as a function of size of the superstrate layers by varying L_2 from $1\lambda \times 1\lambda$ to $6\lambda \times 6\lambda$. The directivity of classical ERA with equally truncated layers is also plotted for reference.	38
2.14	Comparison of 3dB bandwidth of the classical 2-layer ERA with unequally truncated layer ERA. For the latter, L_1 and L_2 truncated to $3\lambda_0 \times 3\lambda_0$ and $4\lambda_0 \times 4\lambda_0$, respectively [98].	40
3.1	Unit cell models of the proposed S-II wide defect-mode EBG Structure (a) defect cavity model (DCM) to calculate transmission ($ \tau_{DCM} $) through the structure (b) superstructure reflection model (SRM) to characterize the reflection profile ($ \Gamma_{SRM} , \angle\Gamma_{SRM}$). Inter-slab spacing h_1 and h_2 are set to quarter-wavelength.	55
3.2	Transmission of (a) a classical EBG structure that consists of four identical dielectric slabs ($\epsilon_1 = \epsilon_2 = 9.2, t = 0.25\lambda_g, h_1 = 0.25\lambda_0, 2h = 0.25\lambda_0$ i.e. no defect), (b) DCM of a narrowband periodicity defect structure ($\epsilon_1 = \epsilon_2 = 9.2, t = 0.25\lambda_g, h_1 = 0.25\lambda_0, h = 0.5\lambda_0$) and (c) DCM of a wideband defect-mode structure ($\epsilon_1 = \epsilon_2 = 9.2, t = 0.5\lambda_g, h_1 = 0.25\lambda_0, h = 0.5\lambda_0$) $f_0 = 11.1$ GHz.	56
3.3	Effects of permittivity and thickness variation on $\angle\Gamma_{SRM}$. The curves are obtained through SRM with $h = 0.5\lambda_0$ and $h_1 = 0.4\lambda_0$. Initial parameters are $\epsilon_1 = \epsilon_2 = 9.2$ and $t_1 = t_2 = 0.36\lambda_g$. Then either t_2 or ϵ_2 is changed to the value shown in the legend.	58
3.4	Reflection ($ \Gamma_{SRM} $) and transmission ($ \tau_{DCM} $) obtained by SRM and DCM. The curves are obtained for different values of separation h_1 between slabs L_1 and L_2 with $t_1 = t_2 = 0.36\lambda_0, \epsilon_1 = 9.2, \epsilon_2 = 9.8, 2h = \lambda_0$	59

3.5	Reflection ($ \Gamma_{SRM} $) and transmission ($ \tau_{DCM} $) magnitude with the third slab in the superstructure, computed using SRM and DCM for various gaps h_2 . L_1, L_2 and L_3 parameters: $\epsilon_1 = 9.2$, $\epsilon_2 = 4.5$, $\epsilon_3 = 9.8$, $t_1 = 0.26\lambda_g$, $t_2 = 0.36\lambda_g$, $t_3 = 0.26\lambda_g$, $h_1 = \lambda_0/4$, $2h = \lambda_0$	61
3.6	Predicted boresight directivity and side lobe level (SLL) for Case-I and Case-II antenna superstructures truncated to $1.5 \times 1.5\lambda_0^2$. The superstructures have additional $10 \times 10 \text{ mm}^2$ extensions on each edge to place nylon spacers, as shown in Fig. 6.1.	62
3.7	Predicted boresight directivity for various superstructure areas of an ERA with S-II (Case-II) superstructure, without extensions.	63
3.8	The computed input reflection coefficients of the waveguide-fed slot antenna with various superstructures are compared with that of the radiating slot without a superstructure.	65
3.9	Prototype of the compact wideband ERA which has a superstructure area of only $1.5\lambda_0 \times 1.5\lambda_0$. A waveguide-to-coax connector is used to feed the antenna (a) top view (b) side view	67
3.10	Measured VSWR of the prototype ERA with a single slot feed compared with the predicted VSWR.	68
3.11	Measured gain and directivity of the fabricated ERA prototype, compared with the gain predicted from full-wave simulation. The area of aluminum ground plane is $75 \times 75 \text{ mm}^2$	70
3.12	Measured radiation patterns of the proposed ERA at (a) $f=11.0 \text{ GHz}$ (b) $f=11.8 \text{ GHz}$ (c) $f=12.6 \text{ GHz}$ (d) $f=13.4 \text{ GHz}$	71

4.1	Defect cavity model (DCM) unit cell and Superstructure reflection model (SRM) unit cell of the two wide defect-mode EBG Structures: S-I and S-II (a) DCM of S-I, with image slabs (b) SRM of S-I (c) DCM of S-II, with image slabs (d) SRM of S-II.	78
4.2	Transmission through the defect cavity model for both superstructure types.	82
4.3	Prototypes of the ERAs designed with S-I and S-II. Both ERAs are fed using a waveguide-to-coax adaptor: top view of ERA_{S-I} with superstructure consisting of two dielectric layers (left) and ERA_{S-II} with superstructure consisting of three dielectric layers, during measurement at the AusAMF. .	83
4.4	Measured broadside directivity of the two ERA prototypes.	85
4.5	Broadside directivity of ERA_{S-I} is compared with the reflection coefficient magnitude of the DCM to show the self-resonance within the EBG structure and its effect in reducing the pattern bandwidth.	86
4.6	Measured input reflection coefficient for both antenna prototypes demonstrating wideband impedance matching covering the entire pattern bandwidths.	87
4.7	Measured radiation patterns of the proposed ERA_{S-I}	89
5.1	(a) Example configuration of a STPG with top view (i.e. xy -plane) and cross-sectional view (i.e. xz -plane) (b) Example configuration of an ERA with a STPG. Design parameters such as permittivity values ($\epsilon_1 \dots \epsilon_n$), segment widths ($w_1 \dots w_n$), STPG radius R , and slab thickness t are also shown.	96
5.2	Reflection magnitudes of three uniform dielectric slabs. In the insert, transverse reflection and transmission profiles are shown symbolically for the case when these three materials are combined to form a STPG.	97

5.3	Broadside directivity of an ERA with a finely-quantized STPG ($N = 9$) is compared with the broadside directivity of three ERAs with uniform superstrates made out of different materials. The relative permittivity values of STPG are $\{\epsilon_1, \epsilon_2, \dots, \epsilon_9\} = \{10, 9, \dots, 2\}$; segment widths are $w_1 = 4mm$, $w_2, \dots, w_9 = 2.875mm$. the 3dB directivity band for the STPG case is shaded.	99
5.4	Phase distribution for a STPG: (a) above the STPG (b) within the cavity. STPG parameters are: $N = 5$, $\{\epsilon_1, \epsilon_2, \epsilon_3, \epsilon_4, \epsilon_5\} = \{10, 8, 6, 4, 2\}$, $w_1 = 6.87mm$, $\{w_2, w_3, w_4\} = 5.75mm$, and $w_5 = 2.875mm$, $R = \lambda_0$, $t = 0.5\lambda_0/\sqrt{\epsilon_1}$, $h = 0.5\lambda_0$ where $\lambda_0 = 27mm$	105
5.5	Phase distribution for a uniform superstrate: (a) above the superstrate (b) within the cavity . Superstrate parameters are: $N = 1$, $\epsilon_r = 10$, $R = \lambda_0$, $t = 0.5\lambda_0/\sqrt{\epsilon_r}$	106
5.6	Computed directivity and realized gain of the circular ERA. The cavity is excited using a waveguide-fed slot.	108
5.7	Photographs of the prototype ERAs (a) side view of the ERA with circular STPG showing the feed slot and WR-75 waveguide (b) top view of the ERA with circular STPG (c) side view of the ERA with square STPG showing the waveguide adaptor with SMA-to-coax transition; notice the larger ground plane (ground plane size: $75mm \times 75mm$) (d) top view of the ERA with square STPG.	109
5.8	Measured directivity and gain of the ERAs (a) Square ERA (b) Circular ERA. The measurements were carried out in the NSI-700S-50 spherical near-field chamber at the Australian Antenna Measurement Facility (AusAMF).	111

5.9	Normalised radiation patterns of the square ERA at a six equally spaced frequencies.	112
5.10	<i>E</i> -plane patterns of the ERA proposed in [71] with a larger footprint and fine TPG to achieve low SLL performance. The peak directivity of this ERA is 17.6 dBi.	114
5.11	Measured input reflection coefficient ($ S_{11} $) of both ERA prototypes. The input reflection coefficient was measured by an Agilent PNA-X N5242A vector network analyser.	115
6.1	Fabricated prototype of the antenna (a) configuration of antenna, and (b) bottom view of antenna showing the feeding slot in ground plane.	123
6.2	Measured directivity and gain of the antenna. The simulated gain of the slot without the ERA superstructure is also shown.	127
6.3	Measured and computed input reflection coefficient of the antenna.	127
6.4	Measured radiation patterns of the antenna	128
7.1	The 2×2 array high- η_{ap} ERAs. The spacing between the elements is designated by D . The physical footprint of the array assembly is marked by dashed lines.	136
7.2	An multi-point excitation ERA. The cavity is excited by an array of slot antennas. The CSS has a footprint of $3.8\lambda_0 \times 3.8\lambda_0$ and the spacing between the slots is $D = 0.5\lambda_0$	137
7.3	Broadside directivity of the high- η_{ap} ERA array shown in Fig. 7.1 for two different configurations. The broadside directivity of a single ERA is also shown for reference.	138

7.4	Broadside directivity of the multi-point excitation ERA shown in Fig. 7.2 when a single feed was used, compared with the case when array excitation was used.	139
8.1	Configuration of a typical ERA with a two layer superstructure: (a) side view of the ERA formed by employing the highly reflective 1D superstructure (b) plane-wave model of the two-layer superstructure used to compute reflection characteristics.	145
8.2	Complex reflection coefficient of the superstructure shown in Fig. 8.1 when only L_1 and L_2 are considered individually, and when both L_1 and L_2 are considered together (a) reflection magnitude (b) reflection phase.	146
8.3	Comparing the variation in (a) peak directivity and (b) the directivity bandwidth with the change in footprint for a one- and two-layer superstructure (L_1 and L_2 are assumed to be made out of FR-4, $\epsilon_r = 4.3$). . . .	148
8.4	Variation in (a) peak directivity and (b) 3dB directivity bandwidth computed using the ERA model shown in Fig. 8.1 for various sizes of L_2 , whereas the size of L_1 was fixed to the values shown in the figure (antenna parameters used are: $h_1 = 12.5mm$, $h_2 = 6.25mm$, $t = \lambda_0/\sqrt{\epsilon_r}$ where $\epsilon_r = 4.3$ and $\lambda_0 = 25mm$).	150
8.5	Variation in (a) peak directivity and (b) directivity bandwidth computed using the ERA model shown in Fig. 8.1 for various sizes of L_1 , whereas the size of L_2 was fixed to the values shown in the figure (antenna parameters used are: $h_1 = 12.5mm$, $h_2 = 6.25mm$, $t = \lambda_0/\sqrt{\epsilon_r}$ where $\epsilon_r = 4.3$ and $\lambda_0 = 25mm$).	151

8.6	Prototypes for experimental validation (a) ERA-I (feed slot dimensions: $10.88mm \times 7.9mm$), (b) ERA-II (feed slot dimensions: $11.95mm \times 5.88mm$), (c) ERA-III (feed slot dimensions: $11.95mm \times 5.88mm$), and (d) Waveguide-to-coax adapter with SMA transition (WR75 grade).	153
8.7	Measured reflection coefficient for the three ERA prototypes.	154
8.8	Measured broadside directivity and gain of the ERA prototypes.	155
8.9	E- and H-plane patterns of ERA-I within the 3dB bandwidth.	156
8.10	E- and H-plane patterns of ERA-II within the 3dB bandwidth.	156
8.11	E- and H-plane patterns of ERA-III within the 3dB bandwidth.	157
9.1	Basic ERA with an EBG superstructure composed of dual dielectric slabs with equal permittivity ($\epsilon_r = 9.2$) and thickness ($t = \lambda_g/4$) at $f_0 = 11.5$ GHz.	164
9.2	Fig. 2. E-field shown for horizontal and vertical cuts for the ERA shown in Fig. 9.1 for two aperture sizes at $f_0 = 11.5GHz$ (a) Top view for aperture size $2\lambda_0 \times 2\lambda_0$ (b) Top View for $6\lambda_0 \times 6\lambda_0$ (c) vertical cross section for $2\lambda_0 \times 2\lambda_0$ (d) vertical cross section for $6\lambda_0 \times 6\lambda_0$	165
9.3	Peak directivity of ERA for various aperture sizes of the EBG superstructure. Peak directivity of some designs proposed for HPDB enhancement are also plotted for comparison.	167
9.4	Fig. 4. Computed HPDB of ERA for various aperture sizes of EBG superstructure compared to some key designs proposed for bandwidth enhancement. Note the consistency between results of ERA in Fig. 9.1 and 3 layer all-dielectric ERA when the superstructure size is $6\lambda_0 \times 6\lambda_0$	168
9.5	Percentage HPDB versus peak directivity, computed for the ERA shown in Fig. 1.	169

List of Tables

2.1	Quantitative summary of bandwidth enhancement of ERAs in the last decade.	45
2.2	Summary of some wideband designs proposed in this dissertation.	49
3.1	Design parameters for Case-I and Case-II	64
3.2	Summary of measured performance of the wideband ERA at four frequencies.	69
4.1	Summary of measured performance of the wideband ERAs.	84
5.1	Effect of STPG quantization level on antenna performance.	101
5.2	Effect of varying superstrate thickness “ t ” on directivity-bandwidth product of an ERA with STPG.	103
5.3	Comparison of effective in-phase radius ($\Delta\phi \leq 90^\circ$), as a fraction of superstrate radius, of STPG and uniform superstrates.	107
5.4	Differentiating proposed ERAs from lens-based antennas.	118
6.1	Thickness and relative permittivity of the dielectric layers in the superstrate	124
6.2	Comparison of measured performance parameters of the antenna.	126
6.3	Comparison of figures of merit	130
8.1	Comparison of experimental data for the three prototype ERAs.	157

Chapter 1

Introduction

1.1 Overview

With the rise of wireless technology dominating the consumer market in recent years, bandwidth-hungry wireless applications such as high definition video streaming, in-flight internet access via satellite, and delocalized cloud data access, have grown tremendously. To cope up with this heavy demand for broadband wireless communication, simple and efficient directive antennas have become a prime focus of research. Directive antennas have numerous applications in modern communication systems including point-to-point links, backhaul systems, sensor systems, and electronic warfare. Electromagnetic band gap (EBG) resonator antenna (ERA) is a class of highly directive antennas well known for its simple configuration. Antenna arrays present high design complexity and expensive feeding networks whereas the reflectors, owing to their bulky nature, are often constrained by deployment geographies (urban and extra-urban environments) as well as topological aesthetics. In contrast, ERAs have the potential to offer highly directive radiation with a single feed source, and often have planar, low-profile characteristics.

A common ERA consists of an air-filled cavity formed between a perfect reflector

(e.g. metallic ground plane or Artificial Magnetic Conductor (AMC)) and a partially reflecting superstrate (PRS). This forms a Fabry-Perot type cavity that is excited by one or several small antennas such as slots. Despite the highly directive characteristics, the bandwidth of conventional ERAs is very narrow (1-3%), and this poses a major limitation on their use in various practical applications. The bandwidth of operation (commonly referred as ‘directivity bandwidth’) is designated as the continuous range of frequency where the directivity of the ERA lies within 3dB of the peak directivity. This is an essential requirement to characterize directive wideband antennas. Moreover, ERAs also suffer from low aperture efficiencies due to their excessively large footprints often ranging between $20 - 36\lambda_0^2$, which is, at present, another major limiting factor.

Since the early 1990s, ERAs have been studied analytically. However, practical designs and experiments largely began in the last decade as ERAs became the research focus of both academia and industry, as low-profile high-gain radiating structures. They have potential applications ranging from local multi-point distribution systems (LMDS) and satellite reception, to high-speed mm-wave wireless local area networks (WLANs). A particularly interesting application of ERAs is in concerns where planar characteristics allow for reduced radar cross-section signature¹. They can also be used as interleaved feeds in the focal array-fed reflector (FAFR) antennas. Multi-beam FAFRs are indispensable for defence, satellite, and radio astronomy applications where efficient illumination of the reflector is desired for various beam orientations alongside a low rollover between multiple beams. More recently, these planar antennas have been viewed as potential candidates for broadband last-mile access, wireless backhaul and mm-wave applications. Therefore, it is imperative to explore methods to design ERAs that offer high gain and wide bandwidths with minimal footprints, without compromising their simple configurations and low-profile

¹In 2012-13, the first ever Ka-band satellite transmit/receive link using metamaterial based ERA technology was demonstrated [1-3]

nature. However, it should be remarked that the ERAs proposed in this dissertation are not meant to replace the conventional high gain antennas such as reflectors, lens antennas, and antenna arrays. Instead, they serve as a convenient alternative, especially in space-constrained applications where robustness, performance, and aesthetic appeal are equally important.

1.2 Challenges and Objectives

ERAs are well-known for their bandwidth limited behavior. Unlike most antennas that are restricted by their impedance bandwidth, ERAs are often limited by their half power directivity bandwidth (3dB directivity bandwidth) and of course, their half power gain bandwidth (3dB gain bandwidth). In most classical ERAs, the directivity bandwidth ranges between 1-3% [4–8]. In the past, various efforts were made in this challenging research subject. Yet for peak antenna directivity exceeding 15 dBi, the figures for directivity bandwidth rest at around 15% [9–14]. One method is to achieve wideband cavity resonance by adding resonant layers in the superstructure². In this case, arrays of metallic patterns are printed on dielectric layers to achieve closely spaced resonant frequencies that combine together to form a single wide band of operation. But the size of these arrays often needs to be amply large to create a well-illuminated aperture to obtain high directivity. Thus, the footprint of these arrays is rather large ($\approx 25\lambda_0^2$) and the resultant aperture efficiency of the antenna is quite low. Moreover, inherent self-resonances associated with printed arrays have been found to limit the maximum obtainable directivity. Another method is to use a multilayered wideband superstructure in combination with array feeding. However, two of the most desirable aspects of ERAs, i.e. the benefit of single feed and simple configuration are lost. Also, each added layer in the superstructure increases the

²Superstructure is a more general term that encompasses superstrates that have one or more layers.

profile of the antenna and thus limits the bandwidth potential of the antenna. Therefore, despite being challenging, it is intriguing to explore methods for designing ERAs that demonstrate high directivity as well as significantly improved directivity bandwidths.

Another major issue relating to ERAs is their large footprint³. ERAs are often designed and analyzed using periodic analysis: a simplified process to extract a scattering profile of superstructures that assumes infinite transverse extent. Truncation of the superstructure to a finite size is a decision that is often made towards the end of the ERA design life cycle. In addition, it has been observed in the past that peak directivity increases by increasing the ERA footprint, whereas bandwidth decreases. Thus, to adhere to the predictions of periodic analysis and to achieve high directivity, the superstructures of ERAs are large in size and this leads to large antenna footprints.

In this dissertation, the emphasis is on improving the directivity bandwidth of ERAs while maintaining sufficiently high directivity, and on minimizing the complexity of design while trying to do so. For this purpose, limitations surrounding the use of periodic analysis for wideband ERA design are highlighted. Novel wideband ERAs that benefit from axial and transverse permittivity gradient superstructures are proposed and thoroughly studied. Various superstructures are characterized by studying their behavior in detail. Rigorous studies are conducted using both numerical techniques and experiments. The possibility of constructing wideband, high-directivity ERAs that have very small footprints is practically demonstrated. Moreover, this dissertation aims to understand how the finiteness of superstructure affects the antenna's directivity bandwidth? and, if the field diffracted from the edges of the finite superstructure can improve the performance of the resulting ERAs? In addition, guidelines to decide on superstructure size in ERAs are developed to assist their general design.

³footprint is defined as the lateral area an antenna occupies.

1.3 Main Contributions

In this dissertation, various novel ERAs have been designed to achieve wide directivity bandwidths as well as significantly reduced footprints. Half power directivity bandwidths exceeding 50% with broadside directivity ranging between 15-20 dBi have been successfully demonstrated, thereby representing an improvement of nearly two orders of magnitude compared to classical single-feed ERAs [4–8]. For a peak directivity greater than 15 dBi, the figure for bandwidth of single-feed ERAs now exceeds 50%, which was previously approximately 15%. Moreover, the following are some of the key scientific contributions:

- Simple methods for creating wide defect-modes with only two layers of dielectric structures considering commercially available material thicknesses.
- Equivalence between thickness contrast and permittivity contrast for dielectric defect-mode superstructures.
- Simultaneous use of defect cavity model (DCM) and superstructure reflection model (SRM) to predict wideband performance in ERAs.
- Multilayered dielectric superstructures with wide defect-mode and significantly truncated lateral sizes.
- Dielectric superstructures having transverse permittivity gradients (TPG) for extremely wideband ERAs.
- Thorough characterization of TPG superstructures with methods to increase directivity-bandwidth products up to 4000.
- Composite superstructures where peak directivity is nearly unaffected by the varying its size.

- ERAs with significantly truncated superstructures featuring reductions of $>90\%$ compared to classical designs.
- Systematic empirical studies on superstructure finiteness and its effects on bandwidth and directivity of ERAs.
- ERAs with high radiation and total efficiencies with average values exceeding 85% within the respective directivity bandwidths.
- ERAs with significantly high aperture efficiency approaching mean value of 90% within the directivity bandwidths.
- An ERA prototype⁴ with peak measured gain of 15.6 dBi and an excellent measured 3dB gain-bandwidth of 27%, yet with a total footprint of only $1.7\lambda_0^2$.

1.4 Organization

This dissertation follows the non-traditional “Thesis-by-Publication” format which has been approved by *Macquarie University Higher Degree Research Office*. It consists of a general introduction, background, and the following list of my major scientific publications. The thesis materials are original texts and graphics of my publications, published or in review, that have been reformatted to improve readability. In addition to these major publications, a complete list of publications that resulted from my PhD research is included in Appendix A, which lists patent applications and articles containing associated auxiliary contributions.

1. R.M. Hashmi, B.A. Zeb and K.P. Esselle, “Wideband high-gain EBG resonator antennas with a small footprints and all-dielectric superstructures,” *IEEE Transac-*

⁴To the best of the author’s knowledge, no other planar antenna with such a small footprint presents a broadside gain greater than 15 dBi with a matched 3dB gain-bandwidth exceeding 25% [15].

- tions on Antennas and Propagation*, vol. 62, no. 6, pp. 2970-2977, 2014.
2. R.M. Hashmi, B.A. Zeb, and K.P. Esselle, "Composite defect-mode superstructures and wideband EBG resonator antennas," *9th European Conference on Antennas and Propagation (EuCAP)*, Lisbon, Portugal, 12-17 April, 2015.
 3. R.M. Hashmi and K.P. Esselle, "A class of extremely wideband resonant cavity antennas with large directivity-bandwidth products," *IEEE Transactions on Antennas and Propagation*, accepted in December 2015 (*in press*).
 4. R.M. Hashmi, and K.P. Esselle, "A wideband EBG resonator antenna with an extremely small footprint area," *Microwave and Optical Technology Letters*, vol. 57, no. 7, pp. 1531-1535, 2015.
 5. R.M. Hashmi, and K.P. Esselle, "Arrays of high aperture efficiency wideband EBG resonator antennas," (Invited Paper), *17th International Conference on Electromagnetics in Advanced Applications (ICEAA)*, Turin, Italy, 7-11 September, 2015.
 6. R.M. Hashmi and K.P. Esselle, "Enhancing performance of EBG resonator antennas by individually truncating superstructure layers," *Microwaves, Antennas & Propagation, IET*, 2015, *in review*.
 7. R.M. Hashmi, B.A. Zeb, K.P. Esselle, and S.G. Hay, "Effect of truncating the superstructures in broadband Fabry-Perot cavity antennas," *10th IEEE/MTT International Microwave and Optoelectronics Conference (IMOC)*, Rio de Janeiro, Brazil, 4-7 August, 2013.

1.5 Author's Contribution

In all the publications listed above, I have conducted the major investigations, designs, measurements, data processing, and drafting. Prof. Esselle, who is my principal supervisor, provided invaluable guidance, suggestions and advice at every stage of this research. He also reviewed, proof-read, and corrected all these manuscripts. Dr. Zeb provided initial support regarding the simulation environment as well as in the experiments on uniform composite superstrates. Dr. Hay, my adjunct supervisor from CSIRO, reviewed, corrected, and proof-read the last article in the list.

1.6 Dissertation Outline

Chapter 2 gives a brief overview of the origin and basics of electromagnetic band gap resonator antennas (ERAs) along with analytical models that have been used for their design and analysis in the past. A comprehensive review of the literature available on bandwidth enhancement of ERAs is included in this chapter, followed by a quantitative comparison of some key designs proposed in the last decade with the designs proposed in this dissertation.

In Chapter 3, the design and use of composite superstructures with wide defect-modes to design wideband ERAs is presented. It presents characterization and design of a three-layer dielectric superstructure that simultaneously provides wide defect-mode bandwidth, high reflection magnitude, and increasing reflection phase. Later on, this superstructure is used to design an ERA prototype with a significantly reduced footprint. In addition, associated auxiliary studies on a two-layer dielectric superstructure are presented in Chapter 4. It is shown through simultaneous use of DCM and SRM, that despite a wide defect-mode bandwidth of this two-layer superstructure, self-resonances in the superstructure can limit the performance of the resulting ERA, as compared to the design proposed in Chapter 3.

An alternative approach to wideband ERA design using single layer dielectric superstructures is presented in Chapter 5. These superstructures have a radially transverse permittivity gradient (TPG). This chapter thoroughly characterizes the TPG superstructures and also demonstrates wideband ERA design by using them. Design and experimental results of two low profile and extremely wideband prototypes are presented in Chapter 5. The relationship of aperture field with wideband directivity enhancement is also studied in this chapter.

Chapter 6 utilizes the interesting properties of defect-mode superstructures discussed in Chapter 3 to design an ERA that demonstrates excellent bandwidth with high aperture efficiency (average $\eta_{ap} > 90\%$ within the directivity bandwidth). Discussion and experimental results of the prototype ERA are provided, demonstrating a peak aperture efficiency as high as 135%. Chapter 7 develops the idea of high- η_{ap} ERAs proposed in Chapter 6 by arranging them in array configuration. Preliminary numerical results of a 2×2 array are presented and compared with classical multi-point excitation methods. It was also shown that despite a very high aperture efficiency, these arrays perform exceedingly well even with very small inter-element spacing.

The effect of finiteness of superstructures in enhancing the directivity bandwidth of ERAs is studied in Chapter 8. Detailed case studies are presented using single and double layered ERA superstructures. The effects of truncating individual layers in the superstructure to different sizes, and their effects on the antenna's bandwidth are quantified. A thorough discussion entailing experimental results and validation is presented. Chapter 9 contains the results of supplementary investigations that consolidate the idea presented in Chapter 8. It presents a quantitative study on reducing the footprint of a generic ERA superstructure and compares some of the key wideband designs documented in the literature, commenting on their performance with respect to superstructure sizes. Guidelines for designers on effectively truncating the ERA superstructures are presented.

Concluding remarks are drawn in Chapter 10 and a non-exhaustive list of future research directions is included.

Chapter 2

Background

This chapter provides background knowledge regarding periodic structures, electromagnetic band gap (EBG) materials, and their application to form directive antennas. In addition, it introduces the unfamiliar reader to analytical models that may be used to design and analyze such antennas. An introduction to periodic analysis is provided followed by its limitations, and available alternative approaches. In addition, the literature on bandwidth enhancement of EBG resonator antennas is briefly reviewed. Limitations of EBG resonator antennas addressed in this dissertation are discussed, commenting on their bandwidth limitations, superstrate finiteness, and associated design configurations. The chapter concludes with a quantitative summary of designs proposed in this dissertation.

2.1 Periodic Structures

Since the beginning of human history, several breakthroughs in science and technology are the result of mankind's thorough understanding of natural materials and the properties associated with them. With the transition from prehistoric to modern times, we have

learned how to achieve more than what nature provides in raw form. Nowadays, our lives benefit from a huge collection of artificially engineered materials that exhibit excellent mechanical properties. Interestingly, people's curiosity was not limited to just mechanics and scientists were intrigued to explore if it is possible to gain control over the flow of light and waves; even better, to guide, collimate, and mould them as desired. The search for answers to these questions gave birth to the fascinating domain of periodic structures and photonic crystals [16].

Periodic structures are one-, two-, or three-dimensional materials that are formed by periodic arrangement of a basic building block (so called 'photonic crystal' or 'unit-cell'), which eventually forms a lattice. Such an arrangement gives a particular periodic structure unique properties which can be shaped by controlling the arrangement of crystals in the lattice. Wave propagation in periodic media has been an intriguing area of study for more than a century. Initial contributions date back to the mid-18th century when Lord Rayleigh characterized the propagation of waves in such media using complex differential equations [17]. The earliest application of periodic structures was the design of electronic filters that was based on periodic networks at the beginning of the 20th century. However, the most interesting applications surfaced with advances in manufacturing technologies and artificial materials [18–20] that allowed us to achieve much more than ever before, for example, a perfect lens overcoming the diffraction limit [21], and volumetric cloaking of objects [22].

The broad term of periodic structures is defined as representing various sub-classes that include electromagnetic band gap (EBG) materials [23–25], metamaterials [26, 27], and frequency selective surfaces (FSS) [28]. Any isotropic material can be classified by its constitutive parameters, i.e. permittivity (ϵ) and permeability (μ). EBG materials are classified as materials that can exhibit an effective negative permittivity in a certain frequency band [29]. This negative permittivity causes the guided wave number k to

become imaginary, resulting in the generation of evanescent modes. Due to the excitation of these modes, such materials are able to prohibit the propagation of electromagnetic waves, totally or partially, in the direction of k , within a certain frequency band. This band is called the “electromagnetic band gap”. A thorough mathematical treatment of EBG structures is carried out in [16, 30], with detailed qualitative analyses found in [24]. Various applications of EBG materials that span over the commercial, satellite, and defense sectors include high-impedance surfaces [31, 32], microwave filters [23], and coupling reduction. EBG materials are often characterized structurally by the direction of band gaps they possess. Some examples of 1-D, 2-D and 3-D EBG structures are shown in Fig. 2.1. Amongst these applications, EBG materials are also used to design highly directive antennas known as EBG resonator antennas (ERAs). These antennas are mainly based on the angle dependent transmission and reflection properties of EBG structures. In the forthcoming sections, ERAs are described in detail, and their characteristics and limitations are explored.

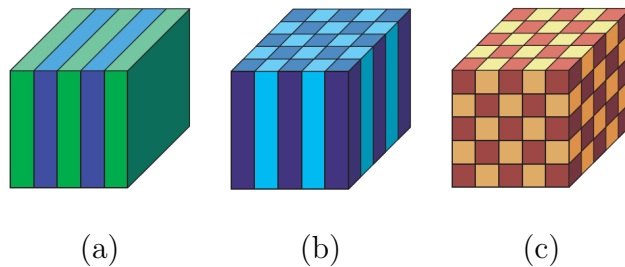


Figure 2.1: Block examples of (a) one-, (b) two- and (c) three-dimensional electro-magnetic band gap structures [16].

2.2 EBG Resonator Antennas

EBG resonator antennas (ERA) achieve increased broadside directivity by reinforcing reflected wave portions between a cavity that is formed by a partially reflecting superstrate

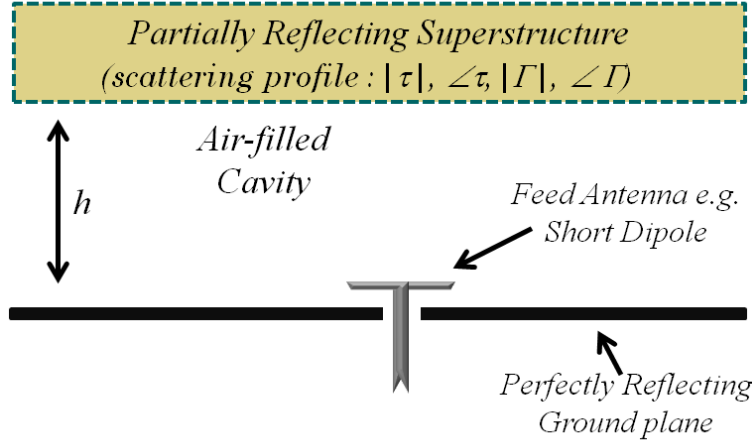


Figure 2.2: The general structure of an EBG resonator antenna showing a metallic ground plane, a symbolic superstructure, and an example feed source. In EBG analysis, the superstructure is often characterized by its scattering profile which will be discussed thoroughly in Section 2.5.

and a perfectly reflecting ground plane [4–6, 33]. An ERA generally consists of a linear, dual-linear or circularly polarized feed source, embedded within an air-filled resonant cavity [5, 8, 34]. This cavity is formed by a superstructure (a general term that encompasses 1-D, 2-D and 3-D superstrates) and a metallic ground plane, which are separated by a distance h . The general structure of an ERA is shown in Fig. 2.2 which depicts an ERA with a generic superstructure. The types of superstructure are discussed in detail in Section 2.3. With h adjusted to satisfy the cavity resonance condition, highly directive emissions towards the broadside can be achieved with only a single feed source [35].

The basic concept of ERAs dates back more than half a century when in 1956, Giswalt Von Trentini reported the directivity enhancement of simple radiating sources by the use of partially reflecting sheet arrays [36]. The concept remained dormant until the mid-1980s when Jackson and Alexopoulos reported that high broadside directivity can be achieved by placing one or more dielectric layers over a radiating source that is placed

next to a conducting sheet [36,37]. A few years later, transmission line theory was used to model the series of dielectric layers as a transverse equivalent network and asymptotic formulae were derived to predict the power pattern of these antennas [35]. In the early 1990s, a more fundamental yet complex approach involving leaky-wave analysis was used to study the radiation from these antennas which led to significant physical insight into their directivity enhancement [38,39]. Nearly a decade later, experiments on ERAs led demonstration of significantly enhanced antenna gain (around 20dB) by simple ERA configurations that were excited by a single source[4–6,33,40,41]. This tempted several researchers to devote their time and effort to understanding these novel antennas and on improving their performance using different analytical models [23,34,40,42–49]. Therefore, ERAs are also known as Fabry-Perot cavity antennas, resonant cavity antennas, and 2-D leaky-wave antennas.

Over the last decade, ERAs have been identified as excellent candidates for upper microwave and millimeter wave applications. At these frequencies, their high gain, planar nature, and simple configuration serve as a major advantage over bulky and complex alternatives. To maximize the focussing properties of the antenna, the superstructures are designed to provide high reflectivity, however, this is achieved to the detriment of antenna bandwidth. In ERAs, the bandwidth is often characterized by its directivity bandwidth. Directivity bandwidth, also referred to as pattern bandwidth or half power bandwidth, is defined as the range of frequencies where the directivity of the ERA remains within 3dB of the maximum value. The single feed in an ERA allows the directivity to be increased with minimal complexity, as compared to the feeding networks used in conventional antenna arrays and hence, is amongst the most desirable characteristics of ERAs. Various configurations have been designed in the past and produced high directivity at broadside, and addressed at least one of these aspects: bandwidth enhancement, footprint reduction, frequency reconfiguration, profile reduction, and multi-frequency operation. A historical

overview of such configurations is included in the following sections with a special focus on bandwidth enhancement of ERAs. In addition, fundamental principles of analytical models that analyze ERAs from different perspectives are also presented.

2.3 Superstructure Types

Designing ERA superstructures has been an interesting area of research [5, 8, 12, 13, 50, 51]. Superstructures are often classified in terms of dimensions, quantitatively, i.e. 1-D, 2-D or 3-D superstructures, whereas sometimes they are categorized structurally, qualitatively as “printed” and “unprinted” superstructures. They can take various forms such as 1-D stacks of alternating dielectric slabs [8, 10, 39], 2-D Frequency Selective Surfaces (FSS) [9, 11, 12] or 3-D periodic structures [52, 53]. Some examples of ERAs with each of these superstructures are shown in Fig. 2.3.

Over the years, their footprint reduction [15, 54–57], frequency reconfiguration [58–60], beam control [61–64] as well as bandwidth enhancement [9–12, 65–68] have been addressed for various applications such as mobile base stations, global satellite coverage, feed clusters for multi-beam antennas in space applications, and point-to-point microwave/millimeter wave links. To achieve high gain, sufficiently strong superstructure reflectivity (typically >0.6) is required [5]. However, high superstructure reflectivity results in a resonant cavity with a high quality factor (Q-factor). Therefore, the resulting single-feed antennas are highly directive but increasingly narrow-band.

2.3.1 Unprinted Superstructures

Unprinted superstructures encompass all superstructures that are made out of purely dielectric layers. These layers may be stacked [4, 8, 10], perforated [69], milled out for subtractive combining [70, 71], or pressed together to form additive composites [15, 51, 56, 72].

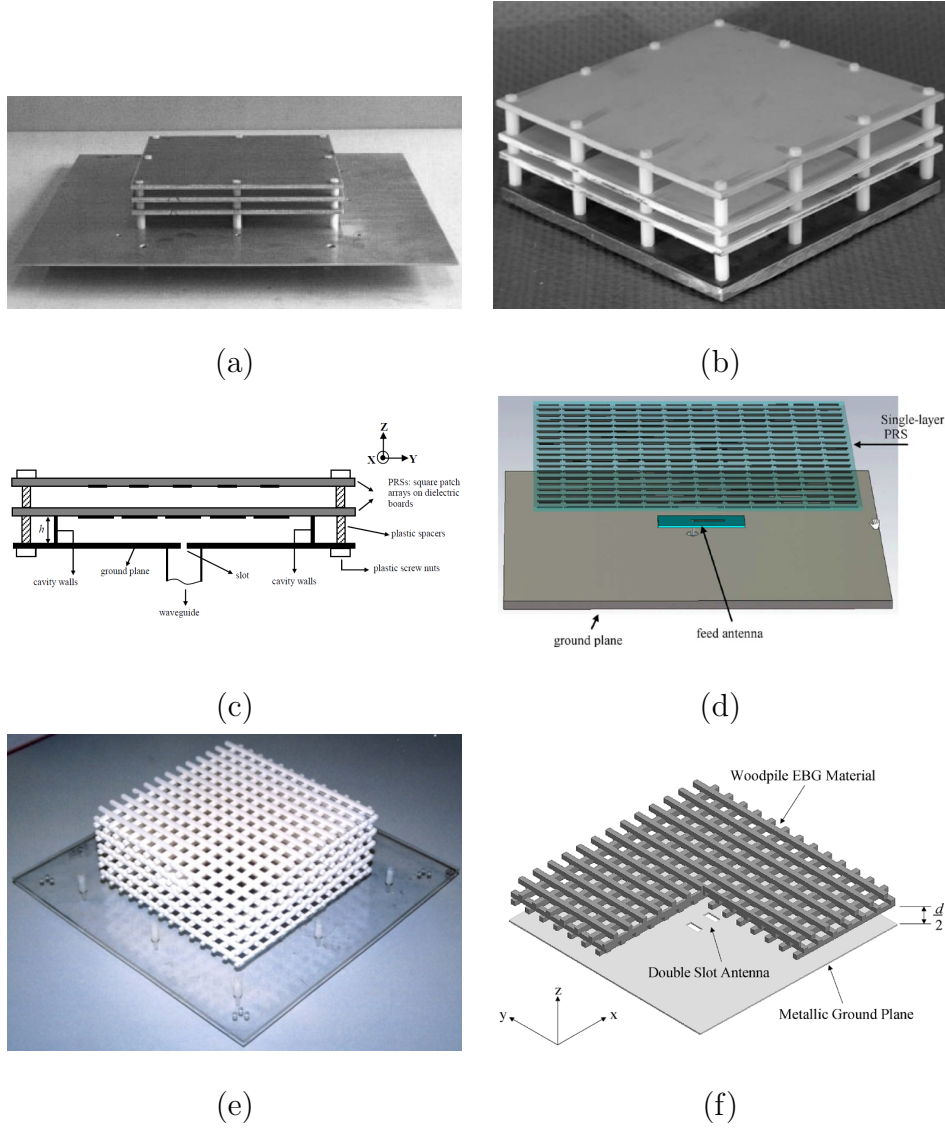


Figure 2.3: Examples of ERAs with 1-D, 2-D and 3-D superstructures: (a) classical 1-D EBG superstructure made by 3 dielectric layers [8], (b) “defected” 1-D EBG structure [10], (c) multi-layer 2-D FSS superstructure [9], (d) single layer thin 2-D FSS superstructure [12], (e) 3-D woodpile EBG superstructure [41], (f) truncated 3-D woodpile EBG structure [7].

The most commonly constructed superstructures in this category are 1-D EBG structures formed by stacking of dielectric layers that provide a band gap in the direction normal to the structure [4, 8, 10, 72]. Classically, there are a number of advantages associated with this approach:

- Manufacturing is simplified as commercially available dielectric layers can be used to construct a particular superstructure.
- Structural variations are minimized thereby reducing the sensitivity of the superstructure to etching/milling tolerances, and increasing the stability of the antennas. This is very attractive at upper microwave and millimeter wave frequencies.
- Polarization versatility is added to the design as the symmetry of the superstructures can be exploited by appropriately modifying the feed antennas to support dual-linear or circular polarization [60, 73].

However, these advantages are accompanied by the following price:

- The design is often constrained by the availability of dielectric materials and the thickness values available commercially.
- Antenna profile may be sacrificed when multiple layers are stacked together in conventional ways.
- Comparatively more volume due to weight and thickness of the dielectric materials (this may only apply to some cases).

2.3.2 Printed Superstructures

Printed (or so-called Metallo-dielectric) structures are single or multi-layer structures that may be manufactured by printing, etching or milling patterns on dielectric sheets, e.g.

printing metal strip gratings, split ring resonators, or other resonant elements (patches, slots etc.) [12, 14, 74–76]. In addition, these may also be realised by perforated grids made by drilling through a metallic sheet of finite thickness or by metallic wires/rods that are combined to form a mesh [34]. In most cases, application of these superstructures employs the reflection phase characteristics of a particular design instead of a band gap in the normal direction [75, 77, 78]. Key advantages associated with these are:

- Lower antenna profile since the structure gains its characteristics by the resonant nature of printed elements and not from periodic wave propagation. Thus, thin dielectric layers are often used for manufacturing and often, a single layer suffices for a classical ERA design [12, 75, 76].
- Possibility of using lower permittivity materials since the dielectric is often only the means of supporting the printed pattern and the actual permittivity of it are often of little significance [14, 75].

However, again these advantages are accompanied by the following tradeoffs:

- Printing/etching/milling may induce metallization-based tolerance in the design, thus making the antenna more sensitive. This is particularly important at upper microwave and millimeter wave frequencies [74, 75, 79, 80].
- Resonant bandwidth of the printed elements constrains the antenna's directivity bandwidth. This limitation can be addressed by stacking multiple printed layers with closely spaced resonant frequencies, however, the advantage of low antenna profile is lost [79, 80].
- The antennas are less versatile in terms of polarization extension especially in the case of circular polarization.

2.4 Analytical Models

As discussed in Section 2.2, over the last two decades different analytical methods have been used to study the behaviour of ERAs. Early models were mathematically more rigorous and proved to be invaluable in developing a better understanding of ERAs. Later, with advances in computing power combined with full-wave numerical solvers, hybrid approaches appeared multi-layer dielectric theory and periodic analyses [8,81,82]. Trentini first used ERAs excited by a single source to produce a high directivity at broadside [36] followed by critical studies carried out in [38,83,84]. All analytical models associated with ERAs are mainly based on the following four analytic models that are explained in more detail below.

2.4.1 Ray-Tracing Approximation

Building on the approach presented in [36], the ray-tracing approximation was thoroughly developed in [5]. Fig. 2.4 (a) shows the ray-tracing diagram of the antenna cavity that resembles a Fabry-Perot interferometer. Similar to the treatment of resonant optical cavities, this cavity in Fig. 2.4 (a) is formed between a highly reflective PRS and a perfectly reflecting ground plane. It should be noted that the reflection characteristics of the PRS are frequency dependent where as for the ground plane, they are constant, i.e. $|\Gamma_{ground}| = 1, \phi_{ground} = -\pi$. A waveguide used to feed the resonant cavity can be seen in Fig. 2.4 (b). This waveguide acts as the primary excitation and emanates waves inside the cavity. These waves bounce between the ground plane and the PRS repeatedly as they travel radially outwards, progressing through the parallel walled cavity. As a result of these multiple reflections, a phase shift is introduced corresponding to three factors: the length of the path the waves travel through, the total reflection on the ground plane, and the phase of the reflection coefficient of the PRS. By superposition of the rays that

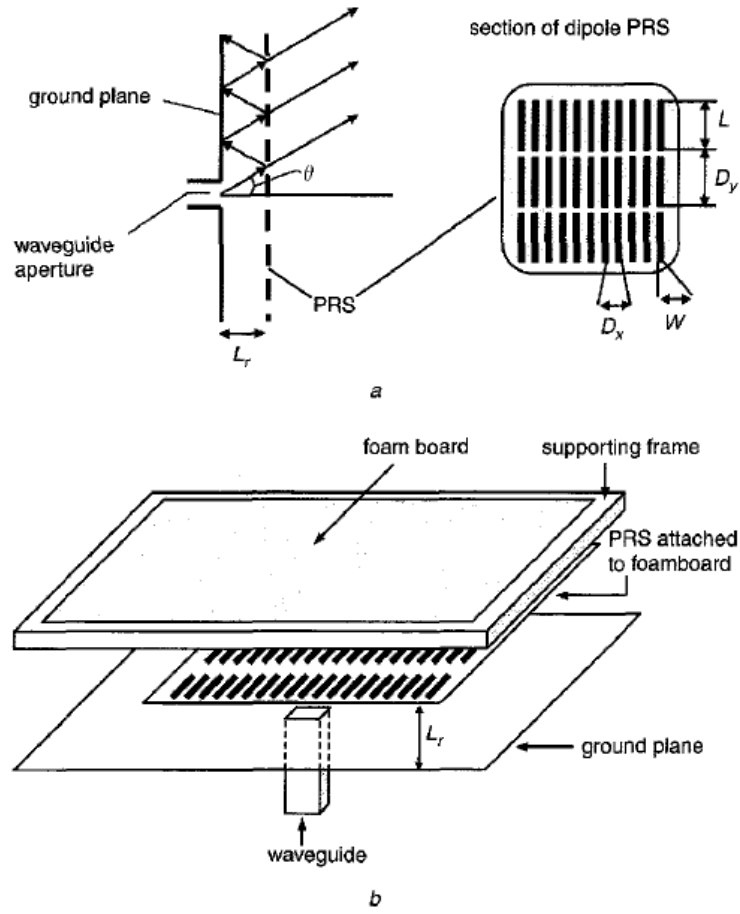


Figure 2.4: Conceptual model of the antenna proposed in [5] (a) The ray-tracing diagram of the Fabry-Perot type cavity formed between the PRS and the ground plane, (b) structural view of the proposed antenna.

are partially transmitted through the PRS, it is possible to calculate the far-field power pattern by summing up these transmitted rays [5]. This frequency response of the power pattern is largely dependent on the complex broadside reflection coefficient of the PRS, as well as the resonant length L_r , the distance between the ground plane and the PRS. To obtain maximum power towards broadside, the resonant length L_r should be adjusted such that

$$\phi_{PRS}(f, \theta = 0) + \phi_{ground}(f) - \frac{4\pi L_r}{\lambda} = 2N\pi \quad (2.1)$$

However, it should be noted that the above formula assumes the PRS and ground plane to be infinite in transverse directions, and finiteness effects are not accounted for. This value of L_r when substituted in the generalized power pattern of the PRS can be solved for gain enhancement. The gain enhancement that can be achieved by the PRS compared to the gain of the feed antenna, is given by

$$G_{PRS} = \frac{1 + |\Gamma_{PRS}|}{1 - |\Gamma_{PRS}|} \quad (2.2)$$

A simple formula for estimate of the 3dB bandwidth was also provided in [5] which states that

$$Bandwidth = \frac{\lambda(1 - |\Gamma_{PRS}|)}{2\pi L_r \sqrt{|\Gamma_{PRS}|}} \quad (2.3)$$

Later, Boutayeb et al. further developed this model to provide a comparatively more complete prediction of 3dB bandwidth that was based on the quality factor (Q-factor) of the cavity as

$$\Delta\theta_{3dB,min} \approx \sqrt{\frac{2}{Q}} \quad (2.4)$$

where Q-factor describes the selectivity of the cavity and can be expressed as a function of both $|\Gamma_{PRS}|$ and ϕ_{PRS} [85]. Thus, the ray-tracing approximation states that antenna gain increases significantly with an increase in $|\Gamma_{PRS}|$ but at the detriment of 3dB bandwidth. Rearranging eq. 2.2, it is noticeable that increased gain over a certain frequency range can be obtained if ϕ_{PRS} satisfies the following condition

$$\phi_{PRS}(f, \theta = 0) = \frac{4\pi L_r}{\lambda} - (2N - 1)\pi \quad (2.5)$$

This condition can be used for bandwidth enhancement of ERAs and is used to develop a unit-cell design model in Section 2.5.

2.4.2 EBG Defect Model

The concept of EBG defect model was initially proposed in [4, 40]. As described earlier, EBG structures can be used as antenna PRS. When the periodicity in these structures is disturbed by introducing defects in the EBG lattice, their band gap displays localized frequency windows within the forbidden frequency band due to the induced anisotropy. As opposed to outside the band gap where several modes may propagate through these windows, only a single mode is allowed to propagate. This property is very useful for designing ERAs. At the defect frequency, the distribution of electromagnetic fields within the superstrate changes along specific directions and the aperture of the antenna, created on the superstrate by the fields excited within the cavity, becomes large [44]. This allows for enhanced directivity provided by the ERA. It is envisaged that if the defect can be made to encompass a wide range of frequencies, the frequency response of the resulting ERA can be increased. This property is used to develop a unit-cell design model in Section 2.5.

Although the most general ERA can be constructed with only one dielectric slab dielectric, metamaterial slab, or if a FSS is employed as a PRS [87], multilayered EBG structures can be used to demonstrate the band gap and defect band gap of the EBG materials. Fig. 2.5 shows two multilayered EBG structures where the first one is a stack of uniform dielectric slabs (Fig. 2.5 (a)) and the second one contains a defect created by removal of the middle slab (Fig. 2.5 (b)). The dielectric slabs have thickness d_1 , permittivity ϵ_1 and are spaced h_1 apart. The defect introduced in Fig. 2.5 (b) creates a defect-resonator with a resonant height equal to $2h_1$ where the defect-mode will correspond to $f = c/(2h_1)$. By exploiting the symmetry of this defect in the EBG structure (Fig. 2.5

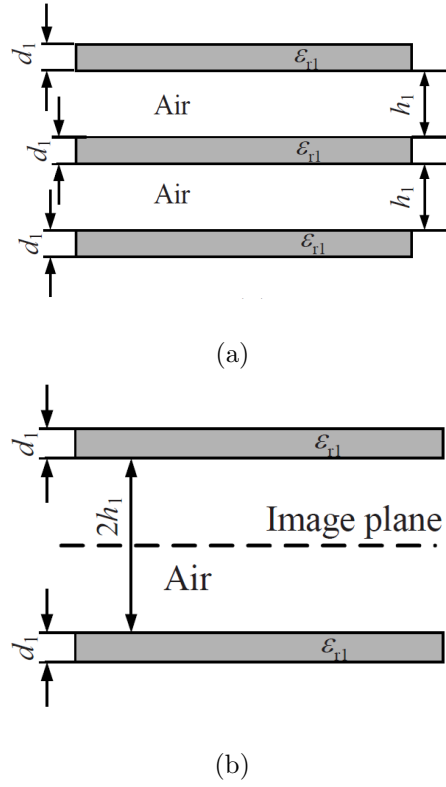


Figure 2.5: Simple EBG structure made out of stack of dielectric layers (a) 3 layer EBG structure, each layer is quarter guided-wavelength thick ($d_1 = \lambda_0/(4\sqrt{\epsilon_{r1}})$) and spaced quarter free-space wavelength apart ($h_1 = \lambda_0/4$), (b) The same EBG structure with defect, the upper and lower half of the structure are dual in nature and have an image plane in the centre [86].

(b)), a metallic plate ($\Gamma = 1, \phi = -\pi, E_{\text{tangent}} = 0$) can be positioned at the image plane that forces the radiation into a hemisphere above the ground plane, and creates a resonant cavity with height $\approx h_1$. Fig. 2.6 shows a band gap obtained using this approach where an EBG structure with six dielectric slabs was employed in [8].

The band gap approach was further developed in [8] using the transmission matrix for the multilayered dielectric. This yielded formulae for reflection and transmission from the EBG structures under both, normal ($\theta_0 = 0^\circ$) and oblique ($\theta_0 = \theta_{\text{inc}}$) incidence. The transmission through a multilayered EBG structure is given by

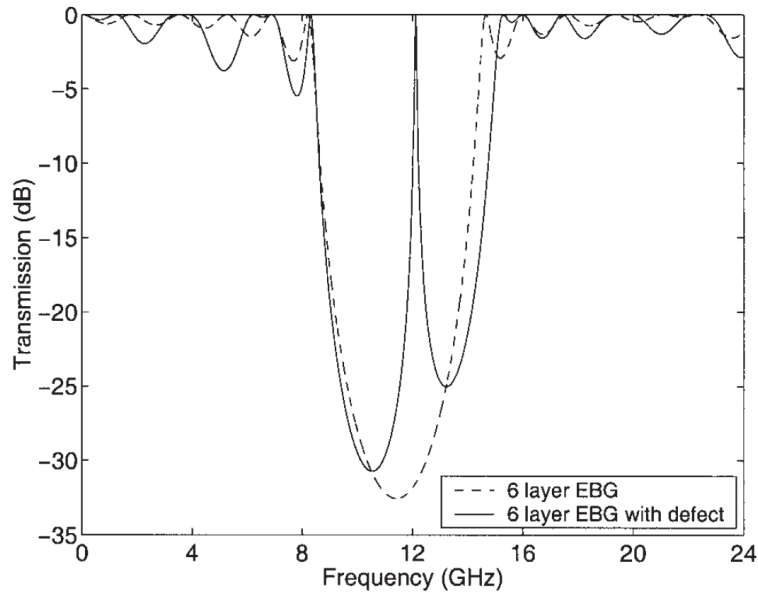


Figure 2.6: Band gap obtained with a 6 layer 1-D EBG structure in [8]. The defect-mode obtained by disturbing the periodicity is also shown here.

$$T = \frac{4\eta_0 \Re\{\eta_m\}}{(\eta_0 B + C)(\eta_0 B + C)^*} \quad (2.6)$$

where η_0 designates the free space refractive index and η_m corresponds to the exit medium.

The reflection, on the other hand, can be obtained as

$$R = \frac{\eta_0 B - C}{\eta_0 B + C} \cdot \left(\frac{\eta_0 B - C}{\eta_0 B + C} \right)^* \quad (2.7)$$

where B and C are given by

$$\begin{bmatrix} B \\ C \end{bmatrix} = [M_1][M_2] \dots [M_m] \begin{bmatrix} 1 \\ \eta_m \end{bmatrix} \quad (2.8)$$

M_1 to M_m are transfer matrices corresponding to each of the dielectric layers.

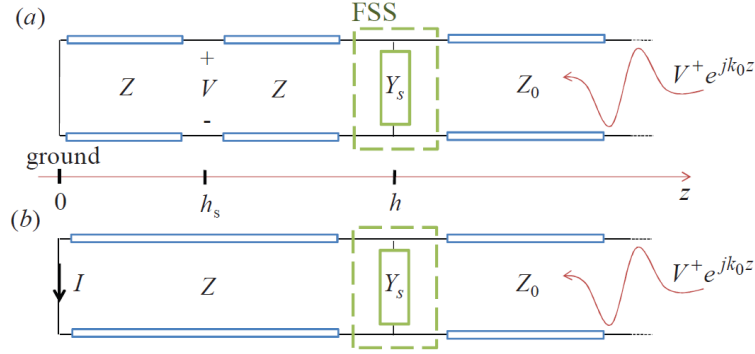


Figure 2.7: The transverse equivalent network model of an ERA derived from [90] (a) when fed using an electric dipole in the middle of the cavity at distance h_s , and (b) fed by a magnetic dipole (slot) on the ground plane of the antenna.

2.4.3 Transmission Line Model

The transmission line model (TLM) is based on circuit theory and has been applied rigourously in the past to analyze the ERAs [35, 37, 39, 73, 88, 89]. The TLM serves as a cascade model of transmission lines where each layer in the ERA, i.e. dielectric slabs, air spaces, and the ground plane are modeled as sections with different characteristic impedances. Fig. 2.7 shows two TLMs of two ERAs that have a FSS (2-D EBG) superstrate, excited using (a) magnetic dipole, and (b) electric dipole.

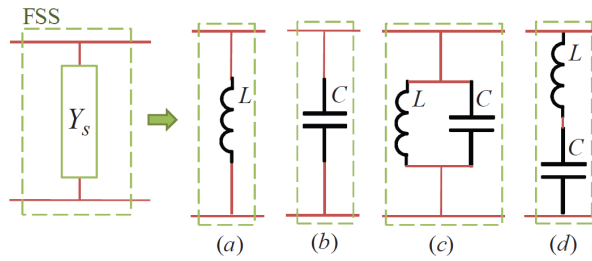


Figure 2.8: Circuit elements used to model the FSS that are implemented using (a) slots printed on a substrate, (b) patches printed on a substrate, (c) patches and slots printed above and below the substrate, and (d) reciprocal case of (c).

In Fig. 2.7, Z_0 models the free space above the ERA, Y_s is the admittance of the

FSS, and Z model the cavity of the ERA with a ground plane at the end. Jackson and Alexopoulos established the resonant conditions using reciprocity, when a plane wave is incident on the ERA, denoted by $V^+e^{jk_0z}$ [37]. Simple asymptotic formulae to calculate resonance, gain, beamwidth, and bandwidth for ERAs with a multilayered dielectric superstrate were established [37]. Fig. 2.8 depicts the various circuit elements that may be used to model the admittance of the FSS. These models are implemented in reality using metallo-dielectric superstrates and have been used in various practical ERA designs [90,91].

2.4.4 Leaky-wave Model

The leaky-wave (LW) radiation from a microstrip antenna in a superstrate-superstrate configuration was examined initially in [38,39]. Fig. 2.9 (a) shows an ERA where a multilayered dielectric superstructure acting as a PRS. From the LW point of view, the PRS structure acts like a leaky parallel plate waveguide which is excited by a source. Since the PRS is an isotropic, homogeneous medium, the TM_z and TE_z modes are excited by the source. However, the power carried by each of the modes leaks through the top of the parallel plate structure. Each mode becomes a radiating leaky mode with a complex wave number $k_p = \beta - j\alpha$ where β is given by

$$\beta \cong k_0 \sin \theta_p \quad (2.9)$$

where k_0 is the free space wave number and θ_p is the angle of incidence measured from the normal direction (as shown in Fig. 2.9 (a)). The attenuation (leakage) constant α is determined by the geometrical properties of the PRS as discussed in [92]. The far-field radiation pattern of the antenna may be calculated either by taking Fourier transform of the aperture field at $z = 0$, or by invoking reciprocity. Computationally, the latter is the simplest approach [39,84,89,92,93]. The LW model also allows for simple design

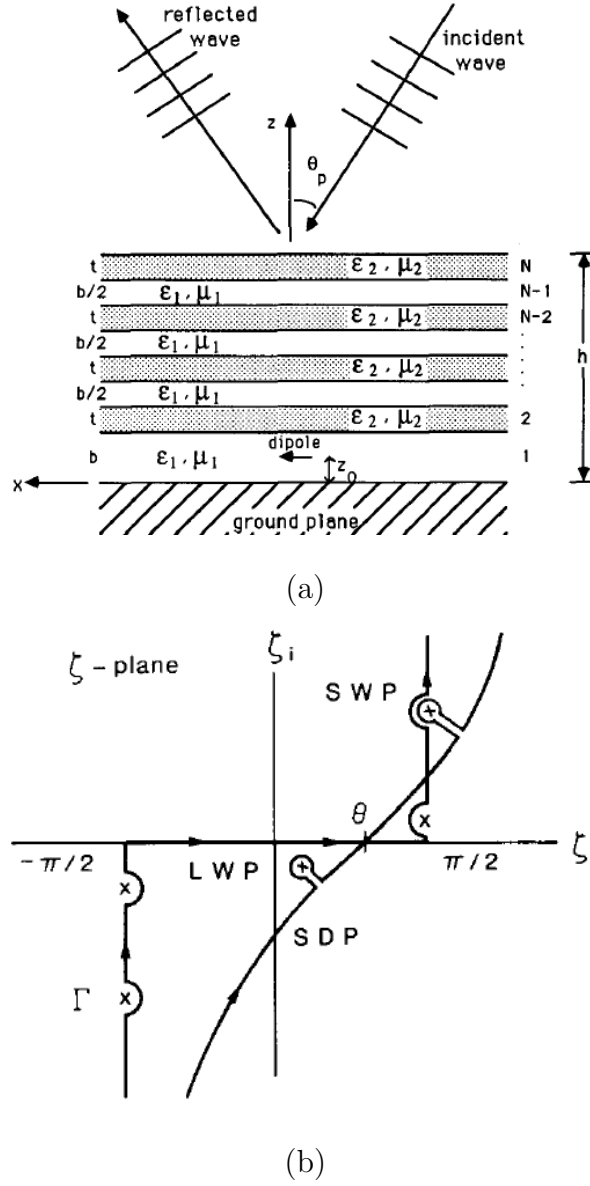


Figure 2.9: The leaky wave antenna model: (a) Multilayered LWA geometry with dipole excitation. The incident angle measured from the normal axis is $\theta_p = 0$ for broadside radiation (b) Steepest descent path corresponding to time dependence $e^{j\omega t}$. Saddle-point is present at $\xi = 0$ on real axis, and an example is given of leaky-wave pole and surface-wave pole captured by deformation from original path Γ to steepest descent path [39].

formulas that can be used to initialize as well as optimize the ERA designs. It was shown in [39] that highly directive beams can be produced if the thickness of the layers in the superstrate/PRS are chosen appropriately as

$$\frac{n_1 b}{\lambda_0} \sqrt{1 - (\sin^2 \theta_p)/n_1^2} = \frac{m}{2} \quad (2.10)$$

$$\frac{n_2 t}{\lambda_0} \sqrt{1 - (\sin^2 \theta_p)/n_2^2} = \frac{2p - 1}{4} \quad (2.11)$$

where n_1 and n_2 are the respective refractive indices corresponding to the media in Fig. 2.9 (a), t is the thickness of the dielectric slabs, b is the spacing as shown in Fig. 2.9 (a), and $(m, p) = 1, 2, \dots, N$. Theoretically, this approach has roots in the spectral Green's function and steepest descent contour integration. As shown in Fig. 2.9 (b), the steepest-descent path passes through the saddle point where the integral contour covers not only the surface wave poles, but also the leaky-wave poles [38].

This can generate a resonance condition, whereby the leaky-wave poles make a dominant contribution to the far field and determine the radiation pattern. It can be validated that the resonance condition obtained by the leaky-wave model is the same as that obtained by the transmission line model [92]. This also provides an alternative definition of α and β as

$$\beta = k_0 \sin \zeta_r \cosh \zeta_i \quad (2.12)$$

$$\alpha = -k_0 \cos \zeta_r \sinh \zeta_i \quad (2.13)$$

One of the key features of the LW theory is its ability to predict the required structure size in the transverse directions to realize the narrow beam patterns. Conversely, all the three preceding models assume infinite transverse extent and do not account for finiteness. The

general guideline here is that the transverse size should be large enough to ensure that the leaky waves are sufficiently attenuated at the perimeter of the antenna [89, 94, 95]. Mathematically, if the structure radius is r , then $\alpha.r \gg 1$ is expected.

2.5 Periodic Analysis: Unit-Cell Models

In this section, the extension of the ray-tracing approximation and the EBG defect model are shown as unit-cell models that can be used for efficient design and analysis of the ERAs. Both these models assume that the superstrate or the EBG structure is illuminated by a plane wave that is often normally incident on the superstrate. In addition, these models assume the transverse extent of the structure to be infinite. Therefore, to compute the scattering response of EBG structures, unit-cells are used instead of the entire structure. Finite difference time domain (FDTD) or finite-element method (FEM) based full-wave solvers can be used to compute and optimize the scattering response of EBG structures. In CST microwave studio, periodic boundary conditions can be used in the frequency domain solver where scattering response for oblique incidence as well as normal incidence can be computed. While in the transient solver, perfectly matched layer (PML) boundaries can be employed to compute the response for normal incidence; oblique incidence cannot be computed using transient solver. It has been demonstrated in the past that the predictions of these models reasonably agree with the predictions of the transverse equivalent network model.

2.5.1 Superstrate Reflection Model (SRM)

The superstrate reflection model (or SRM) is a unit-cell model that computes the reflection magnitude and phase of a particular superstructure. Theoretically, this model roots back to the ray-tracing approximation and is built on the same assumptions. For a simple PRS

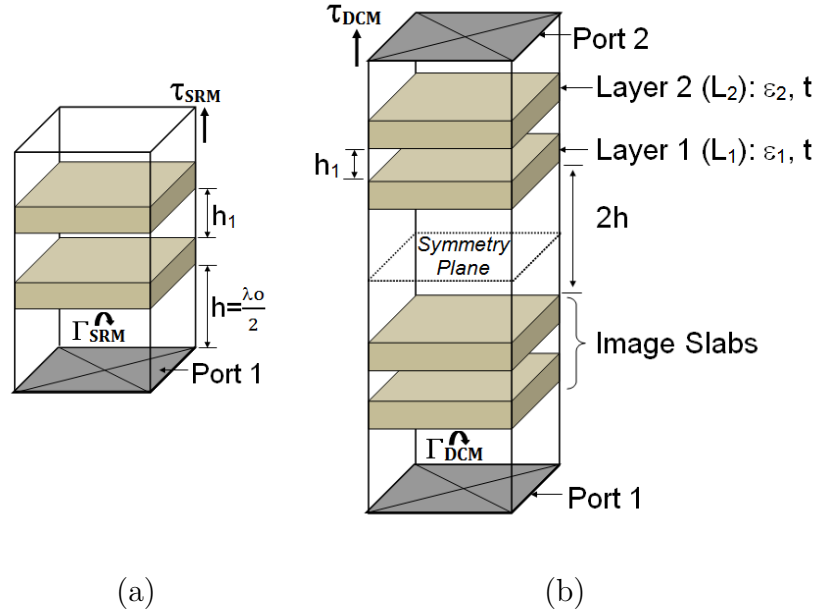


Figure 2.10: Unit-cell models used for computing 1D scattering from the periodic structures (a) superstructure reflection model, and (b) defect cavity model [81].

composed of two unprinted dielectric layers, the SRM is shown in Fig. 2.10 (a). Each dielectric layer has a thickness t , permittivity ϵ_r , and separation h_1 . A waveguide port is applied at one end of the superstructure such that the normal vector of the port coincides with the normal vector of the superstructure. The port is de-embedded to a distance h , which is equal to the height of the cavity. This allows for the reflection phase to be calculated at the surface of the superstructure¹. In addition, the wave port simulates the plane wave incidence on the superstructure, as required for the ray-tracing approximation. Perfect electric and perfect magnetic boundaries are applied to the corresponding lateral sidewalls to extend the superstructure infinitely in transverse directions.

The reflection phase of a typical superstrate decreases monotonically with an increase

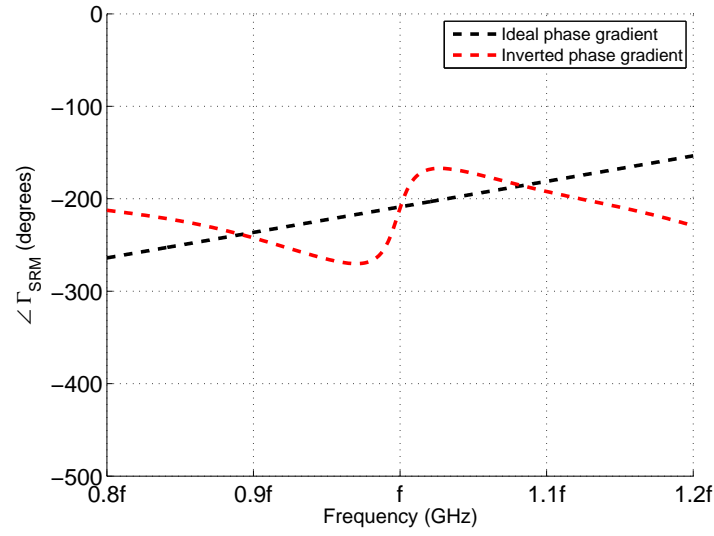
¹The reflection phase of the superstructure defined at the bottom surface of the lower layer in Fig. 2.10 (a) is equal to the phase calculated at Port 1 minus twice the path delay between Port 1 and the bottom surface of L_1 . Therefore, the value of Γ at port 1 is obtained through a full-wave solver and then the phase correction is applied using port de-embedding to obtain $\angle\Gamma_{SRM}$.

in frequency. In order to design a wideband antenna, the reflection phase of the superstructure should be engineered to follow the ideal curve in the operating bandwidth [5]. SRM has proven to be invaluable for such optimizations while being fast and computationally inexpensive. The reflection phase of the superstructure ($\angle\Gamma_{SRM}$) of an ideal EBG structure (that exhibits the ideal phase for directivity enhancement according to the cavity resonance condition) is plotted in Fig. 2.11 (a). The inverted phase gradient is also shown in Fig. 2.11 (a), which is the phase of the superstructure shown in Fig. 2.10 (a). This phase is achieved by the variation of permittivity (ϵ_2) of L_2 , with respect to that of L_1 (ϵ_1). The closer the reflection phase can be made to the ideal phase, the more consistent directivity enhancement is expected by the ERA.

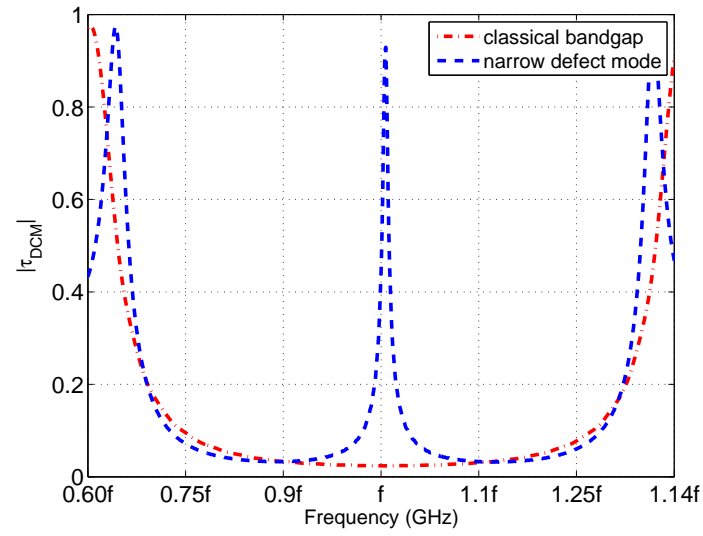
2.5.2 Defect Cavity Model (DCM)

The defect cavity model (or DCM) is used to compute transmission through a particular EBG structure. DCM is theoretically related to the EBG defect model discussed earlier. Defects can be induced in periodic structures to create localized transmission windows in the band gap. The frequency response of a stack of dielectric layers, when a plane wave is normally incident on it, is shown in Fig. 2.11 (b). It shows a classical band gap that extends from $0.65f$ to $1.35f$ as well as the defected band gap with the narrow defect mode occurring at $f_0 = f$. It is computed through the DCM shown in Fig. 2.10 (b). It is formed by mirroring the superstructure along the symmetry plane to include its image. Waveguide ports are assigned at the top and bottom of the superstructure, shown in Fig. 2.10 (b) as Port 1 and 2. In this case, de-embedding is not necessary as the primary figure of interest is the transmission magnitude ($|\tau_{DCM}|$). Similar to the SRM, perfect electric and perfect magnetic boundaries are applied to corresponding lateral sidewalls.

For a structure with two dielectric layers (L_1, L_2), the thickness of slabs (t_1, t_2), their permittivity (ϵ_1, ϵ_2), and their separation (h_1) are the parameters, which can be opti-



(a)



(b)

Figure 2.11: (a) Reflection phase computed using SRM showing an inverted phase gradient, calculated ideal phase for directivity enhancement over wideband is also shown, and (b) Band gap calculated using the DCM as well as the defected band gap are shown [96].

mized to influence the width of the defect in the band gap. Wideband defect modes result in wideband ERAs and therefore, DCM provides an efficient and computationally inexpensive means of carrying out such optimizations using full-wave solvers.

2.5.3 Limitations of Periodic Analysis

Despite the fact that periodic analysis has proven to be a powerful and robust method in optimizing ERAs, it has its limitations. Like any other model, periodic analysis is based on a certain set of assumptions. Although these assumptions have been discussed earlier in the chapter in different sections, they are presented below for comprehensive understanding, alongside the associated limitations.

1. Periodic analysis assumes that the superstructure is periodic in transverse directions and therefore is taken to be infinite. For this reason, SRM or DCM cannot be effectively used to study aperiodic superstructures (e.g. having transverse permittivity contrast, transverse gradients) such as those proposed in [11, 70, 71, 79, 80, 87].
2. Due to the assumption of infinite transverse extent, the predictions of SRM and DCM for designing wideband ERAs hold well when the footprint of the superstructure is reasonably large as observed in [57, 72].
3. Although periodic analysis provides a good starting point for the design of ERAs with severely truncated superstructures, it cannot account for the field that is diffracted from the edges and thus, cannot predict the bandwidth or directivity of these ERAs [15, 82, 96, 97].
4. Periodic analysis assumes that the transverse footprint of the cavity in ERAs is large enough such that it is safe to assume that the field in the cavity is nearly uniform. For this reason, plane wave incidence is used to study the 1-D scattering response

from the structure under study. However, in most of the practical ERAs, the field in the cavity is non-uniform and equi-phase incidence does not hold [57, 82, 98].

For these limitations, the design of modern ERAs that are severely truncated, compact, and often employ superstructures with transverse gradients, cannot solely rely on periodic analysis as has been the practice in the past. To effectively utilize the field diffraction from the edges of the superstructures and to understand their contribution to bandwidth enhancement/directivity enhancement, more complete methods should be used. These methods include full-wave design of the composite antenna (e.g. using CST Microwave Studio, Ansys HFSS, or FEKO, etc.), custom optimization engines (e.g. MATLAB or Maple, that use periodic analysis in conjunction with full-wave solvers), and field transformation approaches. Unlike the approaches used in the past where most of the design choices were made in the periodic analysis phase, it is essential, considering the above limitations, that the composite antenna design be thoroughly conducted and antenna parameters are optimized in this phase.

2.6 Directivity Bandwidth and Footprint

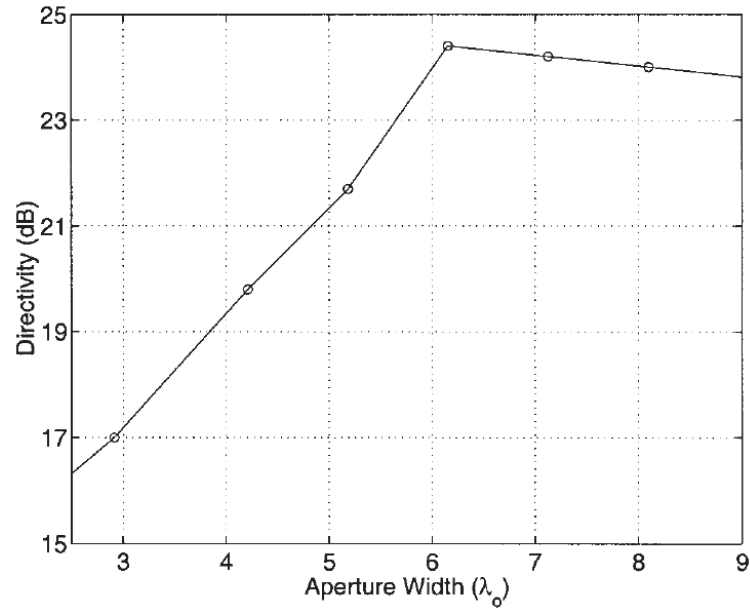
All analytical models associated with ERAs assume the ideal scenario that the superstructure has infinite transverse extent. However, all practical antennas must be finite and therefore, the superstructure layers need to be truncated to a finite size in real antennas. For this reason, the LW model was used to predict a finite size of the resulting antenna. Theoretically, the longer the leaky waves travel within the cavity, the larger the aperture they create on the superstructure, and thus, the higher the directivity obtained from the antenna. However, as the waves travel outward, their strength is reduced exponentially as a factor of squared distance from the centre of the cavity. Hence, it was suggested that the transverse size should be large enough to ensure that the leaky waves excited within

the cavity are sufficiently attenuated at the perimeter of the antenna [89, 94, 95].

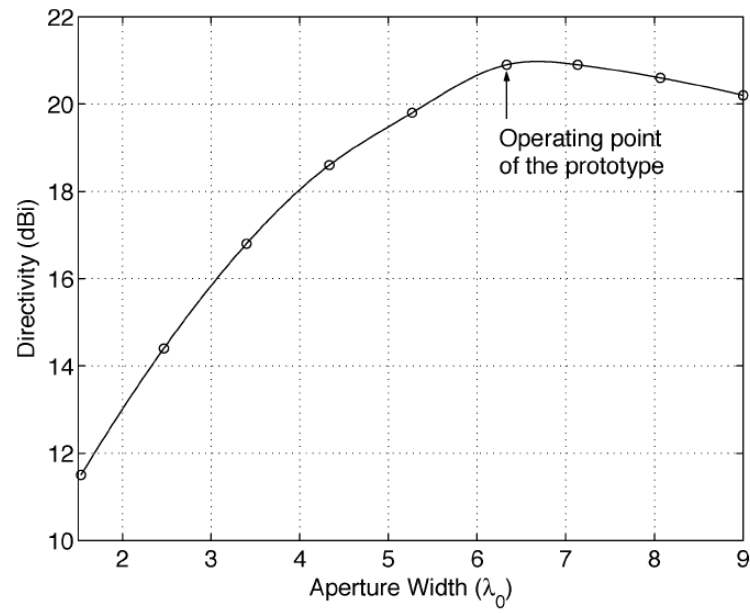
It is well-known that the maximum obtainable directivity is a characteristic of the superstructure [5, 37, 89]. However, within this limit, the peak directivity of a particular ERA largely depends on its footprint. Computed peak directivity of two ERAs for increasing footprint is shown in Fig. 2.12 as studied in [7, 8]. These results were computed through FDTD simulations by varying the length of the superstructure equally in the transverse directions (length is denoted by aperture width (λ_0)). It is evident in Fig. 2.12 (a) that the ERA directivity shows a linear increase with ERA's length between $2.5\lambda_0$. Above this length, the directivity saturates and begins to converge to a value just slightly below the maximum. Below $2.5\lambda_0$, it was found that the directivity drops rapidly as the size of the superstructure approached the size of the feed and sidelobe levels began to rise significantly. A similar trend is observed in Fig. 2.12 (b) which shows similar results for a 3-D EBG superstructure. Hence to achieve maximum directivity, most of the ERA prototypes were designed with large footprints often ranging between $20 - 36\lambda_0^2$. Also, it is considered that conventionally, the directivity and footprint of an ERA follow an inverse relationship, whereas the bandwidth often increases with a decrease in footprint. However, the challenge addressed in this dissertation is to achieve high directivity and wide bandwidths, while minimizing the footprint of the ERAs. It will be shown that it is possible to design superstructures that can provide maximum obtainable directivity with small footprints [15, 51, 57, 96, 97]. Such designs significantly minimize the computational payload, thereby making the composite design of ERAs inexpensive.

2.7 Composite Antenna Design

Composite design of ERAs can be conducted through in-house or commercial full-wave solvers. In this case, the complete antenna is simulated instead of only unit-cell models and



(a)



(b)

Figure 2.12: Computed peak directivity of two ERAs for increasing footprint area. The superstructures considered for these computations are square and aperture width denoted by λ_0 is the length of one side of the superstructure (a) 1-D EBG structure [8] and (b) 3-D woodpile EBG structure [7]

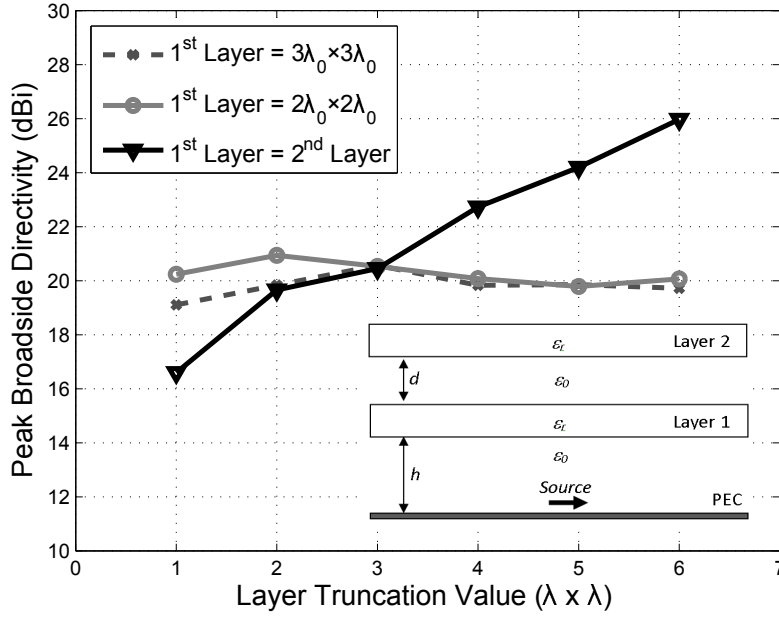


Figure 2.13: Peak broadside directivity computed as a function of size of the superstrate layers by varying L_2 from $1\lambda \times 1\lambda$ to $6\lambda \times 6\lambda$. The directivity of classical ERA with equally truncated layers is also plotted for reference.

therefore, in addition to the radiation from the aperture formed on a superstructure, the fields diffracted from the edge are also accounted for. This is an extremely simple method that directly results in improved bandwidth and directivity. As an example, consider a traditional EBG superstrate consisting of two finite-sized dielectric layers. Traditionally, these layers are truncated to equal lateral dimensions. However, it was found that the lateral truncation of each layer in the superstructure affects the peak directivity and 3dB bandwidth of the resulting ERA. When the truncation of individual layers was studied for various sizes ranging from very small ($\approx 1\lambda_0$) to reasonably large values ($\approx 6\lambda_0$), several interesting combinations of truncation values were recorded (as discussed in Chapter 8) which offered far better bandwidth and/or peak directivity than the equally truncated superstructure. This interesting result cannot be perceived through periodic analysis alone.

Empirical models can be constructed through case studies based on composite design of ERAs to quantify the behaviour of truncating individual layers in the superstrates to various practically feasible values. Fig. 2.13 shows the response of peak broadside directivity when the second layer in a two-layer superstructure varies from $1\lambda_0 \times 1\lambda_0$ to $6\lambda_0 \times 6\lambda_0$ with the first layer fixed at $2\lambda_0 \times 2\lambda_0$ and $3\lambda_0 \times 3\lambda_0$, respectively. It is observed in Fig. 2.13 that peak directivity could be made to increase with the decrease in superstructure size, contrary to the conventional relationship. Furthermore, it will be shown in Chapter 8 through a similar case study on individual layer truncation that it is possible to achieve improved bandwidths for larger footprints, again contrary to the conventional relationship. Moreover, it was also observed that since the first layer and ground plane form the primary cavity, the variation in the first layer directly affects the input matching of the feed antenna in the cavity. This knowledge can be utilized as a degree of freedom to fine-tune the input reflection coefficient of the ERA, which is a crucial step to achieve high radiation efficiency.

Building on this knowledge, a simple ERA demonstrating nearly double bandwidth potential is shown in Fig. 2.14. It uses a conventional two-layer EBG structure having uniform permittivity ($\epsilon_1 = \epsilon_2 = 9.2$) and thickness ($t_1 = t_2 = \lambda_g/4$). Initially, both L_1 and L_2 were set to equal lateral size of $4\lambda_0 \times 4\lambda_0$. On varying the lateral size of L_1 to $3\lambda_0 \times 3\lambda_0$, the directivity bandwidth of this ERA was almost doubled. This behavior is attributed to the radially leaking fields within the primary cavity which are diffracted by the edges of L_1 to contribute coherently to the fields being radiated from the top of L_2 .

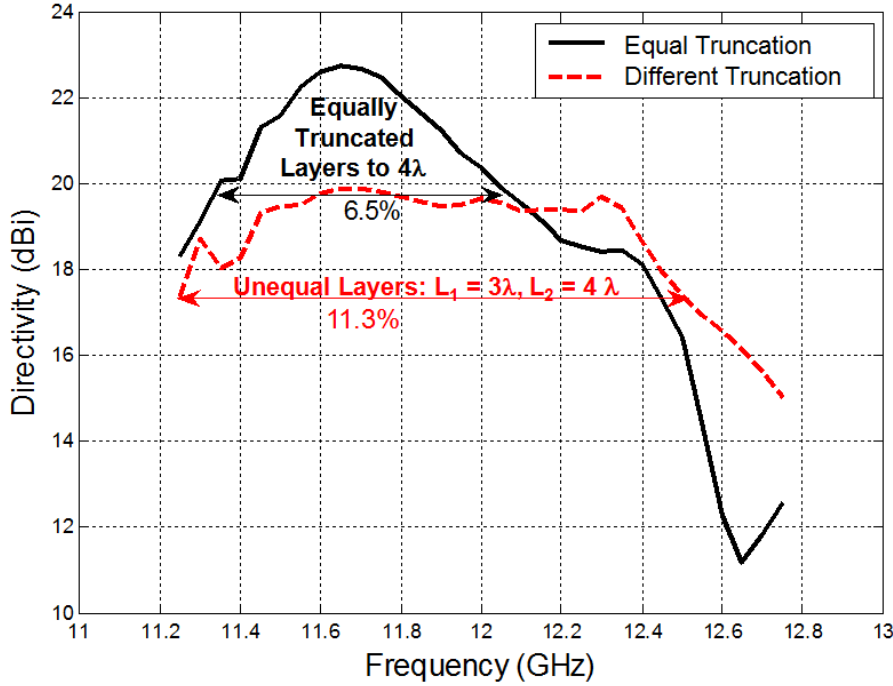


Figure 2.14: Comparison of 3dB bandwidth of the classical 2-layer ERA with unequally truncated layer ERA. For the latter, L_1 and L_2 truncated to $3\lambda_0 \times 3\lambda_0$ and $4\lambda_0 \times 4\lambda_0$, respectively [98].

2.8 Reviewing the Literature on ERA Bandwidth Enhancement

In this section, we comprehensively and critically review the literature on bandwidth enhancement of ERAs. Unlike most antennas that are limited by their impedance bandwidth, ERAs are often limited by their half power directivity bandwidth (3dB directivity bandwidth) and of course, their half power gain bandwidth (3dB gain bandwidth). Ever since the practical design and experimentation on ERAs began in the late 1990s, their narrow bandwidth was a major limitation for most practical applications. Early ERAs were notoriously narrowband with bandwidths reaching only up to 1-3% [4, 5, 7, 8, 41]. The theoretical models stated earlier suggest that the resonance of the Fabry-Perot type

cavity in an ERA results in a standing wave that is created within the cavity. This standing wave is a spectral function of constructive superimposition of multiple-reflected rays. Thus, a first step towards bandwidth enhancement of ERAs was to achieve wideband cavity resonance. To achieve such resonance, the reflection phase of PRS must suffice for the variation in reflected wavelengths over a wider range of frequencies. Following this approach, various researchers focussed their attention on designs based on printed resonant structures to achieve reflection phase approaching the increasing gradient requirement set out in [5].

2.8.1 Multi-layer Printed PRS-based ERAs

Initially, a method for obtaining broadband performance while maintaining high gain performance was presented in [9]. The design was based on a two-layer metallo-dielectric PRS. The size of the patch array printed on each layer of the PRS was different. It was adjusted such that the reflection phase response of the PRS satisfied the resonance condition of the cavity at a wide range of frequencies. Highly directive ERAs with improved bandwidth can be designed using this technique while resorting to a single waveguide-fed slot that acted as the primary feed antenna. An ERA with peak directivity of 20dBi was reported that demonstrated 10% bandwidth [9]. Following this approach, two inductive PRSs were studied in [65,66]. The first PRS was composed of a printed array of metallic loops whereas the second consisted of an array of loops with two different sizes. In the latter the loops were interleaved such that in a given unit-cell, the larger loop enclosed the smaller one. These PRSs, when employed in ERAs fed with a single patch antenna, yielded a bandwidth of about 15% and 25% with the same level of peak directivity (≈ 14.5 dBi), respectively [66]. These methods, specifically the ones proposed in [66], involved a high degree of fabrication complexity, despite their effectiveness in improving the bandwidth. The PRS suffered from an inherent self-resonance that limited

the enhanced directivity to a maximum of 14.5 dBi [66]. Moreover, as the reflection phase response was due to the printed capacitive/inductive elements, the arrays printed on the PRS needed to be amply large to create a well-illuminated aperture that was essential to obtain high directivity. Thus, the footprint of these arrays was fairly large ($\approx 25\lambda_0^2$) and the resultant aperture efficiency was quite low.

2.8.2 Variable Reflection Profile and Metamaterial-based ERAs

The use of arrays with tapered-size elements was proposed in the following years [11, 79, 80, 87]. Two PRSs were studied in [11]. The first PRS had an array of square metal patches where the size of the patch as well as its periodicity was kept constant. In the second PRS, both the size of the patch and the periodicity were tapered to achieve a spatially-variable reflection profile. It was found that the ERA with the first PRS (with constant spatial reflection profile) provided narrowband response whereas the ERA with the second PRS achieved wider directivity bandwidth. It was suggested in [11] that as the rays in the cavity undergo multiple reflections, their phase is not constant but becomes a function of distance from the centre of the cavity. Consequently a PRS with fixed size elements is unable to provide optimal reflection phase to the rays within the entire cavity. However, when each element in the array is adjusted to provide a reflection phase that compensates for different path lengths, the total superimposed field can be made coherent and the condition for broadside radiation is satisfied over a wide bandwidth. An ERA designed using this method demonstrated a measured bandwidth of 8.5% with peak directivity approaching 19 dBi.

Following this approach, a few other designs were also proposed [11, 79, 80], including a theoretical model based on metamaterial PRS in [80]. It was proposed that if the refractive index of the PRS can be tailored such that its real component has a minimum at the centre and increases towards the edges, the spherical wave fronts within the ERA cavity may

be transformed to planar wave fronts to achieve high gain over a wider bandwidth. Such a design can be carried out using the effective-medium theory and S-parameter retrieval through periodic analysis. Numerical results predicting a peak directivity of 19 dBi over a bandwidth of 15.4% were reported. These methods improved the ERA bandwidth but the degree of complexity to design, replicate, and fabricate the process was significantly increased. Furthermore these designs were highly sensitive to fabrication tolerances as the aperture field could be altered by any undesired variations in lattice periodicity. This caused large shifts in operating bandwidths as well as fluctuation of directivity within the bandwidth that was visible in the measurements [11].

2.8.3 Multi-point Array-Fed ERAs

During the same period, improving the illumination of the PRS to create a large radiating aperture was studied as a means of improving the bandwidth of ERAs [10, 52, 99]. It was proposed that instead of a single feeding antenna, if an array of antennas is used to feed the resonant cavity of an ERA, high directivity as well as wide bandwidth can be achieved at the same time. This method utilizes the unused area in the cavity to achieve an efficient radiating aperture on the PRS. The main advantage is that the directivity is enhanced by both the array of feed antennas as well as the PRS, however, the bandwidth is mainly limited by the nature of the PRS. In [10], this technique was combined with a dual-resonator wideband PRS and a dense slot array to achieve 24 dBi peak directivity over 12.6% bandwidth. An array of 4×8 aperture coupled slots was used to uniformly excite the cavity formed by a PRS composed of 3 unprinted multilayered dielectric slabs. A configuration involving the application of an artificial magnetic conductor (AMC) ground plane with a similar configuration was also studied to reduce the profile of the resulting antenna, in addition to bandwidth enhancement [99]. However, these methods make the design of the ERA significantly complex due to the induction of a feeding network required

by the array. Thus, simple configuration and single source feeding, the two most attractive characteristics of ERAs, are compromised.

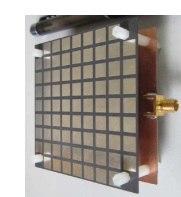
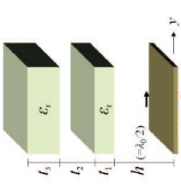
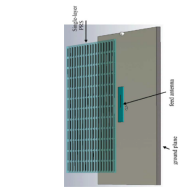
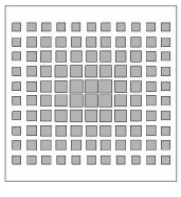

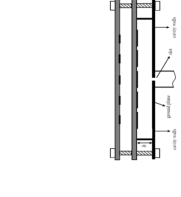
2.8.4 Complementary FSS-based ERAs

As methods stated previously are accompanied by increased profile of the ERAs, single layer PRSs able to provide bandwidth and high directivity have become increasingly attractive in recent times [12, 14, 100, 101]. Thin PRSs that provide positive reflection phase gradients over a wide band were investigated for use with ERAs [12]. The PRSs investigated were composed of a single dielectric sheet with 2-D arrays printed on both sides. The idea was to make the ERA low-profile as well as wideband. As an example, dipole arrays were considered where the size of the dipoles for each side of the PRS was different. The parameters of the dipoles were optimized according to the proposed design method to achieve positive reflection phase gradients within a designated frequency band. This PRS, when used to form an ERA, provided a peak gain of 16 dBi over a bandwidth of nearly 12.6%. Three PRSs were studied where each had a different set of parameters for the printed elements.

Recently, an ERA having a double-sided printed PRS was proposed in [14]. The PRS used complementary inductive and capacitive grids made out of printed patch-type and slot-type FSS printed on the sides of a single dielectric sheet. Transmission line modelling was used to extract the values of the reactive elements that led to a positive reflection. To feed this ERA, a low profile aperture coupled parasitic patch served as a sophisticated wideband feed. This ERA demonstrated a bandwidth as wide as 28%, however, the peak directivity was only 13.8 dBi.

A quantitative comparison of some ERAs discussed in the preceding sections is presented in Table 2.1 to provide insights for the readers. It can be inferred from this review that enhancing ERA bandwidth has challenged researchers over the last decade. For peak

Table 2.1: Quantitative summary of bandwidth enhancement of ERAs in the last decade.

							Ref. [9]	Ref. [10]	Ref. [11]	Ref. [12]	*Ref. [13]	Ref. [14]
Directivity	10	12	8.5	12.6	19.3	28						
Bandwidth (%)												
Peak	20	24	19	16	17	13.8						
Directivity (dBi)												
Footprint (λ_0^2)	25	36	12.3	20.5	Infinite	5.8						
Feed	Slot	4×8	Reactive	Printed	Hertzian	Aperture						
Antenna		Slot Array	Loaded patch	Monopole	Dipole Patch	Coupled						

**theoretically proposed design; predicted performance is quoted.*

antenna directivity exceeding 15 dBi, the figures for bandwidth somewhat rest at around 15%. Conventionally, it has been observed in the past that ERA directivity and bandwidth follow an inverse relationship. However, for practical applications, both these factors are critical and require simultaneous enhancement. Therefore, in this dissertation, methods to achieve wide bandwidth and high antenna directivity (>15 dBi) are introduced and examined in detail. While achieving worthwhile antenna performance in terms of ERA bandwidth and peak directivity, simplicity of configuration as well as the advantage of a single feed source are also preserved to make the designs low-cost and attractive.

2.9 Potential Applications

Potential applications of ERAs range from local multi-point distribution systems (LMDS) and satellite reception, to high-speed mm-wave wireless local area networks (WLANs). As stated earlier, their prime advantage is their ability to provide high gain without relying on complex feed networks and secondary reflectors. Reflector antennas are large and bulky, whereas arrays require feeding networks which are complex to design. Moreover, the feeding networks are expensive to operate due to the cost of associated components (such as phase shifters, couplers and, power dividers) and incur losses specially at higher frequencies. However, it should also be noted that ERAs proposed in this dissertation, as well as ERAs in general, are not meant to replace the conventional high gain antennas such as reflectors, lens antennas, and antenna arrays. Instead, they are a convenient alternative specially in space-constrained applications where robustness, performance, and aesthetic appeal are equally important. In most cases, ERAs are deemed suitable for medium-gain applications that require gain in the range of 15-25 dB.

ERAs feature low-cost fabrication and deployment. A notable application for these antennas is in high-wind coastal regions where sparse populations are distributed over

diverse topographies. This is mostly the case in South America and Australia. Small antenna footprint in coastal terrain provides better wind and weather resilience. More recently, these planar antennas are being viewed as potential candidates for broadband last-mile access, 60GHz wireless backhaul and mm-wave applications. A particularly interesting application of ERAs is as interleaved feed for the focal array-fed reflector (FAFR) antennas. Multi-beam FAFRs are used in defence, satellite, and radio astronomy applications around the world. Some potential applications largely focussing on the future Australian² consumer market are

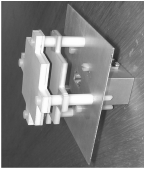
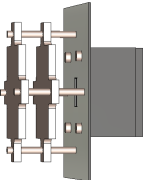
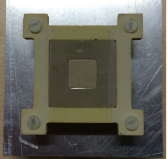
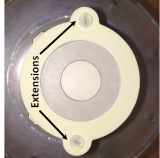
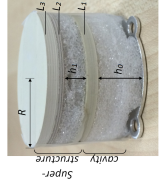
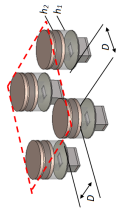
- High-speed access to the Australian National Broadband Network (NBN) backbone for remote areas.
- Point-to-point high-speed fixed wireless links for NBN backhaul.
- Low-cost deployment of broadband links on the coastal belts.
- Aesthetic solution for Building-to-Building high-speed connectivity in metropolitan areas.
- Indoor nodes for 60GHz Wireless LAN applications.
- Interleaved dual-band *X-band* and *Ku-band* radars.
- Potential feeds for medium range, high resolution radio telescopes and weather stations.

²Australian Communications and Media Authority (ACMA) reports in its 2013-17 Spectrum Outlook that in December 2012 more than 50% of all Australian internet connections were wireless including mobile and fixed stations. This equals all wired (digital subscriber line, cable, fibre and dial-up) connections combined that is a dramatic market reshape in just six years (in June 2006 the Australian wireless access share was only about 2%) [102].

2.10 Summary of Proposed Designs

Table 2.2 presents a quantitative overview of some designs proposed in this dissertation. Comparing Table 2.1 and Table 2.2, it is evident that the proposed designs demonstrate a marked increase in bandwidth as well as a significant reduction in the antenna footprint. For a peak directivity greater than 15 dBi, the figure for bandwidth of single-feed ERAs exceeds 50%, which previously rested at around 15%. Compared with the bandwidth of classical single-feed ERAs [4–8], this represents an improvement of nearly two orders of magnitude. To the best of the author’s knowledge, no other class of directive antennas offers such a large bandwidth with a single feed, alongside high gain, simplicity and versatility as demonstrated by these ERAs, while possessing such small footprint areas. The superstructures employed in these antennas are made out of planar, unprinted dielectric slabs which lead to good aesthetics and low production cost. Their small area translates into low weight, low material cost and better wind resistance. Other performance figures such as overall efficiency, aperture efficiency, side-lobe levels and cross-polarization levels, as will be described in the following Chapters, were also found to be very promising.

Table 2.2: Summary of some wideband designs proposed in this dissertation.

						
Chapters	3	4	5	5	6	7
Directivity	22	14.1	43	52.9	27	37
Bandwidth (%)						
Peak	18.2	17.5	15.5	16.4	15.6	21.3
Directivity (dBi)						
Footprint (λ_0^2)	2.25	2.25	2.4	1.77	1.7	-

Chapter 3

Wideband ERAs with Multi-layer Dielectric Superstructures

3.1 Abstract

A novel method is presented to design single-feed high-gain EBG resonator antennas (ERAs) with significantly wider bandwidths. Dielectric contrast is introduced to 1-D EBG superstructures composed of unprinted dielectric slabs and the thicknesses of each of these slabs are optimized to achieve a wideband defect mode in a unit-cell model. Next, antennas are designed and their superstructure areas are truncated to increase the antenna bandwidth and aperture efficiency while decreasing antenna footprint. We demonstrate that a small superstructure area increases the 3dB bandwidth of ERAs significantly. A prototype ERA designed with a single feed and superstructure area as small as $1.5\lambda_0 \times 1.5\lambda_0$ has a measured 3dB directivity bandwidth of 22% at a peak

Published as: R.M. Hashmi, B.A. Zeb and K.P. Esselle, "Wideband high-gain EBG resonator antennas with a small footprints and all-dielectric superstructures," *IEEE Transactions on Antennas and Propagation*, vol. 62, No. 6, pp. 2970-2977, 2014.

gain of 18.2 dBi. This prototype antenna was made out of three slabs of different dielectric constants, two of them touching each other. This prototype demonstrates more than 85% reduction in the ERA footprint alongside a drastic improvement in bandwidth over the 3-4% measured bandwidth of the classical single-feed ERAs with unprinted slabs.

3.2 Introduction

Electromagnetic band gap (EBG) structures exhibit unique characteristics to guide, filter or collimate electromagnetic waves and have attracted a lot of interest from the research community in recent years [7, 8, 23, 31, 36, 103, 104]. Particularly, their antenna applications in suppressing surface waves, reducing antenna profile [31, 103] as well as forming highly directive antennas have been of considerable interest [4, 5, 7, 8, 36, 104]. EBG Resonator Antennas (ERAs), also known as Fabry-Perot cavity antennas, are well known for their ability to increase broadside directivity of simple antennas without resorting to complex feed networks as in phased arrays. Although pioneering research on this concept was published by Von Trentini in 1956 [36], Jackson et al. were the first to propose the use of unprinted dielectric slabs as superstrates for gain enhancement in 1985 [37, 92]. The recent surge of research in EBG and periodic structures inspired many researchers to revisit this concept and make significant advances. A common ERA consists of an air-filled half-wavelength cavity formed between a perfect reflector (e.g., metallic ground plane or AMC) and a high-reflectivity top. This top section can take various forms, depending upon the design methodology and fabrication technology, including 3-D EBG structures [7], 2-D printed frequency selective surfaces [9, 12, 65–67] or stacks of unprinted dielectric slabs [8, 10, 59, 89]. Here we use the general term superstructure to refer to all such top sections. The operating mechanism of such antennas is often explained using the

defect-mode transmission [4], Fabry-Perot resonance condition [5], leaky-wave analysis [92] or transmission line theory [37].

A variety of superstructures have been investigated, both theoretically and experimentally. Their size reduction [54, 55], frequency reconfiguration [58], beam steering [61–64] as well as bandwidth enhancement [9–12, 65–68] have been addressed for applications such as mobile base stations, global satellite coverage, feed clusters for multiple-beam antennas in space applications, and point-to-point microwave links. In order to obtain high gain, sufficiently strong superstructure reflectivity (typically >0.6) is required [5]. High superstructure reflectivity results in a high-Q resonant cavity. Therefore, the resulting single-feed antennas are highly directive but innately narrow-band. To improve the 3dB gain bandwidth, various attempts have been made, but all of them can be classified into two basic categories:

1. *Distributed Source Excitation*: Using multiple feed points, e.g., sparse array feed for more uniform illumination of the cavity, thus, increasing aperture efficiency.
2. *Modification of Superstructure*: Designing the superstructure to increase the defect-mode bandwidth or optimize superstructure reflection coefficient.

The second category is of particular interest and has been applied for partially reflecting surfaces (PRS) [9, 11, 12, 65–67] as well as unprinted dielectric slabs with identical permittivity and thickness [10, 68]. The most notable milestones reached, despite the design complexity, include achieving 3dB gain bandwidths up to 12% with printed PRSs excited by a single feed [9, 12, 66] and 3dB bandwidth of 12.6% from a dual-resonator unprinted structure excited by a 4×8 slot array feed [10]. Employing unprinted dielectric slabs to design EBG structures is attractive since it directly translates into structural simplicity and ease of fabrication. This also allows for easy extension of a linearly-polarized antenna to dual-linear and circular polarization.

This paper presents the detailed design process for ERAs that have significantly wider bandwidths, up to 30%. The defect cavity model (DCM) [4, 42, 105] and superstrate reflection model (SRM) [9, 12, 81] are used in conjunction to design wideband ERA superstructures. Conventionally, the unit-cell design of ERA superstructures is carried out either using the DCM or the SRM, both of which assume periodic boundary conditions (PBC). Although for narrow-band ERA designs (5-6% bandwidth) employing any one of these models in isolation is sufficient, we show that for wideband ERAs (>15% bandwidth), limiting the design process to only DCM or SRM can be misleading. To the best of our knowledge, this has not been addressed in the literature and limits understanding of wideband superstructure design and its feasibility as an ERA superstrate.

We begin with characterizing the EBG superstructure using DCM and use parametric analyses to achieve a wide defect-mode bandwidth (DMB) i.e., transmission bandwidth where $|\tau_{DCM}| > 0.7$. The defect modes are created by varying the thickness, inter-slab separation and permittivity of the slabs in the superstructure. Once a wide DMB is achieved, we evaluate the suitability of the superstructure as an antenna superstrate using the SRM. Next, the area of the superstructure is severely truncated through a parametric study to increase ERA's 3dB bandwidth and gain while minimizing the footprint. It is to note that for keeping the design highly practical, the thicknesses and dielectric constants of the slabs are always selected to match commercially available values. Other associated parameters such as the slab separations have been fine tuned.

The initial superstructure (S-I) consists of two slabs of thickness (t_1, t_2) and relative permittivity (ϵ_1, ϵ_2) , separated by spacing h_1 . It is similar to the superstructure shown in Fig. 4.1 with Layer 3 (L_3) removed. After showing that S-I is not suitable for wideband ERAs, a third slab is introduced to design a three-layer superstructure (S-II), shown in Fig. 4.1, to improve $|\Gamma_{SRM}|$ over a wide DMB. Two types of S-II superstructure are employed to design wideband ERAs. They are severely truncated to increase the antenna

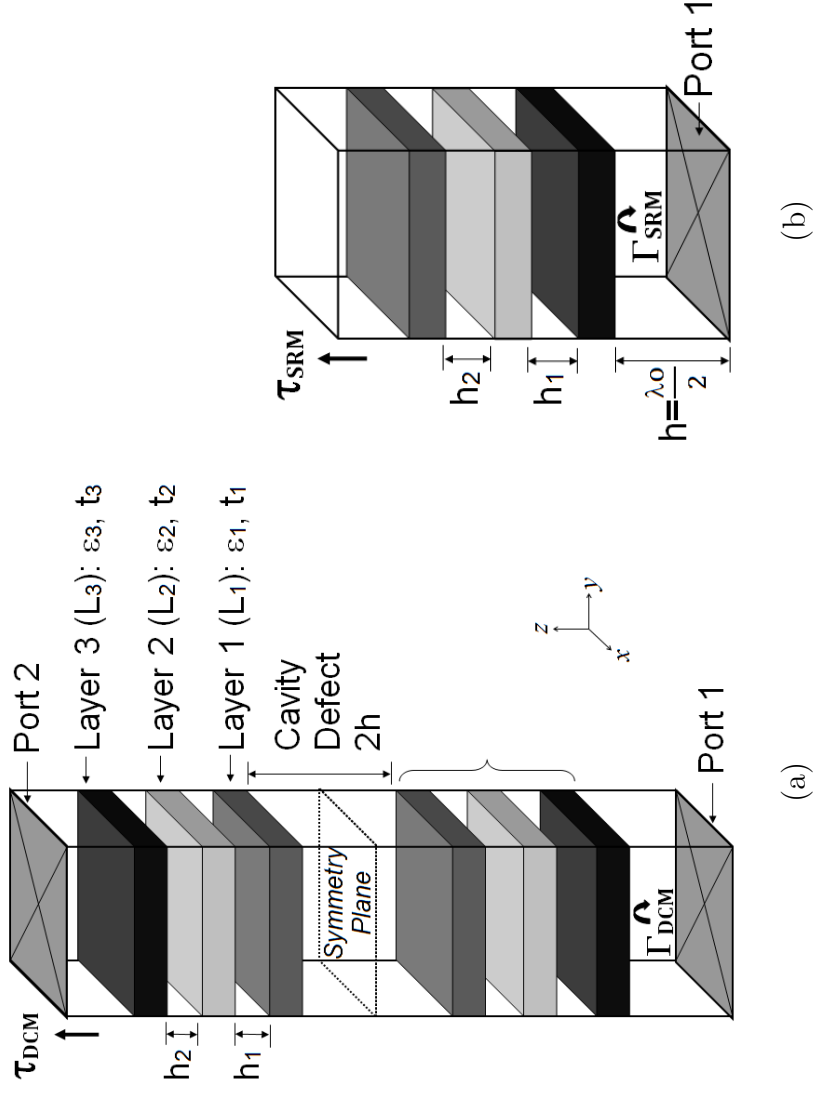


Figure 3.1: Unit cell models of the proposed S-II wide defect-mode EBG Structure (a) defect cavity model (DCM) to calculate transmission ($|\tau_{DCM}|$) through the structure (b) superstructure reflection model (SRM) to characterize the reflection profile ($|\Gamma_{SRM}|, \angle\Gamma_{SRM}$). Inter-slab spacing h_1 and h_2 are set to quarter-wavelength.

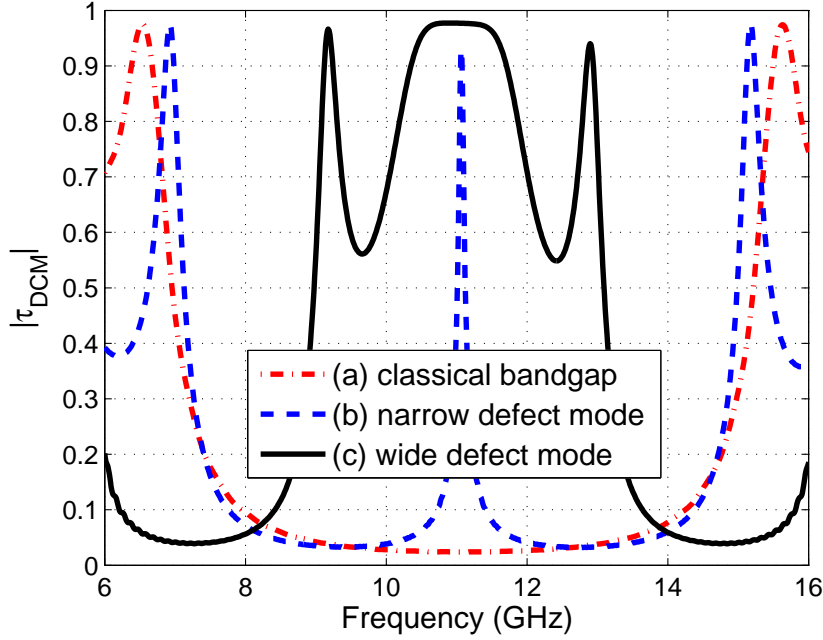


Figure 3.2: Transmission of (a) a classical EBG structure that consists of four identical dielectric slabs ($\epsilon_1 = \epsilon_2 = 9.2, t = 0.25\lambda_g, h_1 = 0.25\lambda_0, 2h = 0.25\lambda_0$ i.e. no defect), (b) DCM of a narrowband periodicity defect structure ($\epsilon_1 = \epsilon_2 = 9.2, t = 0.25\lambda_g, h_1 = 0.25\lambda_0, h = 0.5\lambda_0$) and (c) DCM of a wideband defect-mode structure ($\epsilon_1 = \epsilon_2 = 9.2, t = 0.5\lambda_g, h_1 = 0.25\lambda_0, h = 0.5\lambda_0$) $f_0 = 11.1$ GHz.

bandwidth further and achieve 85% less ERA footprint compared to the classical ERAs (which are $20 - 36\lambda_0^2$), yet with 22% measured 3dB bandwidth and 18.2 dBi gain.

3.3 Theoretical Basis and Unit-Cell Characterization

It is well known that defects can be introduced in EBG structures to form allowed frequency bands (defect modes) within the band gap [4, 7, 8, 104]. The frequency response of such a 1-D EBG structure is typically characterized by the theory of multi-layer structures, which reveals that the defect acts as a narrow band-pass filter, whose frequency selectivity and performance are determined by Q-factor of the formed cavity and its ma-

terial properties [7]. The reciprocal space analysis [40] shows that an EBG structure with defects behaves as a spatial filter in which the defects restrict the modes to certain directions (e.g., $\pm z$ directions). These radially evanescent modes can further be restricted to one direction (e.g., $+z$ direction, i.e., broadside) by inserting a perfect reflector (e.g., PEC ground) at the symmetry plane of the defect EBG structure. We investigate the concept of multiple defects with closely spaced resonant frequencies to achieve a wide pass-band. This is useful to form a wide defect mode in a cavity resonator, which can later be used to design a wideband ERA.

3.3.1 Forming a Wide Defect-Mode Cavity Resonator

The classical 1-D EBG superstructure consists of two or more slabs of identical quarter-wave thickness and permittivity, separated $\lambda_0/4$ apart [4, 8]. This superstructure has a narrow defect-mode bandwidth and thus the 3dB bandwidth of the resulting ERA is no more than 3-4%. For example, the transmission through DCM of S-I has a narrow defect-mode shown by curve (b) in Fig. 3.2 when the thickness t is set to $0.25\lambda_g$. Now, using parametric analyses, thickness of each slab (t_1, t_2) and the separation (h_1) between them are changed to widen this defect-mode, as shown by curve (c) in Fig. 3.2. It is seen that the DMB has increased from 1.8% to 18%, which according to [4, 8, 40] suggests that S-I, when employed as an antenna superstrate, should result in a wideband ERA with 3dB directivity bandwidth close to 18%. However, we will show that this is not a sufficient condition for wideband ERA designs.

As the Fabry-Perot resonance condition requires the reflection phase of the superstrate ($\angle\Gamma_{SRM}$) to increase with frequency [5], following the ideal curve shown in Fig. 3.3, it is desirable to control the slope of $\angle\Gamma_{SRM}$. For this purpose, a slight permittivity contrast ($\Delta\epsilon = |\epsilon_1 - \epsilon_2|$) between the slabs is used to control the ascent of $\angle\Gamma_{SRM}$. Dielectric contrast and physical thickness provide the required control of $\angle\Gamma_{SRM}$ and the curves in

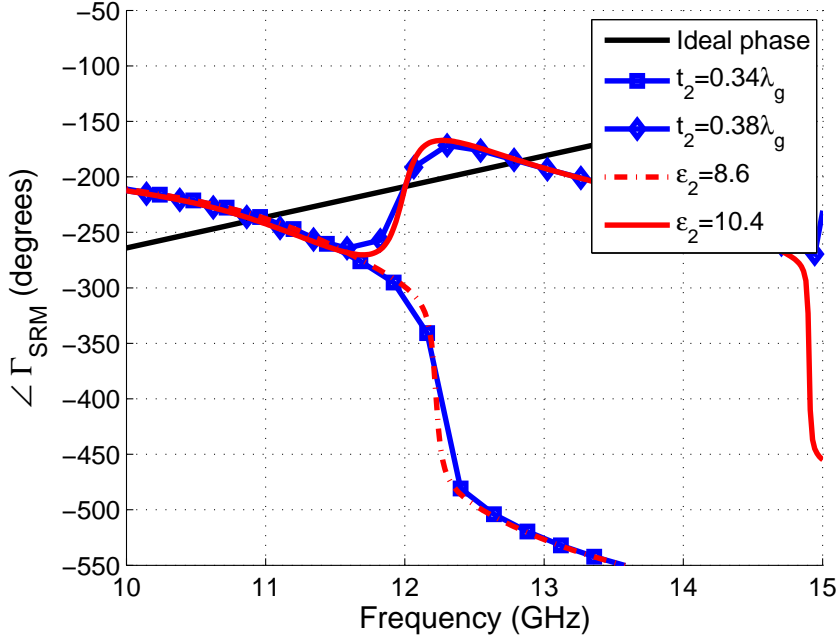


Figure 3.3: Effects of permittivity and thickness variation on $\angle \Gamma_{SRM}$. The curves are obtained through SRM with $h = 0.5\lambda_0$ and $h_1 = 0.4\lambda_0$. Initial parameters are $\epsilon_1 = \epsilon_2 = 9.2$ and $t_1 = t_2 = 0.36\lambda_g$. Then either t_2 or ϵ_2 is changed to the value shown in the legend.

Fig. 3.3 establish the equivalence between permittivity and thickness contrast. Note the interesting inversion of the phase gradient when $t_2 \geq t_1$ and the converse when $t_2 \leq t_1$. On the other hand, fixing ϵ_1 and slightly varying ϵ_2 provides similar results to those of varying the thickness.

3.3.2 Evaluating Feasibility as Antenna Superstrate

In addition to the wide DMB, for a wideband ERA, it is necessary to have sufficiently high reflection magnitude ($|\Gamma_{SRM}| > 0.6$) over the entire DMB. Otherwise, the directivity of ERA does not remain within 3dB from the maximum over the DMB, thereby, reducing the 3dB directivity bandwidth. The $|\tau_{DCM}|$ curves of S-I computed using the DCM (Fig. 4.1

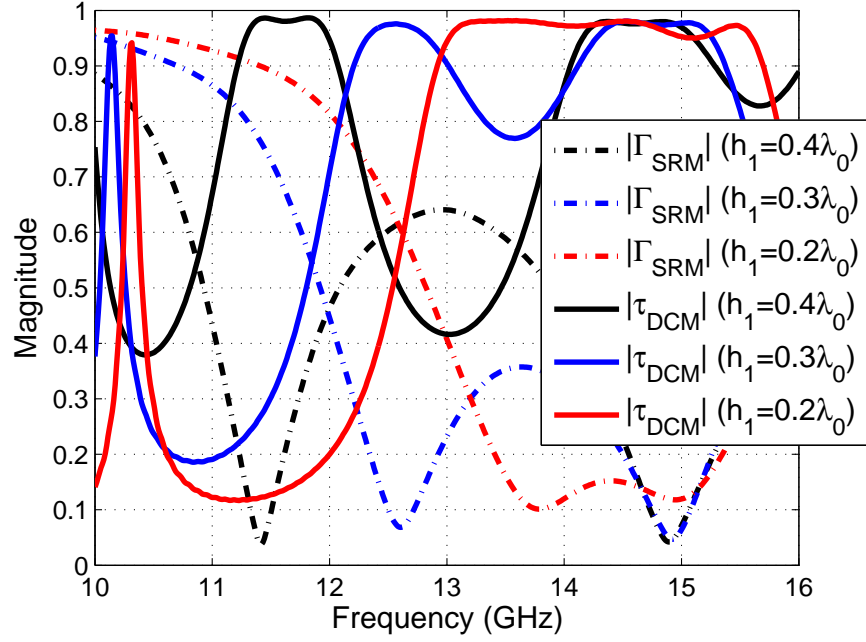


Figure 3.4: Reflection ($|\Gamma_{SRM}|$) and transmission ($|\tau_{DCM}|$) obtained by SRM and DCM. The curves are obtained for different values of separation h_1 between slabs L_1 and L_2 with $t_1 = t_2 = 0.36\lambda_0$, $\epsilon_1 = 9.2$, $\epsilon_2 = 9.8$, $2h = \lambda_0$.

(b)) are plotted in Fig. 3.4. The $|\Gamma_{SRM}|$ for the same thickness values are also plotted to compare and analyze the suitability of S-I as an ERA superstructure. Note that for each curve of $|\tau_{DCM}|$, the corresponding $|\Gamma_{SRM}|$ curve shows a significant drop within the DMB. This drop eventually reduces the directivity bandwidth of the resulting ERA and hence must be rectified. The reason for this drop is the resonance of the secondary cavity formed by the air gap h_1 , that makes the superstructure nearly transparent at the respective resonance frequencies (f_r). In this situation, the wide DMB of S-I does not lead to a wideband ERA. The comparison in Fig. 3.4 shows clearly that limiting the wideband ERA design process to DCM in isolation can be misleading as in the case of S-I. Hence, a wideband defect-mode alone is not sufficient; significant SRM reflection magnitude is also required over the DMB for wideband ERA design.

3.3.3 Inclusion Layer and Formation of S-II

A three-layer superstructure is now considered by adding another low permittivity layer to S-I between L_1 and L_2 , to remove superstructure transparency at f_r . This new superstructure is referred to as S-II and is shown in Fig. 4.1. Following the approach laid out in Section II.A, we use parametric analyses to reach the values: $t_1 = 0.26\lambda_g$, $t_2 = 0.36\lambda_g$, $t_3 = 0.26\lambda_g$ with $\epsilon_1 = 9.2$, $\epsilon_2 = 4.5$ and $\epsilon_3 = 9.8$. The separations between the slabs is set to $h_1 = 0.25\lambda_0$ and $h_2 = 0$, resulting in the formation of a composite slab with L_2 touching L_3 . For S-II, $|\Gamma_{SRM}|$ and $|\tau_{DCM}|$ magnitudes are plotted in Fig. 3.5. A wide defect-mode can be noticed for $h_2 = 0$ with a DMB of 13%. S-II shows a strong SRM reflection magnitude over the DMB and fulfills the conditions required for a wideband ERA superstrate. The reflection phase of S-II, not shown here for brevity, was also found to increase with frequency within the DMB similar to the results shown in Fig. 3.3.

3.4 Wideband ERA Design

A wide defect-mode superstructure is now employed to form an ERA by placing it at a height of $h = \lambda_0/2$ above a conducting ground plane. The goal is to exploit the wide defect-mode bandwidth obtained by the unit-cell analysis of an infinite structure (in the previous section) to achieve a wide antenna bandwidth and then to increase it by truncating the superstructure optimally. The proposed ERA was designed using the CST Studio and further validated in ANSYS-HFSS. Initially, a horizontal electric dipole (HED) was used as the broadband excitation source to predict the radiating characteristics. Later, a waveguide-fed slot antenna was designed to provide impedance matching ($|S_{11}| \leq -10$ dB) over the entire operating band of 10 – 15GHz. In this section, the key parameters associated with the antenna design such as the choice of dielectric combinations for S-II, area of the superstructure and the ground plane, as well as the crucial step of input

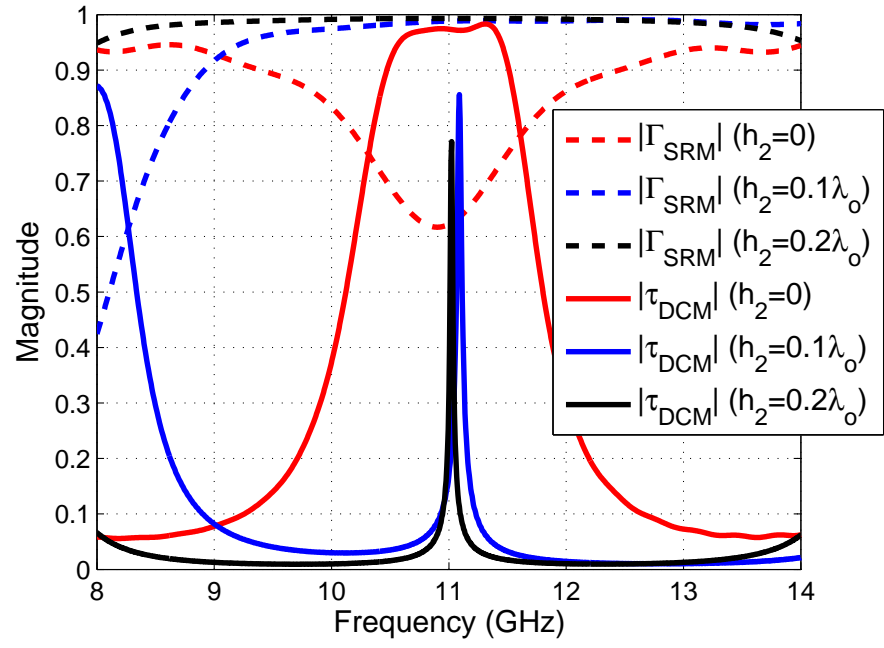


Figure 3.5: Reflection ($|\Gamma_{SRM}|$) and transmission ($|\tau_{DCM}|$) magnitude with the third slab in the superstructure, computed using SRM and DCM for various gaps h_2 . L_1, L_2 and L_3 parameters: $\epsilon_1 = 9.2$, $\epsilon_2 = 4.5$, $\epsilon_3 = 9.8$, $t_1 = 0.26\lambda_g$, $t_2 = 0.36\lambda_g$, $t_3 = 0.26\lambda_g$, $h_1 = \lambda_0/4$, $2h = \lambda_0$.

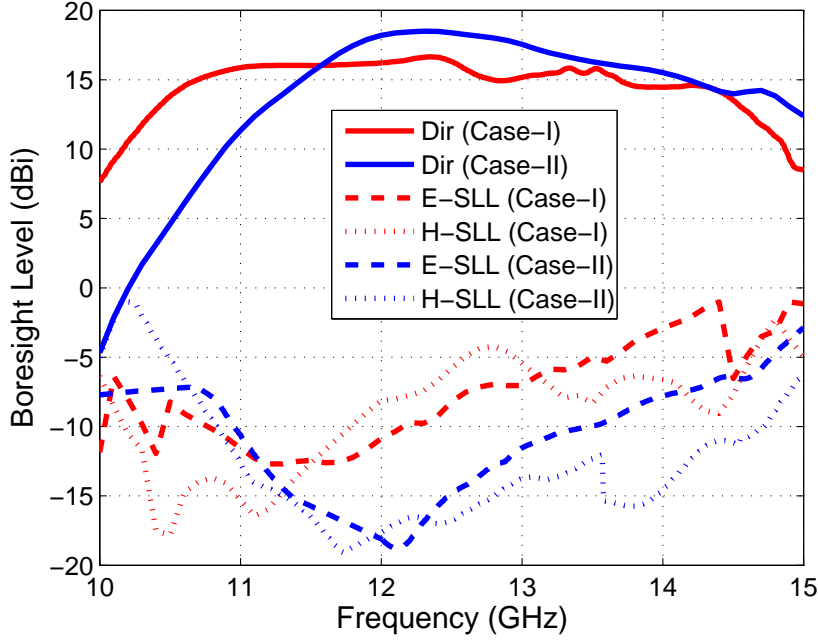


Figure 3.6: Predicted boresight directivity and side lobe level (SLL) for Case-I and Case-II antenna superstructures truncated to $1.5 \times 1.5\lambda_0^2$. The superstructures have additional $10 \times 10 \text{ mm}^2$ extensions on each edge to place nylon spacers, as shown in Fig. 6.1.

impedance matching are discussed.

3.4.1 Choice of the Permittivity Combinations

Another case of S-II is considered here to address economy of the design in which the permittivity combination is reversed to employ low permittivity slabs. Explicitly, the following two cases were considered for antenna design:

1. *Case-I*: $\epsilon_1, \epsilon_3 \gg \epsilon_2$ where $\epsilon_1 \neq \epsilon_3$
2. *Case-II*: $\epsilon_1, \epsilon_3 \ll \epsilon_2$ where $\epsilon_1 \neq \epsilon_3$

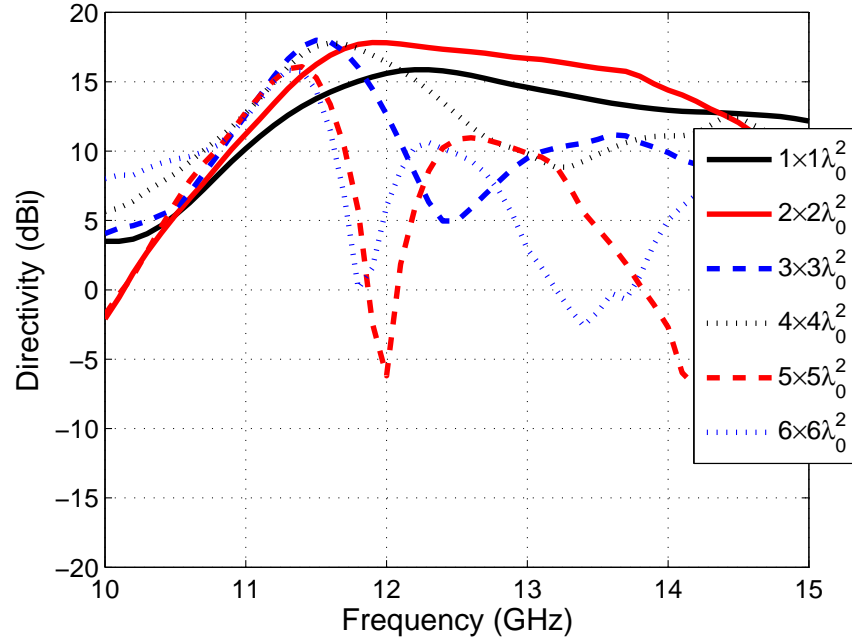


Figure 3.7: Predicted boresight directivity for various superstructure areas of an ERA with S-II (Case-II) superstructure, without extensions.

The final design parameters for these cases, chosen based on commercial availability, are shown in Table 3.1. The computed directivity for Case-I and Case-II are shown in Fig. 3.6. In unit-cell analyses, both the cases exhibited wide DMBs and strong reflection magnitudes. However, the $|\Gamma_{SRM}|$ for Case-II (not shown here) was stronger (>0.8) and its DMB was slightly less compared to Case-I. Owing to this, higher peak directivity can be obtained with Case-II, yet with a predicted 22.5% 3dB directivity bandwidth as shown in Fig. 3.6. The corresponding side lobe levels (SLL) on E- and H- planes are also plotted in Fig. 3.6 to highlight the difference between the two designs. The computed SLLs within the 3dB bandwidth are far better for Case-II compared to those of Case-I. Based on the goal to increase both the directivity and 3dB bandwidth, while having low SLL, Case-II was chosen for further investigations. This choice also brings in an economical advantage since it is largely based on lower permittivity materials, and is thus less expensive.

Table 3.1: *Design parameters for Case-I and Case-II*

	ϵ_1	ϵ_2	ϵ_3	t_1 (mm)	t_2 (mm)	t_3 (mm)	h_1 (mm)
Case-I	9.2	4.5	9.8	2.29	3.175	2.29	6.5
Case-II	3.27	10.5	4.5	3.175	1.27	3.175	6.5

3.4.2 Superstructure Area and Directivity Bandwidth

Various superstructure areas from very small to very large were considered in the ERA design to quantify the effect of truncation on 3dB directivity bandwidth. The computed boresight directivity for several superstructure areas is plotted in Fig. 3.7. The primary cavity height is $h = \lambda_0/2$ at $f_0=11.1$ GHz. From Fig. 3.7, it can be deduced that smaller areas provide wider 3dB directivity bandwidths. For example, 22.5% bandwidth and good SLL is possible using Case-II with a superstructure area as small as $1.5\lambda_0 \times 1.5\lambda_0$. For applications where the SLL can be compromised to levels as high as -4.5 dB, 3dB directivity bandwidth can be further increased up to about 30% (with the same superstructure area) by employing a Case-I superstructure, as indicated in Fig. 3.6.

It was found that provided the $|\Gamma_{SRM}|$ is strong enough (as discussed in Section II), the DMB (obtained from the DCM of an infinite structure) approximately predicts the 3dB directivity bandwidth of a finite antenna when the superstructure area is medium ($\approx 9 - 16\lambda_0^2$). For example, the DMB of Case-I is 12% and the corresponding antenna bandwidth with $4 \times 4\lambda_0^2$ superstructure is 11%. Similarly, the DMB of Case-II is 7% and the corresponding $3 \times 3\lambda_0^2$ antenna's bandwidth is also 7%. However, this bandwidth can be further increased significantly by truncating the superstructure to a smaller area as shown in Fig. 3.7. When the superstructure area is increased significantly (e.g., $36\lambda_0^2$), lateral propagation within the cavity and phase non-uniformity across the aperture cause

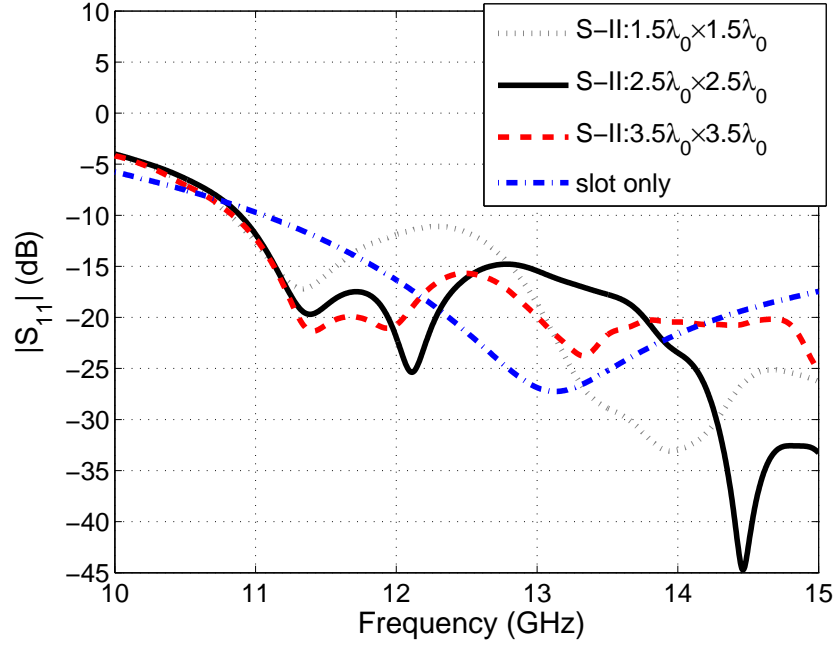


Figure 3.8: *The computed input reflection coefficients of the waveguide-fed slot antenna with various superstructures are compared with that of the radiating slot without a superstructure.*

a degradation in the antenna directivity bandwidth.

Given the superstructure length is suitably small ($1.5\lambda_0 - 2\lambda_0$), the waves leaking from the edges also contribute to increase the 3dB bandwidth. In addition, with a single excitation point, most of the radiation comes from the centre of the superstructure forming an approximately circular effective radiating aperture. As the superstructure area is increased, lateral propagation of the cavity field becomes significant. Cavity fields are very weak outside the “effective aperture” area and the aperture efficiency of such antennas is poor. Hence, a very small aperture area of $1.5\lambda_0 \times 1.5\lambda_0$ is chosen here to obtain increased ERA bandwidth. Below this size, the cavity leaks excessively from sides, significantly degrading the peak directivity and SLLs. In addition to the increase in bandwidth, the use of compact superstructure ($1.5\lambda_0 \times 1.5\lambda_0 = 2.25\lambda_0^2$) provides more than 85% reduction

in ERA footprint compared to the classical ERA designs $(20 - 36\lambda_0^2)$ [9, 12, 66].

3.4.3 Feed Antenna and Input Matching

For an ERA to radiate efficiently and to obtain 3dB gain bandwidth close to the 3dB directivity bandwidth, it is necessary to match the antenna input to a standard 50Ω feed-line over the entire 3dB directivity bandwidth. For this purpose, a single waveguide-fed slot antenna was designed. The dimensions of the slot are $7.5 \times 12.5\text{mm}^2$ and it is cut in centre of the conducting ground plane. The slot is fed by a 50Ω WR-75 waveguide-to-coax adapter. The computed input reflection coefficient magnitude at the coax input ($|S_{11}|$) for various superstructure areas is shown in Fig. 3.8. To demonstrate the loading effect of the superstructure on the feed antenna, the reflection coefficient of slot antenna without the superstructure is also plotted. It is observed that, from 11 GHz, the antenna remains well-matched for all slab sizes considered.

3.5 Measurements and Results

A prototype ERA with S-II (Case-II) as the superstructure, shown in Fig. 6.1, was fabricated for experiments. The dielectric materials were Rogers TMM 3 ($\epsilon_1 = 3.27, t_1 = 3.175$ mm), RT/Duroid 6010.5 ($\epsilon_2 = 10.5, t_2 = 1.27$ mm) and Rogers TMM 4 ($\epsilon_3 = 4.5, t_3 = 3.175$ mm). The loss tangent of the materials used is $\tan\delta = 0.002$. The slab dimensions are $40 \times 40\text{mm}^2$. Four small extensions, $10 \times 10\text{mm}^2$ in area, were provided to place nylon spacers for holding the superstructure above an aluminium ground plane, which is $75 \times 75\text{mm}^2$. The parameters h and h_1 (see Fig. 4.1) were set to 13.5 mm and 6.43 mm, respectively. The input reflection coefficient ($|S_{11}|$) was measured using a HP8720D Vector Network Analyser and the radiation characteristics were measured in the NSI-700S-50 spherical near-field measurement system at Australian Antenna Measurement

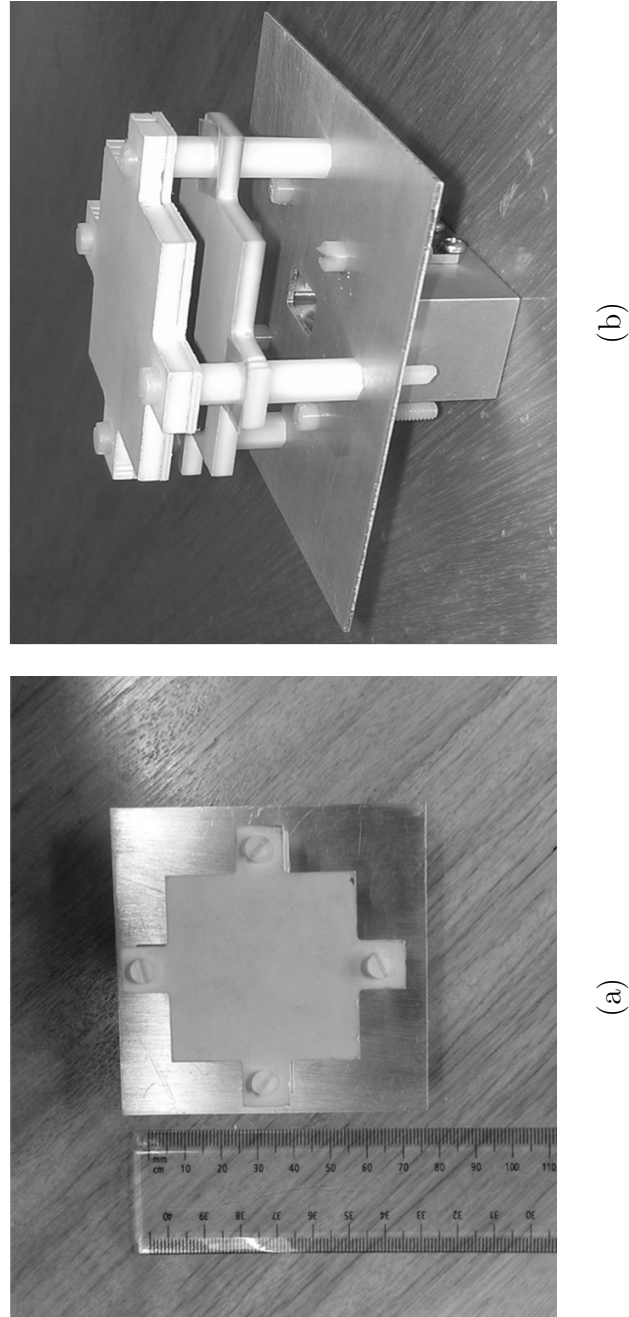


Figure 3.9: Prototype of the compact wideband ERA which has a superstructure area of only $1.5\lambda_0 \times 1.5\lambda_0$. A waveguide-to-coax connector is used to feed the antenna (a) top view (b) side view

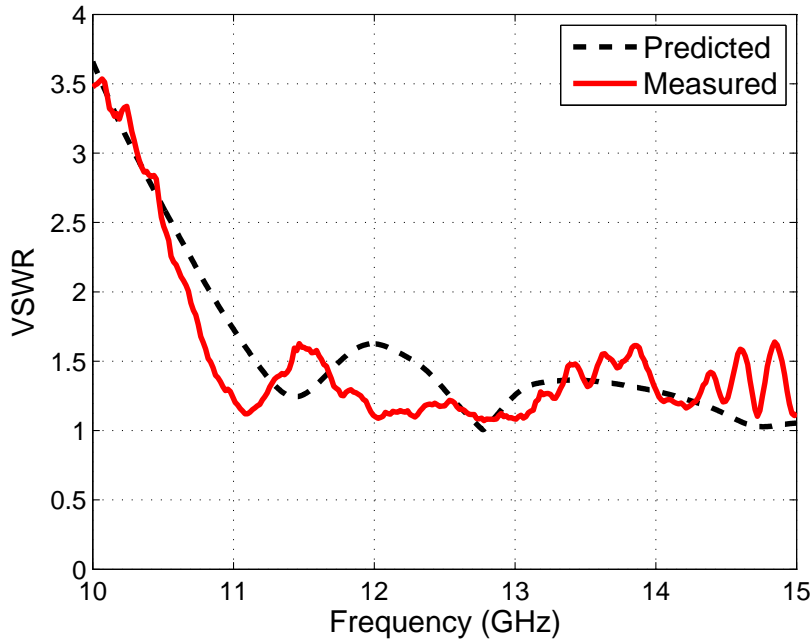


Figure 3.10: *Measured VSWR of the prototype ERA with a single slot feed compared with the predicted VSWR.*

Facility (AusAMF).

3.5.1 Input Impedance Matching

The measured voltage standing wave ratio (VSWR) of the ERA is shown in Fig. 3.10. Input matching is very good ($\text{VSWR} < 2$) at all measured frequencies above 10.7GHz. The measured results agree well with the predicted results from full-wave CST simulations.

3.5.2 Measured Directivity and ERA Gain

The peak gain of the fabricated ERA was measured using the gain comparison method with a WR-75 standard gain horn. To investigate the effect of the ground plane size, the antennas were measured using both a smaller ground plane ($75 \times 75 \text{ mm}^2$) and a slightly larger ground plane ($100 \times 100 \text{ mm}^2$). It was observed that the smaller ground

Table 3.2: *Summary of measured performance of the wideband ERA at four frequencies.*

f (GHz)	11.0	11.8	12.6	13.4
θ_{3dB} E-plane (degrees)	24	18	18	20
θ_{3dB} H-plane (degrees)	18	20	18	16
SLL E-plane (dB)	-9.8	-14.5	-16.9	-12.4
SLL H-plane (dB)	-16.5	-17.0	-19.0	-12.0
Radiation Efficiency (%)	92.4	88.3	83.4	95

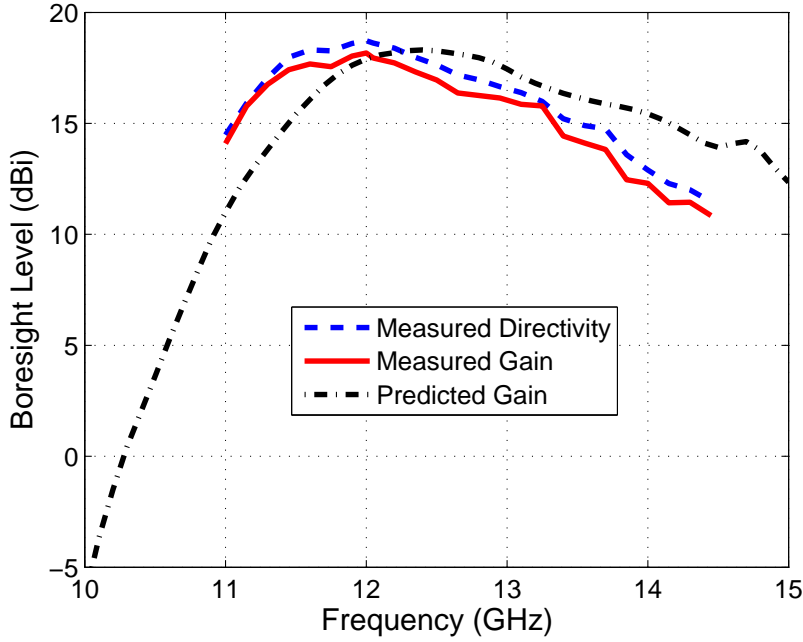


Figure 3.11: Measured gain and directivity of the fabricated ERA prototype, compared with the gain predicted from full-wave simulation. The area of aluminum ground plane is $75 \times 75 \text{ mm}^2$.

plane provided better gain-bandwidth product compared to the larger option. We also found that the ground plane area may be further reduced to match the small area of the superstructure, without significantly affecting the antenna gain or bandwidth. In fact the antenna bandwidth slightly improved when the ground plane area of the antenna was reduced from $75 \times 75 \text{ mm}^2$ to $40 \times 40 \text{ mm}^2$. The peak boresight directivity and realized gain, shown in Fig. 4.4, are 18.7 dBi and 18.2 dBi, respectively, with the smaller ground plane. The 3dB gain bandwidth extends from 11 – 13.35 GHz, which is 21.7% at $f_0=11.1 \text{ GHz}$. Average radiation efficiency in the operating band is 88% as calculated using the realized antenna gain, directivity, mismatch loss and dielectric loss. In general, the measured gain curve closely follows the predicted one, shown in Fig. 4.4, with a slight shift in frequency that is due to fabrication tolerances and measurement uncertainties.

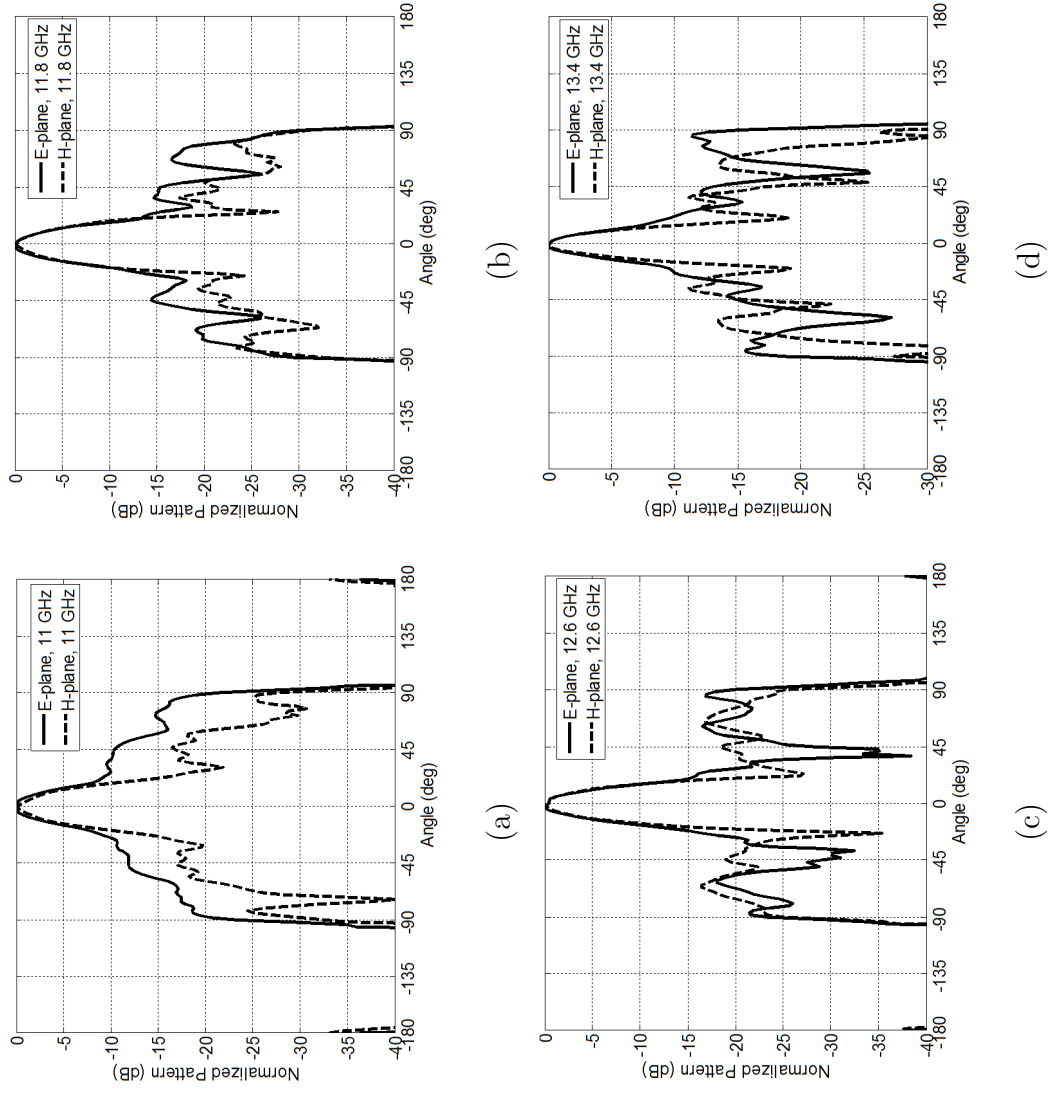


Figure 3.12: Measured radiation patterns of the proposed ERA at (a) $f = 11.0$ GHz (b) $f = 11.8$ GHz (c) $f = 12.6$ GHz (d) $f = 13.4$ GHz

3.5.3 Radiation Patterns

The measured E- and H-plane radiation patterns are shown in Fig. 3.12 at four different frequencies within the measured 3dB gain bandwidth of the ERA. The patterns are directive with low SLL values. The H-plane patterns are better with SLL in the order of -17 dB over most of the operating band. SLL of about -10 dB is observed in the E-plane at 11 GHz; however, at higher frequencies, it remains below -15 dB. A summary of measured parameters is given in Table 3.2. The overall performance of the antenna is found to be consistent with the predictions. This verifies the design methodology and demonstrates that defect-mode structures formed by unprinted dielectric slabs can be used to design wideband ERAs.

3.6 Conclusion

A novel wideband EBG resonator antenna (ERA) has been designed utilizing a wide defect-mode produced by unprinted dielectric slabs of different permittivity and thickness values, and by significantly truncating its superstructure area. It was found that, provided the reflection from the superstructure ($|\Gamma_{SRM}|$) is strong enough, the defect-mode bandwidth approximately predicts the 3dB directivity bandwidth of finite ERAs with medium superstructures ($\approx 9 - 16\lambda_0^2$). Thus when designing wideband ERAs, increasing the defect mode bandwidth using a unit cell is a reasonable start. However, the ERA directivity bandwidth can further be enhanced significantly by truncating these wideband superstructures to have smaller areas (e.g., $2.25 - 4\lambda_0^2$). Experimental results demonstrate 18.2 dBi peak gain and an excellent 3dB gain bandwidth of 21.7%, which is a significant increase over 3-4% bandwidth of classical 1-D ERAs having a single feed.

It is worth noting that this wideband performance is achieved by using a single feed and unprinted dielectric slabs, hence, avoiding the need for expensive feeding networks

and/or complex to design, printed superstrates. The antenna has a well matched feed over the operating bandwidth ($VSWR < 1.6$) and its area is only 15% of the conventional ERAs. In addition, owing to the symmetrical superstructure, these antennas can be extended to support dual-linear polarization as well as circular polarization over a wide band. To the best of our knowledge, no other planar antenna with an area as small as $2.25\lambda_0^2$ has a measured gain over 15 dBi with a measured bandwidth over 20%.

Chapter 4

Defect-Mode Superstructures for Wideband ERAs

4.1 Abstract

We propose two electromagnetic band gap (EBG) structures made out of multi-layer dielectric slabs to enhance the bandwidth of EBG resonator Antennas (ERAs). These multi-layer structures are designed to achieve wide defect-mode bandwidths. Wide defect-modes are created by optimizing the permittivity and thickness of the individual slabs, as well as the inter-slab separations. Using these EBG structures as ERA superstrates and truncating them appropriately to a finite size, two ERAs were designed. They exhibit pattern bandwidths nearly twice as wide as the classical ERAs. 3dB directivity bandwidths of 14.1% and 19.3% with a maximum directivity of 17.5 dBi

Published as: R.M. Hashmi, B.A. Zeb, and K.P. Esselle, "Composite defect-mode superstructures and wideband EBG resonator antennas," *9th European Conference on Antennas and Propagation (EuCAP)*, Lisbon, Portugal, 12-17 April, 2015.

and 18.7 dBi, respectively, were measured for the two ERA prototypes. The lateral dimensions of the ERA superstrates are $1.5 \times 1.5 \lambda_0^2$ which represent more than 90% reduction in superstrate area when compared with classical ERAs. Small size and simple configuration make these ERAs very suitable for high-gain millimeter wave applications.

4.2 Introduction

Electromagnetic band gap (EBG) resonator antennas (ERAs) are excellent candidates for upper microwave and millimeter wave applications. At these frequencies, their high gain, small size, and simple configuration present a major advantage over bulky and complex alternatives. An ERA generally consists of a linear, dual-linear or circularly polarized feed source, embedded within a resonant cavity [5, 8, 53]. This resonant cavity is formed by a partially-reflecting surface (PRS) and a metallic ground plane, which are separated by a distance h . With h adjusted to satisfy the Fabry-Perot resonance condition, highly directive emissions can be achieved with only a single feed source [35].

The design of PRS is a rich area of interest [5, 8, 12, 13, 50, 51]. PRSs can take various forms such as 1D stacks of alternating dielectrics [8], 2D Frequency Selective Surfaces (FSS) [12] or 3D periodic structures [53]. The nature of PRS has a major role in achieving high directivity and determining the pattern bandwidth of the resulting ERA [5, 12, 13, 51]. Pattern bandwidth is defined here as the range of frequencies where the directivity of the ERA remains within 3dB less than the maximum value. Improving the pattern bandwidth while maintaining high peak gain (>15 dBi) is a major challenge. This limitation restricts the use of ERAs for various applications which require directive beaming over a wide frequency band. Initial ERAs were quite narrowband with pattern bandwidths in the range of 3-5% [5]. Various PRS designs have been proposed to improve this figure up

to 12% including the use of resonant capacitive and inductive elements [12], multi-layer PRSs [50], and dielectric superstructures [13].

A major advance was made in [10] by using an array of slots instead of a single feed source in the cavity. This method improved the pattern bandwidth up to 13.2% alongside a peak gain of 22.7dBi, due to highly uniform PRS illumination. Recently, composite superstructures made out of dielectric layers have been introduced in [72]. These superstructures are designed to obtain wide defect-modes (localized transmission windows) within the band gap of an EBG structure. We propose two such superstructures which are designed to have wide defect-mode bandwidths. These structures are then used to design ERAs, which achieve wide pattern bandwidths with a high peak directivity. Unit-cell analyses of the proposed structures are carried out in CST Microwave Studio using normal incidence of plane waves and periodic boundary conditions. The ERAs were designed using FDTD-based transient solver and the prototypes were fabricated using in-house facilities. The measured results of the prototypes demonstrate up to 97% increase in the pattern bandwidth of ERAs.

The rest of the paper is organized as follows: Section II describes the classical structure of ERAs and the proposed wide defect-mode structures with their respective unit-cell models. Section III presents the finite antenna design and fabrication details. Section IV discusses on the measured directivity and impedance matching of the two antenna prototypes and Section V concludes the paper.

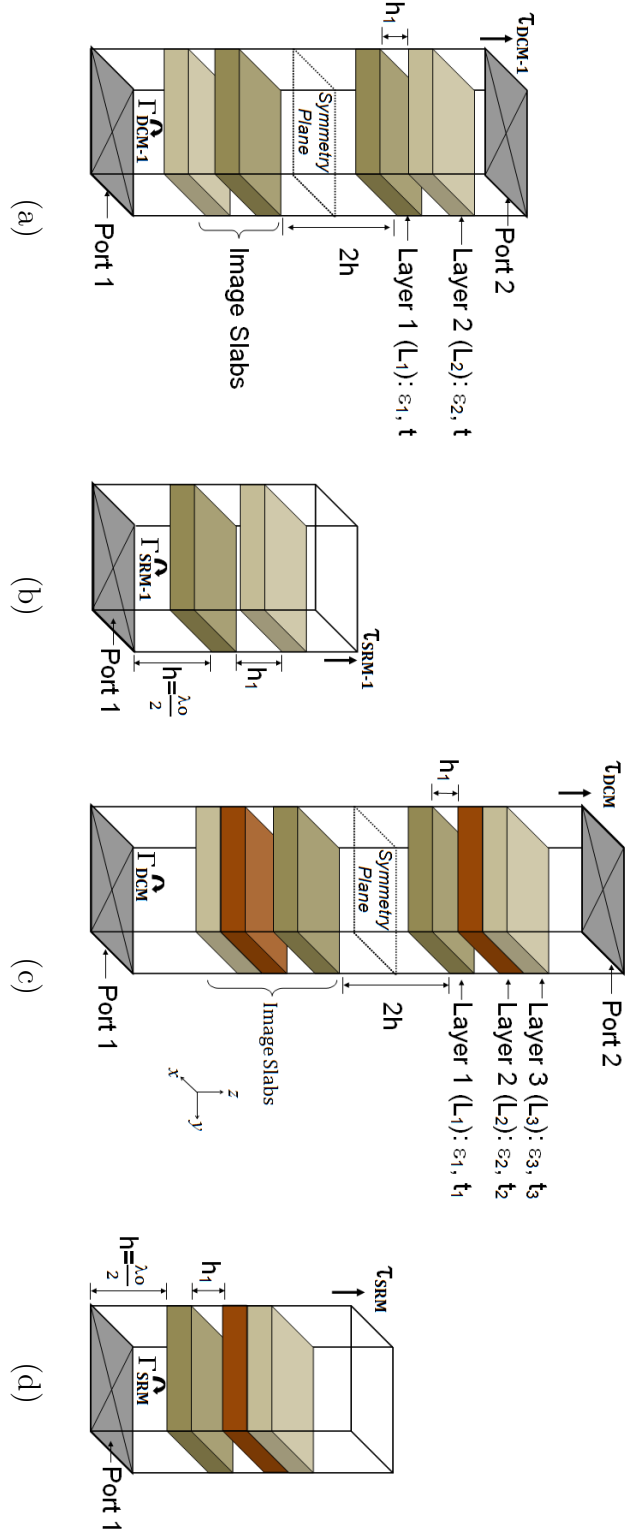


Figure 4.1: Defect cavity model (DCM) unit cell and Superstructure reflection model (SRM) unit cell of the two wide defect-mode EBG Structures: S-I and S-II (a) DCM of S-I, with image slabs (b) SRM of S-I (c) DCM of S-II, with image slabs (d) SRM of S-II.

4.3 Defect-Mode EBG Structures

4.3.1 Classical ERAs and Pattern Bandwidths

Classical all-dielectric ERAs consist of a stack of N layers (N is always even) above an infinite ground plane [39]. These layers alternate with a refractive index $n_1 = \sqrt{\epsilon_1 \mu_1}$ and thickness $h/2$ for all odd layers except the first odd layer. The first odd layer has a thickness h and forms the primary cavity where the excitation source is to be embedded. Often, the material for the odd layers is taken as free space or air ($\epsilon_1 = \epsilon_0, \mu_1 = \mu_0$). The even layers alternate with a refractive index $n_2 = \sqrt{\epsilon_2 \mu_2}$ and have the same thickness t for all layers. The thicknesses of even and odd layers are given by:

$$n_1 h \sqrt{1 - (\sin^2 \theta_0)/n_1^2} = \lambda_0/2 \quad (4.1)$$

$$n_2 t \sqrt{1 - (\sin^2 \theta_0)/n_2^2} = \lambda_0/4 \quad (4.2)$$

where $\theta_0 = 0$ for a broadside beam, which is the case in most ERAs. This method suggests that the superstrate layers should be quarter-wavelength thick and the primary cavity should be half-wavelength thick (where the wavelength is referenced to the respective refractive indices, n_1 and n_2). In addition, it has been established for classical ERAs that the maximum directivity increases as the permittivity of the superstrate layers increases, whereas the bandwidth decreases [84]. Nevertheless, in the following sections, we present an alternative arrangement of the superstructure layers which, when used in the ERA superstrate, allows to have high directivity as well as wide bandwidth. Also, another striking characteristic of this arrangement is that the maximum directivity does not change significantly with the variation of the lateral size of ERA, which is not the case in conventional all-dielectric ERAs [97]. This characteristic allows to have a compact ERA configuration with a small lateral size.

4.3.2 Unit-Cell Configuration

The EBG structures, S-I and S-II, have an important role in the design of the proposed wideband ERAs discussed in Section III. However, before we proceed to the antenna design, these structures are analyzed using a unit-cell approach. The unit-cell models shown in Fig. 4.1 have been thoroughly discussed and classified as the Superstrate Reflection Model (SRM) and Defect Cavity Model (DCM) in [81]. We use the SRM and DCM to achieve high-superstrate reflection magnitude and increasing reflection phase, as well as wide defect-mode bandwidth, respectively. These conditions are necessary to achieve directivity enhancement over a wide bandwidth. Once the unit-cell requirements are met, the superstructures are placed above a conducting ground plane at height h and are laterally truncated to a finite value. The SRMs shown in Fig. 4.1 (b) and (d) are formed by placing a port de-embedded to a distance h , away from the bottom surface of L_1 . This allows to compute the reflection profile ($|\Gamma_{SRM}|$ and $\angle\Gamma_{SRM}$) of S-I and S-II. On the other hand, the DCMs shown in Fig. 4.1 (a) and (c) are formed by applying image theory and mirroring the dielectric stack along the symmetry plane. The respective defect-mode bandwidths ($BW_{DCM}|_{\tau>0.7}$) can be computed using the DCM. The $BW_{DCM}|_{\tau>0.7}$ is the bandwidth where the transmission magnitude (τ_{DCM}) is greater than 0.7. The reflection and transmission coefficients are denoted by Γ and τ and are marked at their respective reference locations in Fig. 4.1. These coefficients can be calculated by numerical simulations using CST Microwave Studio. Periodic boundary conditions were applied to side walls and excitations were defined on the reference ports marked in Fig. 4.1.

4.3.3 Design of Defect-Mode Structures

We use the idea of inserting multiple defects with closely spaced resonant frequencies to achieve pass band filtering phenomenon [42]. This phenomenon results in the creation of

wide defect-mode EBG resonators. Local variation of permittivity is used to modify the effective thickness of the slabs and is treated as a defect to create two configurations of EBG structures:

1. *Superstructure-I (S-I)*: a two-slab structure with uniform thickness having a permittivity contrast
2. *Superstructure-II (S-II)*: a three-slab structure with permittivity contrast and a composite slab

The first EBG structure, S-I, consists of two layers (L_1, L_2) which have the uniform thickness $t = 3.2\text{mm}$ but unequal dielectric constants: $\epsilon_1 = 9.2$ and $\epsilon_2 = 9.8$. The variation of dielectric constant ($\Delta\epsilon$) modifies the effective thickness of the slabs and creates a defect in the band gap of S-I (the guided-wave thickness is dependent on guided wavelength ($\lambda_g = \lambda_0/\sqrt{\epsilon_r}$)). The bandwidth of this defect can be increased by tuning $\Delta\epsilon$ along with the separation between L_1 and L_2 designated as h_1 in Fig. 4.1 (a) and (b). A wide $BW_{DCM}|_{\tau>0.7}$, shown in Fig. 4.2, is obtained by selecting $\Delta\epsilon = 0.6$ and $h_1 = 10\text{mm}$. The narrowband defect obtained from the classical EBG structure ($\epsilon_1 = \epsilon_2 = 9.2, t_1 = \lambda_g/4, h_1 = \lambda_0/4$ and $h = \lambda_0/2$) is also plotted in Fig. 4.2 for the insight of the reader. The reflection phase of S-I was also calculated using the SRM in Fig. 4.1 (b) and was found to be linearly increasing within $BW_{DCM}|_{\tau>0.7}$, satisfying the requirement set forth in [5] for wideband directivity enhancement. However, it was found during the ERA design phase that the pattern bandwidth of the ERA formed by S-I is limited by the undesired resonance of the secondary cavity formed between L_1 and L_2 .

To resolve this limitation of pattern bandwidth, S-II, on the other hand, is formed by three layers: L_1, L_2 and L_3 . The thicknesses of these layers are $t_1 = 3.2\text{mm}, t_2 = 1.3\text{mm}$ and $t_3 = 3.2\text{mm}$ whereas their dielectric constants are $\epsilon_1 = 3.27, \epsilon_2 = 10.5$ and $\epsilon_3 = 4.5$. The separation between L_1 and L_2 , designated as h_1 in Fig. 4.1 (c) and (d), is set to

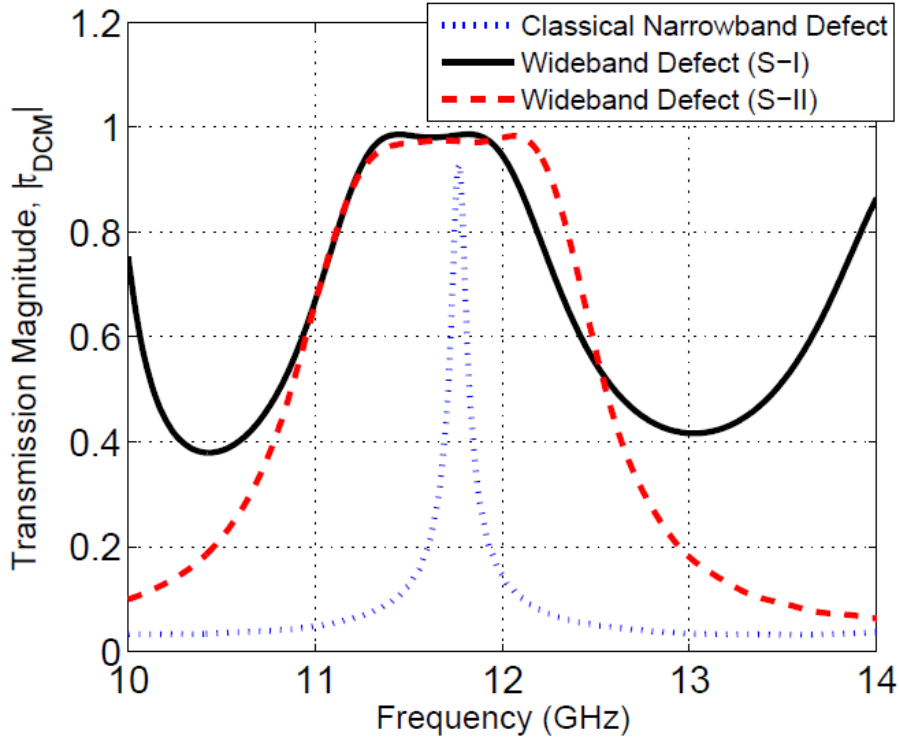


Figure 4.2: *Transmission through the defect cavity model for both superstructure types.*

6.5mm where as L_2 and L_3 are joined together to form a composite slab. In addition to the approach used in S-I, the high-permittivity layer L_2 acts as an inclusion in S-II which not only rectifies the undesired resonance present in S-I, but also allows S-II to have 12% reduced height than S-I. The $BW_{DCM}|_{\tau>0.7}$ of S-II is shown in Fig. 4.2 which is found to be slightly wider than S-I over the band of interest. It was found that the reflection phase of S-II tends to decrease in a monotonic manner, however, its descent is very slow within $BW_{DCM}|_{\tau>0.7}$.

4.4 Antenna Design and Fabrication

It was found that the $BW_{DCM}|_{\tau>0.7}$ (obtained from the DCM of an infinite structure as discussed in Section II) approximately predicts the 3dB directivity bandwidth of a

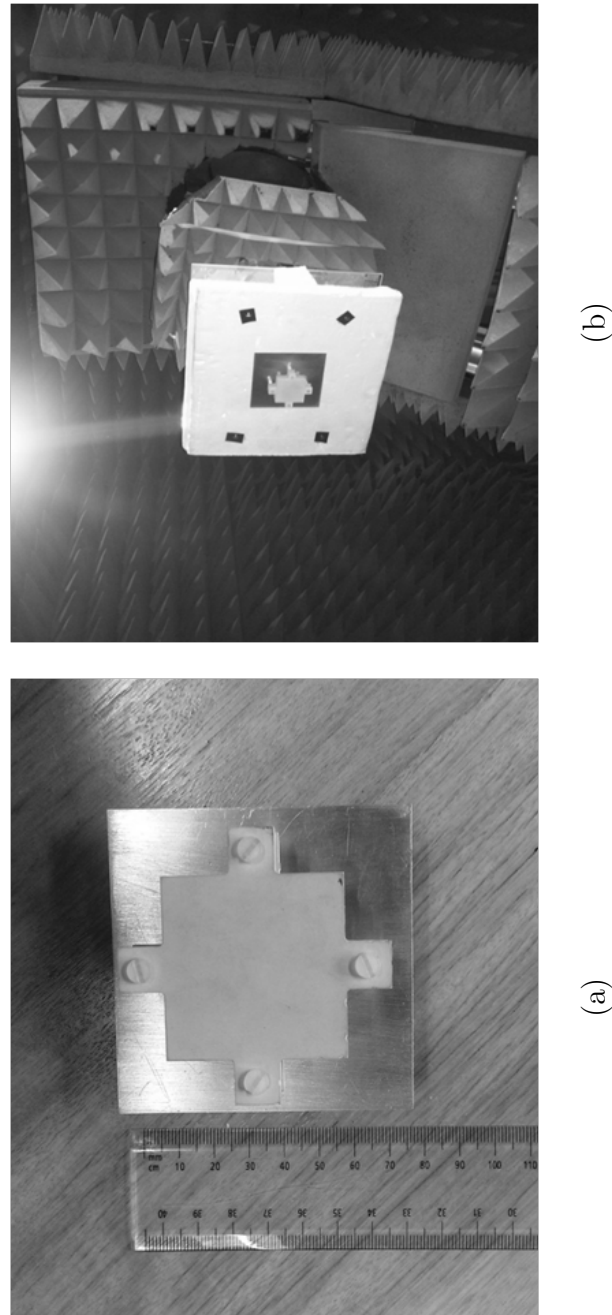


Figure 4.3: Prototypes of the ERAs designed with S-I and S-II. Both ERAs are fed using a waveguide-to-coax adaptor: top view of ERA_{S-I} with superstructure consisting of two dielectric layers (left) and ERA_{S-II} with superstructure consisting of three dielectric layers, during measurement at the AusAMF.

Table 4.1: *Summary of measured performance of the wideband ERAs.*

Frequency (GHz)	E-Plane Sidelobe Level (dB) <i>ERAs-I</i>	H-Plane Sidelobe Level (dB) <i>ERAs-I</i>	Radiation Efficiency (%) <i>ERAs-I</i>
11.0	-8.5	-16.0	92.4
11.8	-18.0	-16.0	88.3
12.6	-14.5	-18.0	83.4
13.4	-17.5	-14.8	95.0

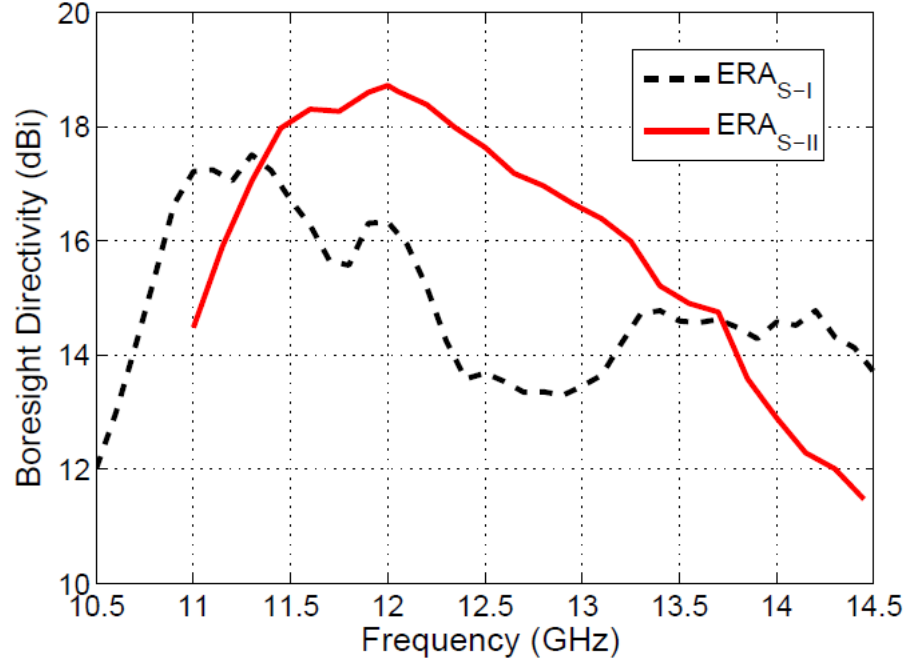


Figure 4.4: Measured broadside directivity of the two ERA prototypes.

finite antenna for medium-sized superstructures ($\approx 9 - 16\lambda_0^2$). For instance, the DMB of S-II was 12% and the corresponding antenna bandwidth with $4 \times 4\lambda_0^2$ superstructure was found to be 11%. However, this bandwidth can be further increased significantly by reducing the area of the superstructure. Hence, for both antennas, parametric studies were conducted to select the superstructure area that minimizes the antenna size while providing high-gain and a wide patten bandwidth.

The two structures S-I and S-II were applied as superstrates to design ERAs and their performance was measured. The first ERA (ERA_{S-I}) having S-I superstructure was fabricated using Rogers TMM 10 ($\epsilon_1 = 9.2, t_1 = 3.175$ mm) and Rogers TMM 10i ($\epsilon_2 = 9.8, t_2 = 3.175$ mm). The second ERA having with S-II was fabricated with Rogers TMM 3 ($\epsilon_1 = 3.27, t_1 = 3.175$ mm), RT/Duroid 6010.5 ($\epsilon_2 = 10.5, t_2 = 1.27$ mm) and Rogers TMM 4 ($\epsilon_3 = 4.5, t_3 = 3.175$ mm). The loss tangent of the materials used is $\tan\delta = 0.002$. Both S-I and S-II were laterally truncated to a small area of 40×40

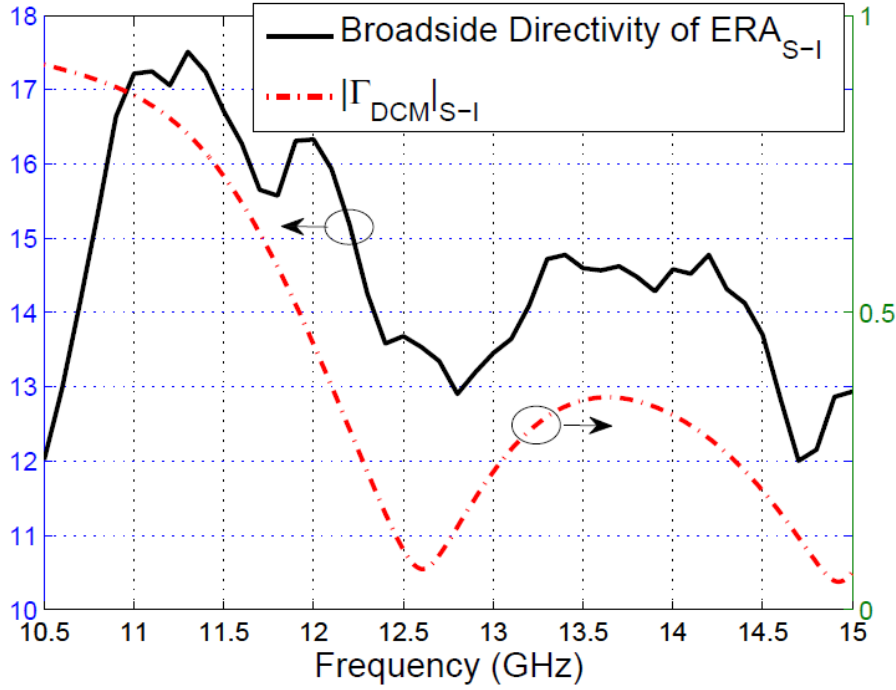


Figure 4.5: Broadside directivity of ERA_{S-I} is compared with the reflection coefficient magnitude of the DCM to show the self-resonance within the EBG structure and its effect in reducing the pattern bandwidth.

mm^2 ($2.25\lambda_0^2$). Four small extensions were provided to place nylon spacers for holding the superstructure in place. An aluminium ground plane is used in both the prototype ERAs. The parameters h and h_1 (see Fig. 4.1) were set to 13.5 mm and 6.43 mm, respectively. Fig. 6.1 shows the prototypes of ERA_{S-I} and ERA_{S-II} , the nylon spacers can be seen on the edges of the superstructure.

4.5 Results and Discussion

The directivity and gain for ERA_{S-I} and ERA_{S-II} were measured in the NSI-700S-50 spherical near-field measurement system at Australian Antenna Measurement Facility (AusAMF). The gain was computed using the gain comparison method using a WR-

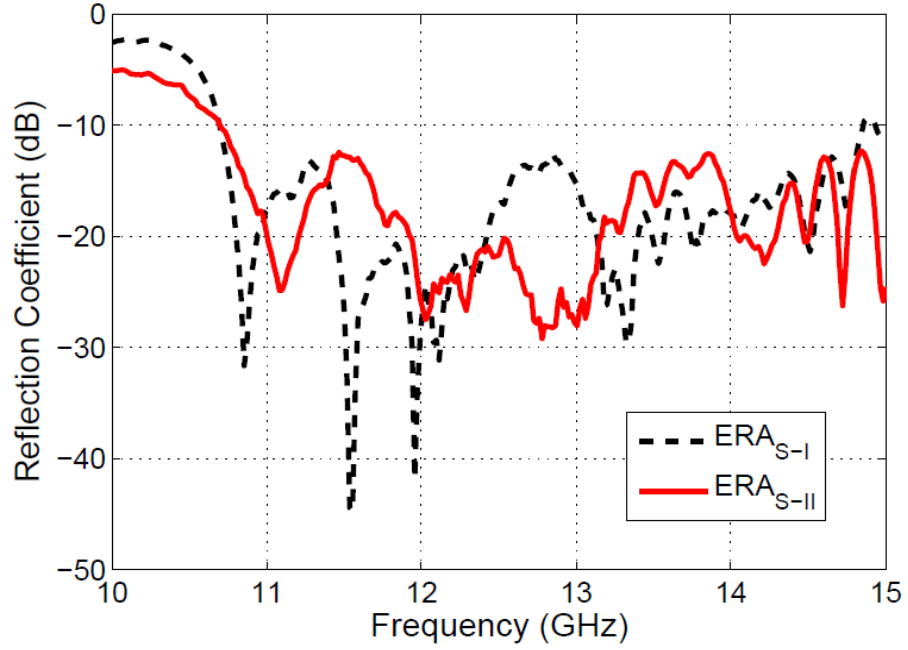


Figure 4.6: Measured input reflection coefficient for both antenna prototypes demonstrating wideband impedance matching covering the entire pattern bandwidths.

75 standard gain horn. For ERA_{S-I} , the measured broadside directivity is shown in Fig. 4.4 with a maximum value of 17.5 dBi at 11.35 GHz. It can be seen that the pattern bandwidth extends from 10.72 GHz to 12.35 GHz, i.e., 14.1%. The maximum directivity for ERA_{S-II} was measured to be 18.7 dBi at 12 GHz alongside a 3-dB gain bandwidth which extends from 11.0 GHz to 13.35 GHz. This is equivalent to a pattern bandwidth of 19.3%.

The input reflection coefficient ($|S_{11}|$) for both the prototypes was measured using the HP8720D Vector Network Analyser and is shown in Fig. 4.6. A rectangular waveguide with a standard 50Ω waveguide-to-coax adapter is used to feed the cavity through a slot. The dimensions of the slot are $7.5 \times 12.5 \text{ mm}^2$. The input impedance bandwidth for ERA_{S-I} extends from 10.0 GHz to 14.7 GHz (i.e. 40.8%) and that of ERA_{S-II} extends from 10.7 GHz to 15 GHz (i.e. 37.4%). The measured results of the two antennas were found to agree well with the results predicted by the FDTD-based transient solver.

ERA_{S-I} has 44% more pattern bandwidth than a classical ERA with the same superstructure size. This improvement increases even more with ERA_{S-II} which has 97% increased pattern bandwidth. Despite the wide $BW_{DCM}|_{\tau>0.7}$, the pattern bandwidth of ERA_{S-I} is lesser than ERA_{S-II} . This is because the secondary cavity in S-I (formed between L_1 and L_2) begins to resonate near $f = 12.5$ GHz. Fig. 4.5 shows the Γ_{DCM} for S-I calculated from the DCM in Fig. 4.1 (a) which shows that the superstructure becomes nearly transparent near 12 GHz as $|\Gamma_{DCM}|$ approaches close to 0. The impedance bandwidths overlap with the respective pattern bandwidths very well. This overlap is necessary for the ERAs to provide high gain within the pattern bandwidth, otherwise the mismatch losses can reduce the antenna gain. A summary of measured parameters is presented in Table. 4.1 comparing ERA_{S-I} and ERA_{S-II} at selected frequencies within the pattern bandwidth.

The measured radiation patterns of ERA_{S-I} shown in Fig. 4.7 were found to be directive with low side lobes over most of the pattern bandwidth. For ERA_{S-II} (patterns not shown for brevity), sidelobe level as high as -10 dB was observed in E-plane, initially near 11 GHz, which, afterwards, decreased below -15 dB. Following the common characteristic of ERAs with all-dielectric superstructures, the sidelobe levels in both the ERAs began to increase near the upper limit of the pattern bandwidth. However, the beam quality was found to be good with an average side lobe level of -15 dB within the pattern bandwidth. The cross-polarization levels were also measured and found to be amply lower, with an average value of -24 dB within the 3dB beamwidth.

4.6 Conclusion

Wideband electromagnetic band gap (EBG) resonator antennas (ERAs) with defect-mode superstrates have been proposed and successfully tested. The measured results of the pro-

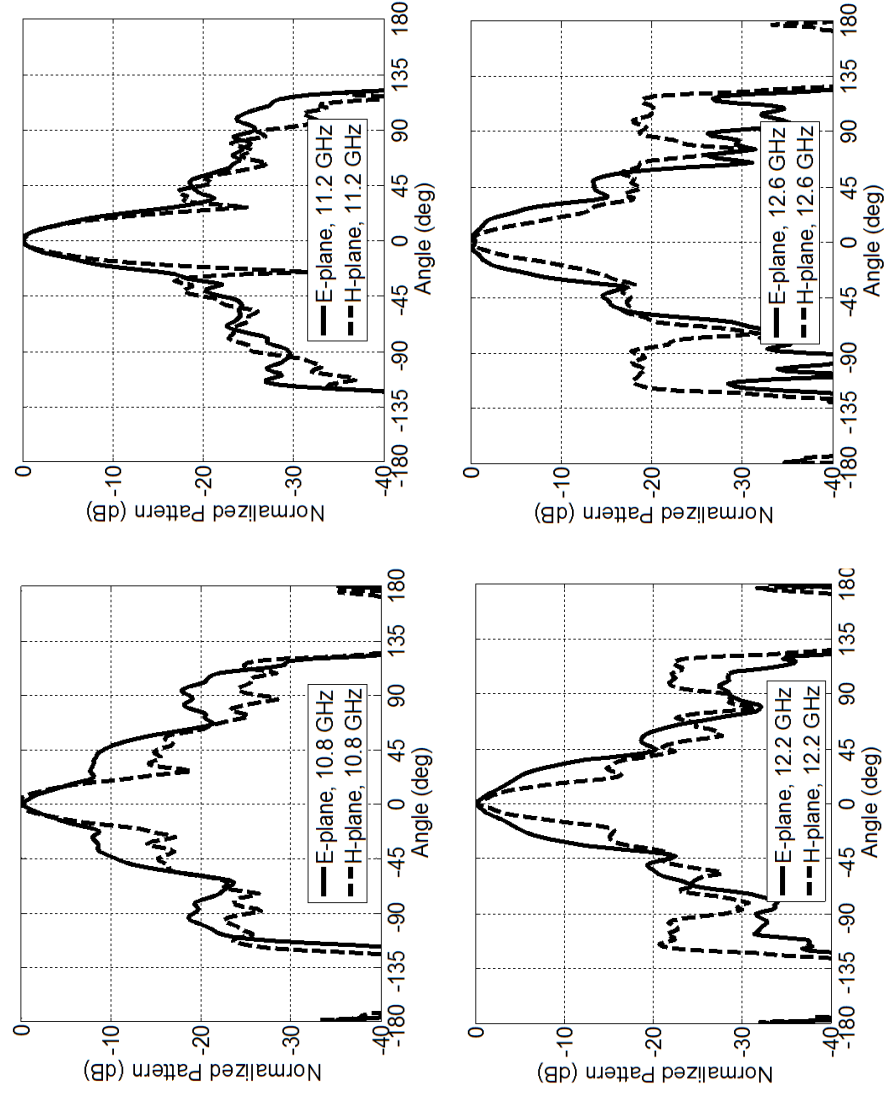


Figure 4.7: Measured radiation patterns of the proposed ERA_{S-I}

totypes demonstrate wide pattern bandwidths, high directivity and excellent impedance matching over the entire operating bandwidth. It is shown using defect-cavity analysis how self-resonances within a superstructure limit the pattern bandwidth of an ERA and an alternative approach is presented to overcome this limitation. In addition to the wide defect-mode bandwidths, small size of the finite antenna superstrate was found to significantly improve the pattern bandwidth of ERAs. It is interesting to note that though the profile of these ERAs is comparable to classical two layer designs, their overall volume is much smaller, making them highly compact.

Chapter 5

Wideband ERAs with Dielectric Superstructures having Transverse Permittivity Gradients

5.1 Abstract

Extremely wideband electromagnetic band gap (EBG) resonator antennas (ERAs) with large directivity-bandwidth products are presented. Their distinct feature is a single-slab superstrate that has a dielectric constant gradient in the directions transverse to the antenna axis. In practice, this is implemented by combining dielectric segments to form a planar slab with a transverse permittivity gradient (TPG). The application of such a superstrate in a single-feed ERA improves the directivity-bandwidth product by a factor of three or more

Published as: R.M. Hashmi and K.P. Esselle, "A class of extremely wideband resonant cavity antennas with large directivity-bandwidth products," *IEEE Transactions on Antennas and Propagation*, December 2015 (*in press*).

as compared with superstrates composed of uniform dielectric slabs. Prototype ERAs have been fabricated and measurements have validated the concept. A measured 3dB directivity bandwidth of 52.9% was demonstrated with a measured directivity of 16.4 dBi for an ERA that has a very small total footprint area of $1.54\lambda_0^2$. This represents an increase of 90% over the previous best measured ERA directivity bandwidth of 28%. Its measured directivity-bandwidth product of 2,309 represents 41% increase over the previous best measured directivity-bandwidth product of 1,637.

5.2 Introduction

Electromagnetic band gap (EBG) resonator antennas (ERAs)¹ with all-dielectric superstructures have been widely investigated in the past. These investigations have been fueled by their highly directive nature and simple configurations [5, 37, 52, 104]. In literature, ERAs are also known as Fabry-Perot cavity antennas, resonant cavity antennas, and 2-D leaky-wave antennas [36, 40, 92]. Antennas of this type find numerous applications in modern communication systems including point-to-point wireless links, sensor systems, and electronic warfare. A common ERA consists of a partially reflecting superstructure placed above a fully reflecting surface, forming a Fabry-Perot type cavity between them. This cavity is excited by one or several small antennas such as slots. The superstructures are often formed by a 1-D periodic arrangement of dielectric slabs [4, 8, 37], one or several 2-D printed superstrates [65, 104], or 3-D EBG structures [7].

Initial ERAs were extremely narrowband with bandwidths in the range of 1-3% [4,

¹The antennas proposed in this manuscript have been re-named as EBG resonator antennas (ERAs) so that the work remains consistent with the existing literature on this subject, as well as with the work presented in this dissertation. However, the name “resonant cavity antenna” (RCA) is more applicable here and was used in the original manuscript.

7, 8]. In the last decade, several ERAs have been proposed to address their narrow bandwidth [9, 11, 106, 107], as well as other aspects such as aperture efficiency [15, 97], compactness [54, 98], frequency-reconfiguration [58, 64], and height-reduction [108, 109]. The first advance in bandwidth enhancement of ERAs was demonstrated by using a two-layer metallo-dielectric superstructure, reaching a record bandwidth of 10% in 2006 [9]. A 2-D grid of metallic patches printed on each of the layers was optimised to create two closely spaced resonant bands, which combined to form a single wide band. In 2007, a multi-layer dielectric EBG superstructure excited by an array of aperture-coupled slots demonstrated a further increase in the measured bandwidth up to 13% [10, 89]. Since then, various approaches have been developed to increase the measured bandwidth of ERAs that include the use of graded-index metamaterial superstrates [11, 80] and superstrates with capacitive and inductive grids [14, 76]. Realization of a positive reflection phase gradient over a wide bandwidth from a thin printed superstrate led to an ERA prototype with 15.7% directivity bandwidth in 2012 [12]. Recently, multi-layer defect-mode composite EBG superstructures have been designed to produce ERAs with measured bandwidths as large as 22% [72]. The largest measured bandwidth ever recorded for an ERA is 28% with a peak gain of 13.8 dBi [14]. For ERAs with gains greater than 15 dBi, the largest measured bandwidth recorded is 27.7% [15].

It is well known that an increase in ERA bandwidth is often accompanied by a decrease in its directivity. Hence, the directivity-bandwidth product (DBP) is also a very important figure of merit. To the best of our knowledge, only three wideband ERA prototypes have demonstrated DBPs greater than 1,000. They are: an ERA in [72] with a three-layer defect-mode superstructure (DBP=1,453), the ERA in [76] with three printed PRS layers (DBP=1,500), and the dual-resonator ERA in [10] with a slot array feed (DBP=1,637).

In this paper, we present a new class of extremely wideband ERAs having planar, single-layer superstrates. These superstrates are made out of unprinted dielectric mate-

rials and have non-uniform permittivity in the transverse direction, forming a transverse permittivity gradient (TPG). This paper describes how to increase ERA directivity bandwidth drastically by means of ‘superstrates with TPG’ (STPG), compared to superstrates with uniform permittivity. We demonstrate that directivity bandwidths greater than 50% and DBPs greater than 2,000 can be achieved from ERAs using this method. For ERAs with STPG, classical design approaches involving unit-cell optimizations or transmission line modelling are not suitable, as they assume uniform transverse extension to infinity. To overcome this limitation, rigorous full-wave analyses were conducted, followed by experiments to characterise the performance of ERAs with STPGs. This work thoroughly explores the mechanism of broadband directivity enhancement by relating it to the electric field phase distribution above the superstrate and within the Fabry-Perot cavity, thus, providing valuable physical insight.

Two ERA prototypes have been fabricated through subtractive manufacturing. The realised superstrates are made out of commercially available dielectric materials that approximate a continuous TPG with three quantized uniform dielectric segments. Experimental results demonstrate a directivity bandwidth of 52.9% and a peak directivity of 16.4 dBi. To the best of our knowledge, this is the largest bandwidth ever demonstrated by an ERA. Its measured DBP (2,309) is also the highest for any ERA, exceeding the previous best (1,637) by 41% [10]. Computed results predict that it can be increased well beyond 3,000 by using thicker STPGs.

The all-dielectric, symmetric nature of the superstrate is attractive as it adds polarisation flexibility to the antenna; i.e. these linearly polarised (LP) ERAs can be extended to dual-linear (DP) or circularly polarised (CP) configurations by replacing the LP feed antenna with an appropriate DP or CP feed antenna. In addition, the need of only a single dielectric superstrate reduces the height of the ERA, adding overall compactness, when compared with multi-layer ERAs. We presented our preliminary work on the concept of

ERAs with this type of superstrate in [70, 71]. However, these conference publications only contain very limited computed results for a special ideal case with five segments.

5.3 STPG Configuration and Advantage

This section first describes the configuration of STPG and ERA. It is followed by discussion on STPG characteristics and the advantages offered by them in terms of ERA directivity and bandwidth.

5.3.1 STPG and ERA Configurations

An example STPG is shown in Fig. 5.1 (a). It has a circular shape with radius R and thickness t , but other shapes such as rectangular or elliptic are equally possible. Ideally, the permittivity of the STPG should decrease continuously and radially from a high value ($\epsilon_1 = \epsilon_{high}$) in the centre to a low value ($\epsilon_N \approx 1$) at the edges. However, for practical implementation, such a continuous gradient can be approximated by segmenting the superstrate disc into one small circle in the middle (radius of w_1) surrounded by concentric rings where each ring has a width of w_i and relative permittivity of ϵ_i ($i \in \{2, \dots, N\}$), where N is the number of quantization segments. It should be noted in Fig. 5.1 (a) that the widths w_i may or may not be equal. A linear, quantized TPG can be obtained when all segments have equal widths (i.e. $w_i = R/N$), and the permittivity of each segment is given by $\epsilon_i = i \times \epsilon_{high}/N$. In all the cases to follow the value of ϵ_1 is 10 unless it is stated otherwise.

In order to form the ERA shown in Fig. 5.1 (b), the superstrate in Fig. 5.1 (a) is placed at a height h above the ground plane. Initial value of h is approximately $\lambda_{low}/2$ where λ_{low} is the wavelength at lower limit of the desired operating bandwidth. This results in an air-filled resonant cavity formed between the ground plane and the STPG. The area of

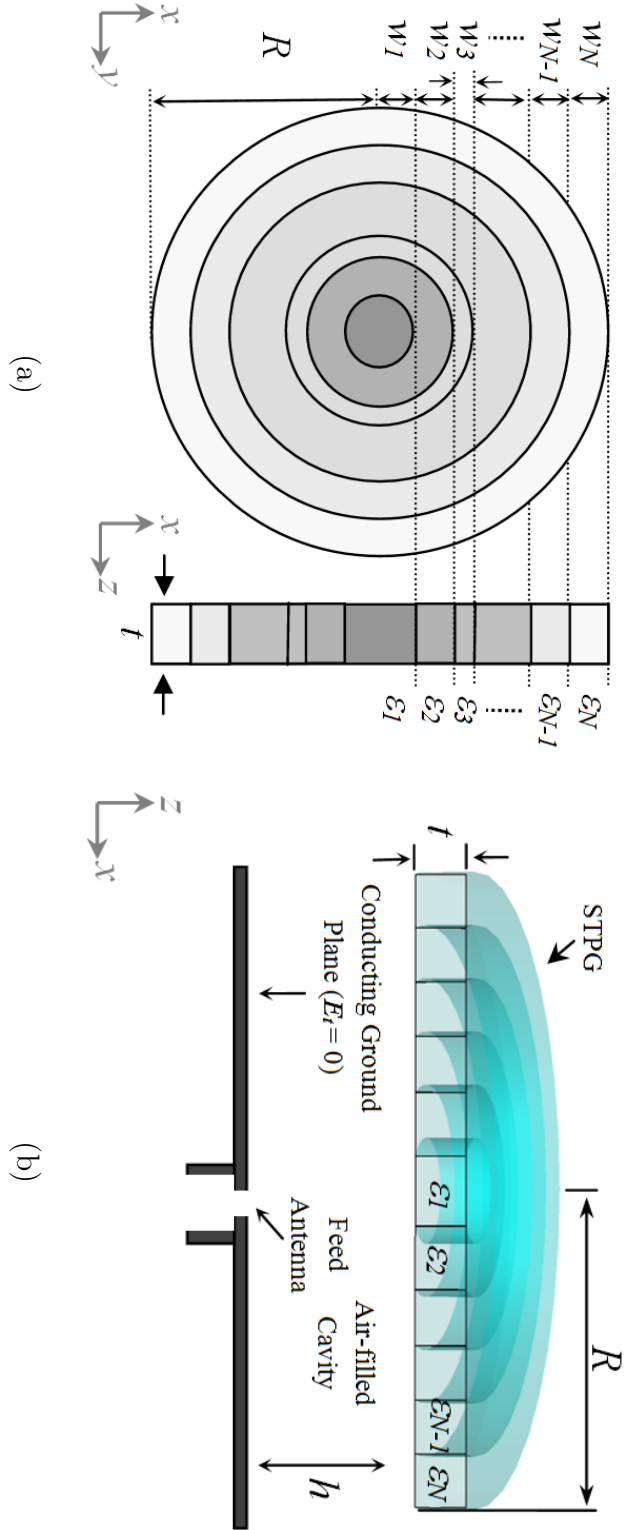


Figure 5.1: (a) Example configuration of a STPG with top view (i.e. xy-plane) and cross-sectional view (i.e. xz-plane) (b) Example configuration of an ERA with a STPG. Design parameters such as permittivity values ($\epsilon_1 \dots \epsilon_n$), segment widths ($w_1 \dots w_n$), STPG radius R , and slab thickness t are also shown.

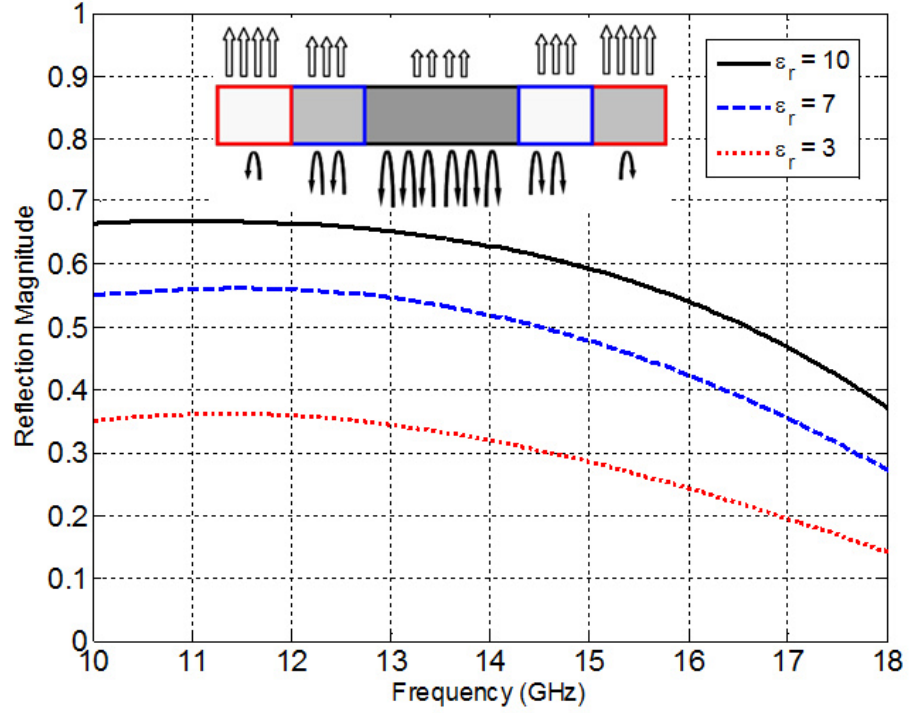


Figure 5.2: Reflection magnitudes of three uniform dielectric slabs. In the insert, transverse reflection and transmission profiles are shown symbolically for the case when these three materials are combined to form a STPG.

the ground plane can be equal or greater than that of the STPG. The cavity is excited by a small feed antenna that is placed in the centre of the ground plane (e.g. waveguide-fed slot shown in Fig. 5.1 (b)).

5.3.2 Transverse Reflectivity Variation

The reflection from, and the transmission through, a dielectric material depend on its relative permittivity and its thickness. The reflection magnitudes computed using the unit-cell SRM [72] for three different uniform dielectric slabs, having relative permittivity values of 10, 7, and 4, are shown in Fig. 5.2. In each case, the slabs are quarter-guided wavelength thick at 11.1 GHz ($t = \lambda_0 / 4\sqrt{\epsilon_r}$, where $\lambda_0 = 27mm$) and are assumed to be

infinite in transverse directions. It can be noticed that the reflection magnitude increases with the increase in the relative permittivity of the material. Therefore, when these materials are combined to form a superstrate which has a continuous or quantized TPG, the reflectivity varies over the surface of the superstrate. A superstrate with spatially varying reflectivity is shown in Fig. 5.2 insert for illustration. This superstrate is formed by selecting $N = 3$ and assigning following relative permittivity values: $\epsilon_1 = 10$, $\epsilon_2 = 7$, and $\epsilon_3 = 3$. The spatial transmission and reflection profiles are indicated by symbolic arrows placed above and below the superstrate, respectively. In the centre of the antenna where the cavity field is strong, transmission through the STPG is low and reflection is high. Closer to the edges of the antenna where the cavity field is weak, transmission through the STPG is high and reflection is low.

In practise, the highest relative permittivity of STPG ($\epsilon_{high} = \epsilon_1$) is determined by availability and cost of dielectric materials. However, its value should be reasonably high ($\approx 10 - 12$) to ensure sufficiently high reflectivity in the centre of the STPG. It was found that the proportion of ϵ_{high} area in the superstrate plays a vital role when fine-tuning the directivity bandwidth of the antenna. On the other hand, the lowest relative permittivity (ϵ_N) is desired to be very close to unity, to reduce lateral reflections from the edges of the cavity, back towards the feed. However, obtaining materials with such low permittivity is challenging and we found that ϵ_N values in the range of 2-3.5, which are commercially available, can provide good performance in terms of directivity bandwidth.

5.3.3 STPG vs. Uniform Superstrates

Broadside directivity of an ERA with a quantized STPG ($N = 9$) is shown in Fig. 5.3 along with that of three uniform superstrates, each made out of the same dielectric material. The thickness (t) of STPG is $\lambda_0/2\sqrt{\epsilon_1}$ or 4.3 mm. For the uniform superstrates, it is set to 4.3 mm, 5.1 mm, and 6.75 mm, according to $\lambda_0/2\sqrt{\epsilon_r}$ where $\epsilon_r = 10$, 7, and 4, respectively.

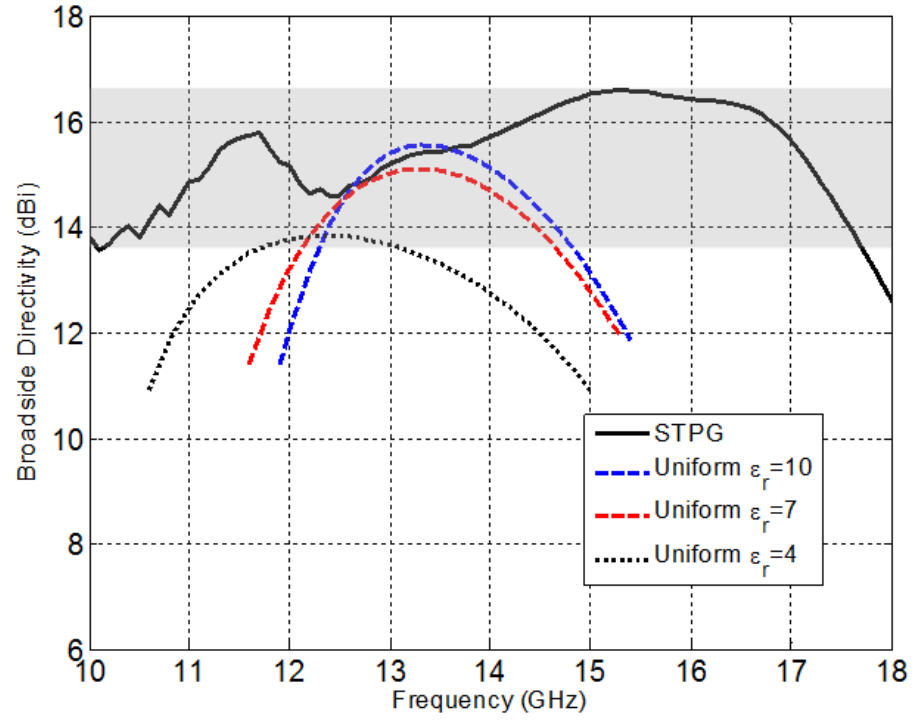


Figure 5.3: Broadside directivity of an ERA with a finely-quantized STPG ($N = 9$) is compared with the broadside directivity of three ERAs with uniform superstrates made out of different materials. The relative permittivity values of STPG are $\{\epsilon_1, \epsilon_2, \dots, \epsilon_9\} = \{10, 9, \dots, 2\}$; segment widths are $w_1 = 4\text{mm}$, $w_2, \dots, w_9 = 2.875\text{mm}$. the 3dB directivity band for the STPG case is shaded.

It is evident from Fig. 5.3 that the STPG outperforms all uniform superstrates in terms of both peak directivity and 3dB directivity bandwidth. In particular, the increase in bandwidth is tremendous. In terms of antenna height, the ERA with STPG is one of the two shortest ERAs in this group.

A classical relationship is found to prevail for each of the uniform superstrates where directivity increases with the increase in superstrate permittivity, whereas the bandwidth decreases. Instead, for the STPG, a higher peak directivity of 16.6 dBi together with a much larger 3dB directivity bandwidth of 54.7% is noted.

5.4 Superstrate Design

It is essential to address the tradeoff between manufacturing complexity and ERA performance. Thus, in this section, we evaluate the performance of finely-quantized STPGs versus practically desirable coarsely-quantized STPGs. Moreover, the effect of superstrate thickness on directivity-bandwidth product is also quantified.

5.4.1 Effect of Quantization

Since the quantization level (N) is a crucial factor in fabrication, let us study the effect of quantization coarseness on antenna performance by changing N . Apart from N , all other parameters such as R , t , and h are kept constant. A summary of key performance figures is given in Table 5.1. It is shown that when $N = 9$ (i.e. very fine quantization), the bandwidth reaches 58%. As the value of N is decreased, the bandwidth gradually decreases and reaches 46% for a reasonably coarse STPG with $N = 3$.

Table 5.1 also shows the relationship between the peak broadside directivity and the 3dB directivity bandwidth of several single-slab ERAs. With classical uniform superstructures (i.e. $N = 1$), a significant increase in bandwidth is often accompanied with

Table 5.1: *Effect of STPG quantization level on antenna performance.*

Quantization level (N)	Relative Permittivity for Segments $\{\epsilon_1, \epsilon_2, \dots, \epsilon_n\}$	Peak Broadside Directivity (dB_i)	3dB Directivity Bandwidth (%)	Directivity-Bandwidth Product
9	$\{10, 9, 8, \dots, 4, 3, 2\}$	16.3	58.0	2,474
5	$\{10, 8, 6, 4, 2\}$	16.2	56.0	2,334
3	$\{10, 7, 4\}$	16.7	46.0	2,151
1	$\{10\}$	15.5	22.8	809
1	$\{7\}$	15.0	26.0	822
1	$\{4\}$	13.8	34.6	830

ERA parameters are: $R = \lambda_0$, $t = 0.5\lambda_0/\sqrt{\epsilon_1}$, $h = 0.5\lambda_0$, $\lambda_0 = 27mm$, $w_i = R/N$.

a significant decrease in peak directivity. However, for the STPGs, when N is increased from 3 to 9, the change in directivity is negligible but the increase in bandwidth is significant, from 46% to 58%. When compared with uniform superstrates, the STPG with $N = 3$ leads to a drastically increased bandwidth and a higher directivity at the same time. It is evident that the directivity-bandwidth product improves by a factor of more than 3 when $N = 9$, and more than 2.5 when $N = 3$, compared to uniform superstrates. Based on the results in Table 5.1, $N = 3$ was found to be a logical compromise between wide bandwidth and complexity of fabrication.

5.4.2 Superstrate Thickness

For a superstrate with a given radius and gradient profile, it is possible to control the directivity-bandwidth product of the ERA by varying the superstrate thickness ' t '. Table 5.2 shows the performance figures for STPGs with four different thickness values. By increasing the thickness of the superstructure beyond the classical quarter guided-wavelength value, peak directivity can be increased by nearly 3 dB. In fact, the directivity-bandwidth product can be quadrupled by using thicker STPGs. This trend is particularly interesting for millimeter wave applications where such an increase in thickness is not impractical, considering the high directivity offered by these single-feed ERAs.

5.5 Phase Distribution and Directivity Bandwidth

Non-uniformity of phase in the aperture field is one reason for the limited directivity bandwidth of some ERAs. Therefore, let us now explore the phase distribution of the dominant transverse electric field on a fictitious "aperture" surface. This surface is parallel to the superstrate and is located at a height of $\lambda_0/8$ above the superstrate. Fig. 5.4(a) shows the aperture phase distribution with an example STPG whereas Fig. 5.5 (a) show the phase

Table 5.2: *Effect of varying superstrate thickness “ t ” on directivity-bandwidth product of an ERA with STPG.*

t (mm)	Peak Boresight Directivity (dB_i)	3-dB Directivity- Bandwidth (%)	Directivity- Bandwidth Product
$0.25\lambda_0/\sqrt{10}$	16.3	20.0%	853
$0.50\lambda_0/\sqrt{10}$	16.6	54.7%	2,500
$0.75\lambda_0/\sqrt{10}$	18.1	53.0%	3,421
$1.00\lambda_0/\sqrt{10}$	19.1	48.9%	3,975

ERA parameters are: $N = 9, \{\epsilon_1, \epsilon_2, \dots, \epsilon_9\} = \{10, 9, \dots, 2\}$, $w_1 = 4mm, \{w_2, \dots, w_9\} = 2.875mm, R = \lambda_0, h = 0.5\lambda_0$,
 $\lambda_0 = 27mm$.

distribution with a uniform superstrate, at four frequencies. Both the superstrates have equal radii (R) of 27 mm and therefore, the phase is plotted over a radial distance of ± 27 mm. All phase values have been normalized so that the peak of each curve is 0° , because the focus of our attention is their distribution as opposed to their absolute values.

It is evident that the spatial phase distribution above the STPG is significantly more uniform than the distribution above the uniform superstrate over the wide frequency range considered. The phase variation along the diameter of the STPG remains between 0° to 90° for most of the frequencies except near the upper limit of the directivity bandwidth (see Fig. 5.4(a)). On the contrary, in the case of the uniform superstrate, this difference exceeds even 180° along the diameter (see Fig. 5.5(a)). It is interesting to note that the phase distributions within the cavity for the two cases, shown in Fig. 5.4(b) and Fig. 5.5(b), are almost equally non-uniform. At each frequency, this in-cavity phase fluctuates in the central region due to feed antenna effects. Then the phase gradually decreases with increasing distance due to lateral propagation effects within the cavity. As opposed to a pure in-phase standing wave in an ideal resonant cavity, the field in an ERA cavity has wave components that propagate in transverse directions and they produce phase variations in the cavity. Despite similar in-cavity phase distributions, STPGs produce significantly more uniform aperture field distributions because the transmission phase delay through the superstrate is non-uniform. Less transmission phase delay through the outer segments in the STPG (discussed in Section II-B), which have low permittivity, partially compensates for the phase lag in the cavity field.

The importance of the uniformity of the aperture phase distribution can be understood using the Huygens-Fresnel principle. Let us consider the secondary wavefronts radiated from two points in the aperture plane that behave as secondary sources. Let us assume that the field strengths are equal (say α) at the two points. Suppose the phase difference between them is $\Delta\phi$. Each secondary source alone creates a power density that is propor-

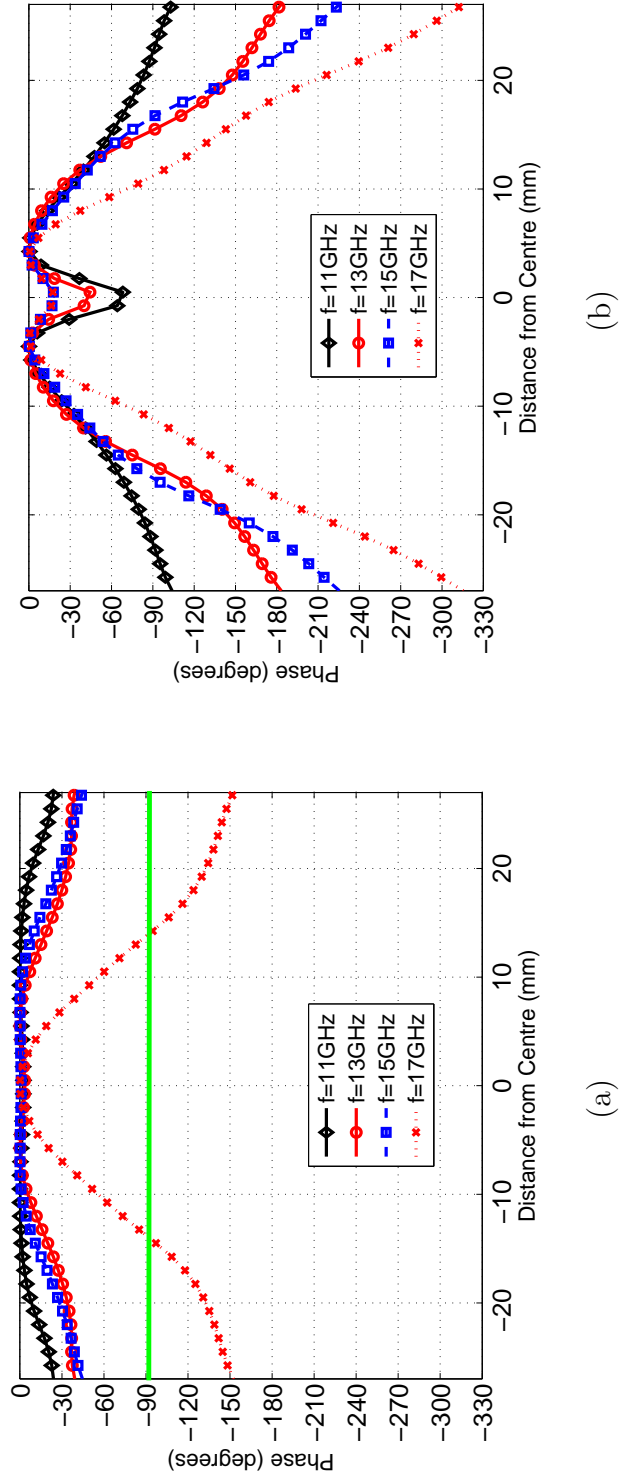


Figure 5.4: Phase distribution for a STPG: (a) above the STPG (b) within the cavity. STPG parameters are: $N = 5$, $\{\epsilon_1, \epsilon_2, \epsilon_3, \epsilon_4, \epsilon_5\} = \{10, 8, 6, 4, 2\}$, $w_1 = 6.87\text{mm}$, $\{w_2, w_3, w_4\} = 5.75\text{mm}$, and $w_5 = 2.875\text{mm}$, $R = \lambda_0$, $t = 0.5\lambda_0/\sqrt{\epsilon_1}$, $h = 0.5\lambda_0$ where $\lambda_0 = 27\text{mm}$.

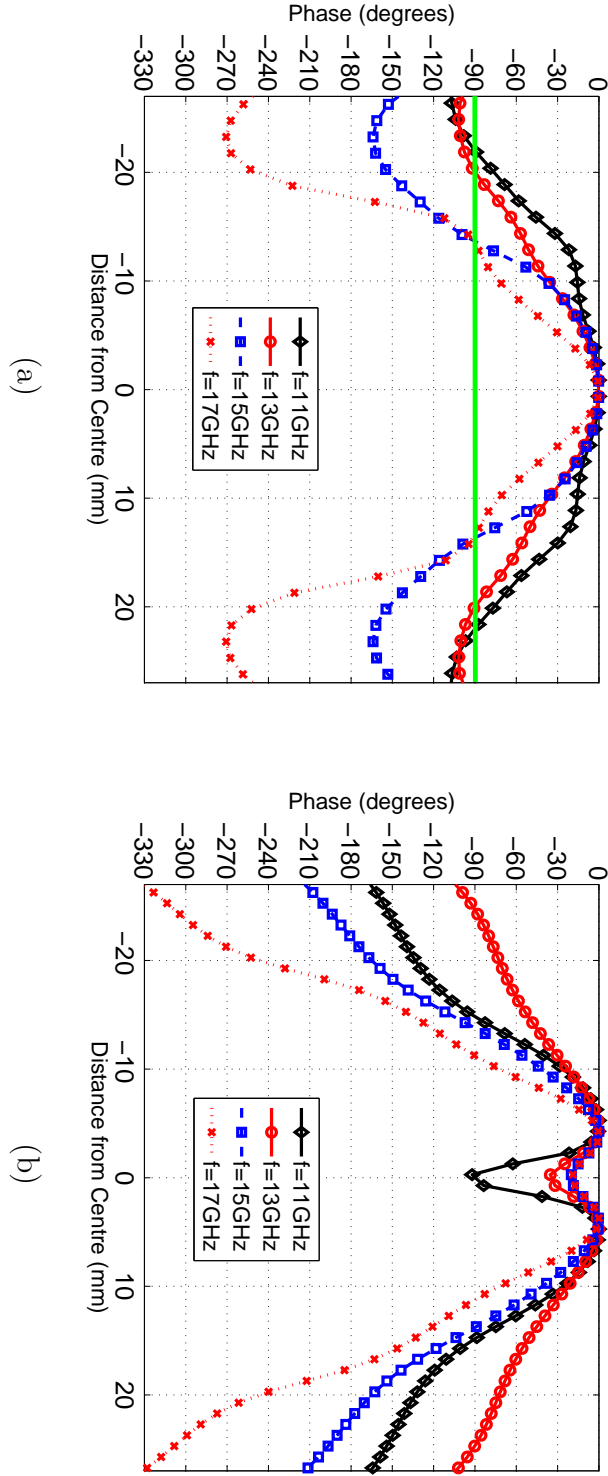


Figure 5.5: Phase distribution for a uniform superstrate. (a) above the superstrate (b) within the cavity . Superstrate parameters are: $N = 1$, $\epsilon_r = 10$, $R = \lambda_0$, $t = 0.5\lambda_0/\sqrt{\epsilon_r}$.

Table 5.3: Comparison of effective in-phase radius ($\Delta\phi \leq 90^\circ$), as a fraction of superstrate radius, of STPG and uniform superstrates.

Frequency (GHz)	11	12	13	14	15	16	17
STPG	100%	100%	100%	100%	100%	89%	50%
Uni. Superstrate	81%	99%	74%	55%	50%	52%	49%

tional to $|\alpha|^2$ in the broadside direction. When $\Delta\phi = 0^\circ$, the two sources produce a power density proportional to $|\alpha_+ \alpha|^2 = 4\alpha^2$. When $\Delta\phi = 90^\circ$, this drops to half the best value, i.e. $|\alpha + j\alpha|^2 = 2\alpha^2$. The worst case occurs when $\Delta\phi = 180^\circ$ due to destructive interference between the two sources. The radius of the aperture within which $\Delta\phi \leq 90^\circ$ can therefore be considered as the effective in-phase radius. In Table 5.3, we list the effective in-phase radius as a percentage of the superstrate radius, and compare the values for the two superstrates over the wide frequency range considered. Clearly, the effective in-phase radius of the STPG aperture is equal to or close to 100% for most of the frequencies. This aperture phase uniformity is a reason for the significantly large directivity bandwidth (10.15 - 17.70 GHz) provided by this STPG, compared to the uniform aperture.

5.6 Prototype Design and Test Results

To experimentally validate the concept, two ERAs were designed: (a) with a square STPG and a ground plane larger than the superstrate, and (b) with a circular STPG and a ground plane whose diameter is equal to the superstrate diameter. Selected experimental results for both ERAs are presented in this section, but the design of only one ERA is discussed here for brevity.

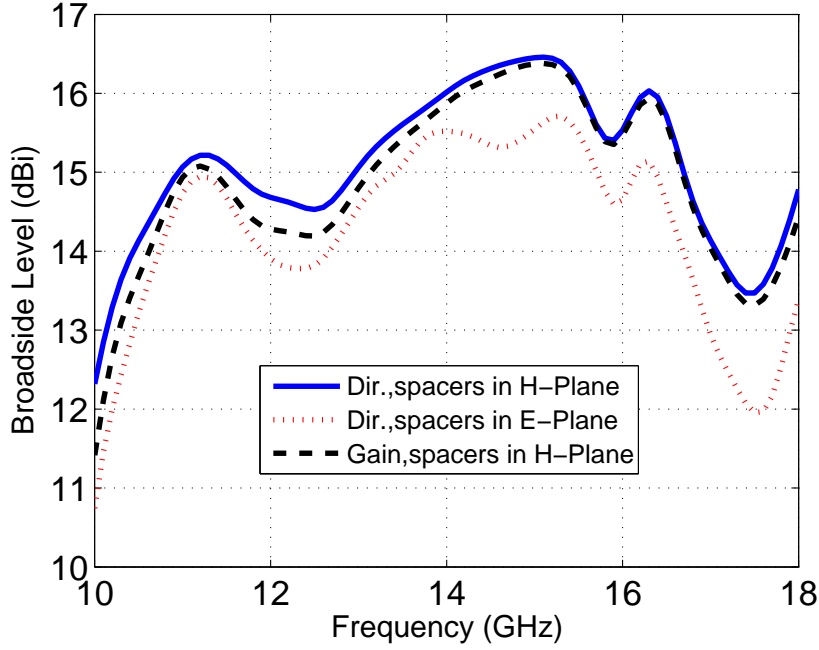


Figure 5.6: Computed directivity and realized gain of the circular ERA. The cavity is excited using a waveguide-fed slot.

5.6.1 Design of ERAs with Feed Antenna

The two ERAs were designed using CST time-domain solver considering commercial availability of dielectric materials. For the circular ERA, $R = 21\text{mm} \approx 0.75\lambda_0$ whereas for the square ERA, the length of each side of the superstructure is $42\text{mm} \approx 1.55\lambda_0$. For both ERAs, $N = 3$, $\epsilon_1 = 10.2$, $\epsilon_2 = 6.15$ and $\epsilon_3 = 3.27$. The superstructure thicknesses (t) for circular and square ERAs are 7.62 mm and 4.4mm, respectively. These values of t were selected to demonstrate wide directivity bandwidths. A waveguide-fed slot was cut in the centre of the ground plane to form the feed antenna. For the circular ERA, predicted results are shown in Fig. 5.6. Its peak gain is 16.4 dBi at 15 GHz and the 3dB gain bandwidth is 51.5%. Two nylon spacers were used to hold the STPG in place above the ground plane, as shown in Fig. 5.7. The spacers were placed in the H-plane to achieve higher gain. Results for two placements of spacers are shown in Fig. 5.6.

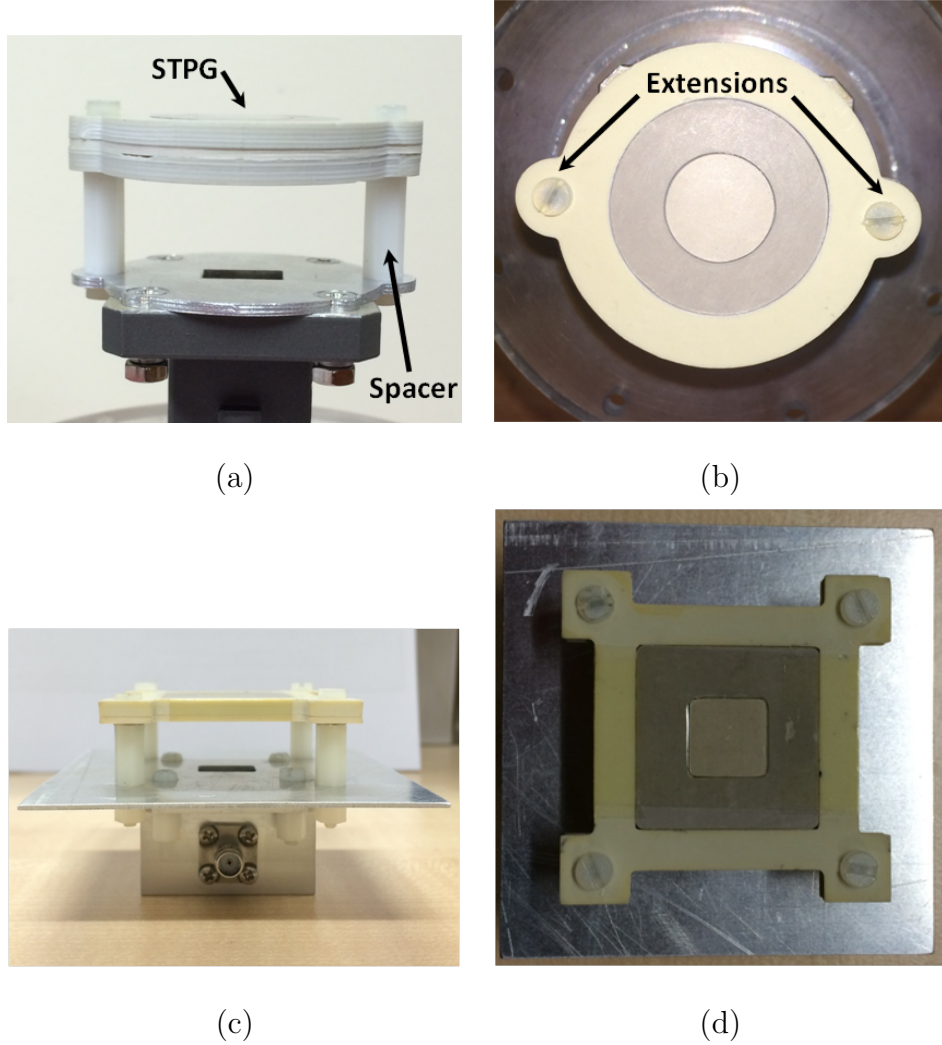


Figure 5.7: Photographs of the prototype ERAs (a) side view of the ERA with circular STPG showing the feed slot and WR-75 waveguide (b) top view of the ERA with circular STPG (c) side view of the ERA with square STPG showing the waveguide adaptor with SMA-to-coax transition; notice the larger ground plane (ground plane size: 75mm \times 75mm) (d) top view of the ERA with square STPG.

5.6.2 Prototype Construction

The two fabricated ERA prototypes are shown in Fig. 5.7. The dielectric materials used for STPG fabrication are RT6010.2 ($\epsilon_1 = 10.2$), RT6006 ($\epsilon_2 = 6.6$), and TMM3 ($\epsilon_3 = 3.27$) by Rogers Inc. The loss tangent of these materials is 0.002. Using subtractive manufacturing and milling, the materials were combined to form a single planar disc. The segment widths w_1 , w_2 , and w_3 are 7 mm for both STPGs. A thin layer of adhesive tape was used to keep the segments in place during the experiments. To hold the superstrate small extensions were provided in the outermost TMM3 rings and nylon spacers were inserted through them, as shown in Fig. 5.7.

5.6.3 Measured Directivity and Gain

Figs. 5.8 (a) and (b) show the measured directivity and gain of the square and circular ERA prototypes, respectively. Both the ERAs exhibit wide directivity bandwidths. The square ERA has a peak directivity of 15.5 dBi and its 3dB directivity bandwidth ranges from 11.6 GHz to 18 GHz (i.e. 43%). As mismatch losses within the directivity bandwidth are negligible in the square ERA, its 3dB gain bandwidth also extends from 11.6 GHz to 18 GHz. Similarly, the maximum measured directivity of 16.4 dBi is observed in Fig. 5.8(b) for the circular ERA. Its 3dB directivity bandwidth extends from 10 GHz to 17.2 GHz (i.e., 52.9%). Although a slightly higher mismatch loss has affected its gain around 11-12 GHz, a 3dB gain bandwidth from 10 GHz to 17.45 GHz (i.e. 54.2%) is noted alongside a peak gain of 15.9 dBi. Overall, the circular ERA has the widest bandwidth as its superstrate is thicker than that of the square ERA. This also validates the findings in Section 5.4.2. The gain was determined using the gain comparison method. For measurement of gain, NSI-RF-SGH-75 and NSI-RF-SGH-51 standard-gain horn antennas were used for 10-15 GHz and 15-18 GHz, respectively.

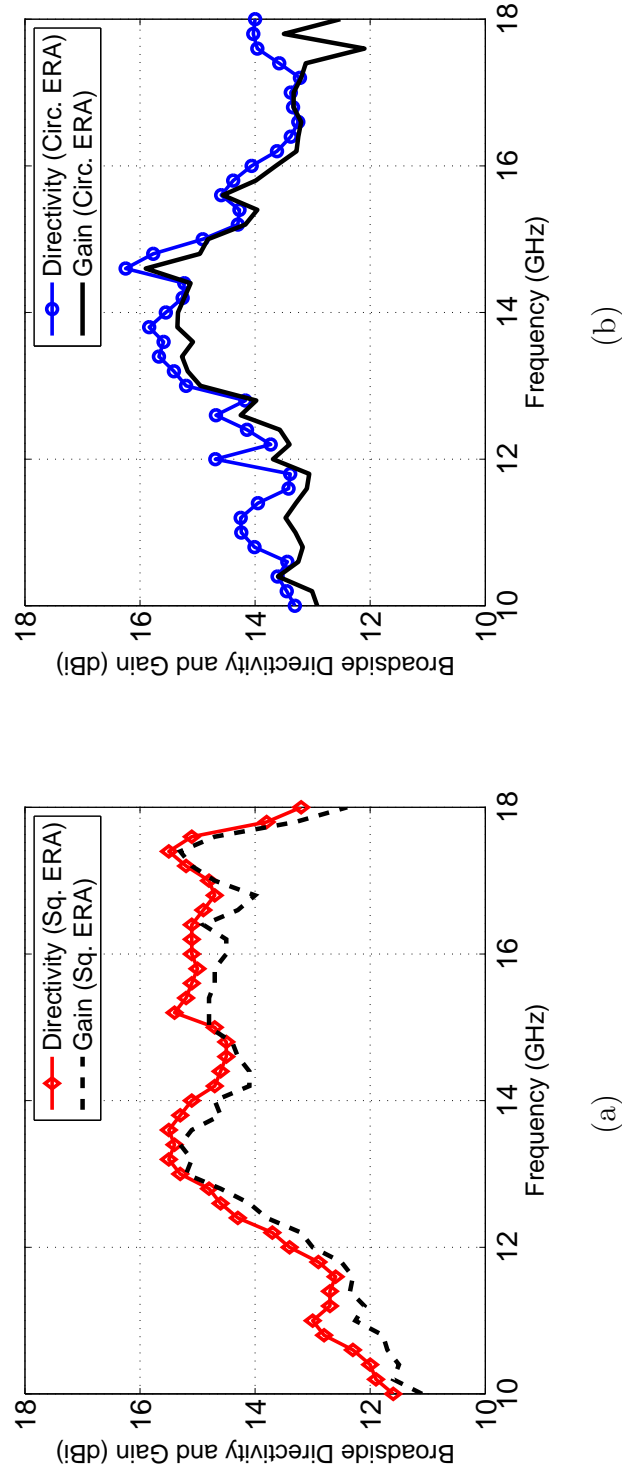


Figure 5.8: Measured directivity and gain of the ERAs (a) Square ERA (b) Circular ERA. The measurements were carried out in the NSI-700S-50 spherical near-field chamber at the Australian Antenna Measurement Facility (AusAMF).

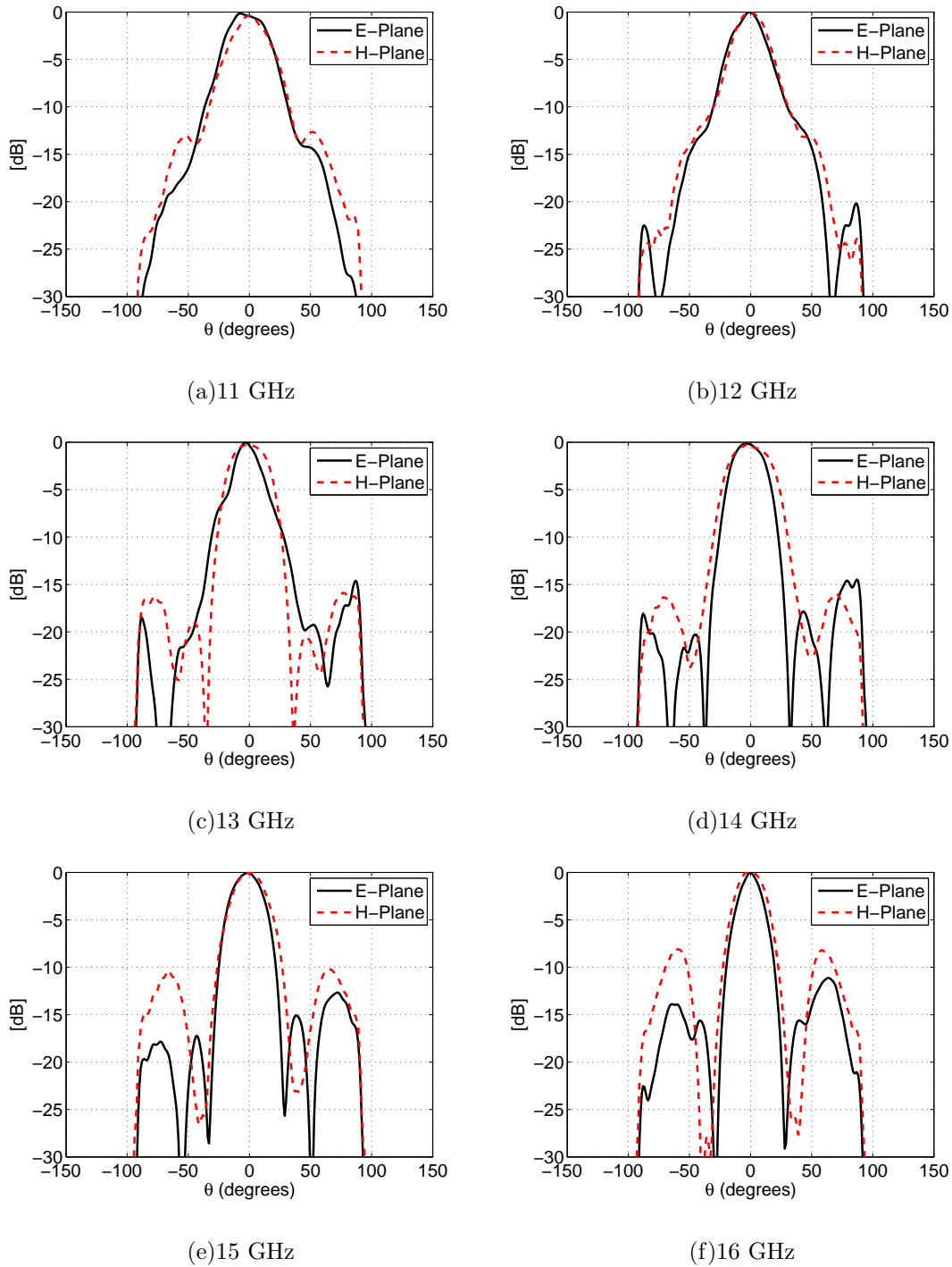


Figure 5.9: Normalised radiation patterns of the square ERA at a six equally spaced frequencies.

5.6.4 Radiation Patterns

E -plane and H -plane radiation patterns of the square RCA are shown in Fig. 5.9 at six frequencies within the directivity bandwidth. It is evident that the beams are directed towards boresight with well behaved side lobe levels (SLLs) over most of the bandwidth. In previous RCAs that are accompanied by large footprints and uniform superstrates, the phase distribution on the superstrate varies continuously as a result of a travelling wave component that propagates inside the cavity in lateral directions. Due to this variation, the SLL increases rapidly as the frequency increases, even within the directivity bandwidth. The proposed RCAs, on the other hand, exhibit comparatively stable SLLs within the operating bandwidth, owing to the phase uniformity above the superstrate. The SLLs in E -plane mostly remain close to -15 dB and rise up to -10 dB near the upper end of the bandwidth. In H -plane, the SLLs are below -12 dB but rise up to -8 dB close to upper frequency limit. This increase in SLL is due to the relatively less uniform surface phase at higher frequencies, as seen from Fig. 5.5 (a). It is worth mentioning that excellent cross polarization performance was noted in measurements, with a worst-case broadside cross polarization level within the 3dB beamwidth reaching -25 dB and an average broadside cross polarisation level of -34 dB within the 3dB directivity bandwidth.

The increase in SLL at higher frequencies (up to -8 dB as shown in Fig. 5.9) can possibly limit the bandwidth shown in Fig. 5.8 to useable bandwidth in some applications that have strict requirements for low SLL. However, it should be noted that the prototypes shown in Fig. 5.7 have been optimised to demonstrate the widest 3dB directivity bandwidths while resorting to the smallest size in order to preserve compactness. In order to achieve low SLL performance, it is possible to design ERAs with STPGs that have a comparatively larger footprint and a finer gradient, such as the one proposed in [71]. The radiation patterns of this ERA are shown in Fig. 5.10, which predict low SLL (< -15 dB) throughout the 3dB bandwidth. However, the STPG in this case has a larger radius

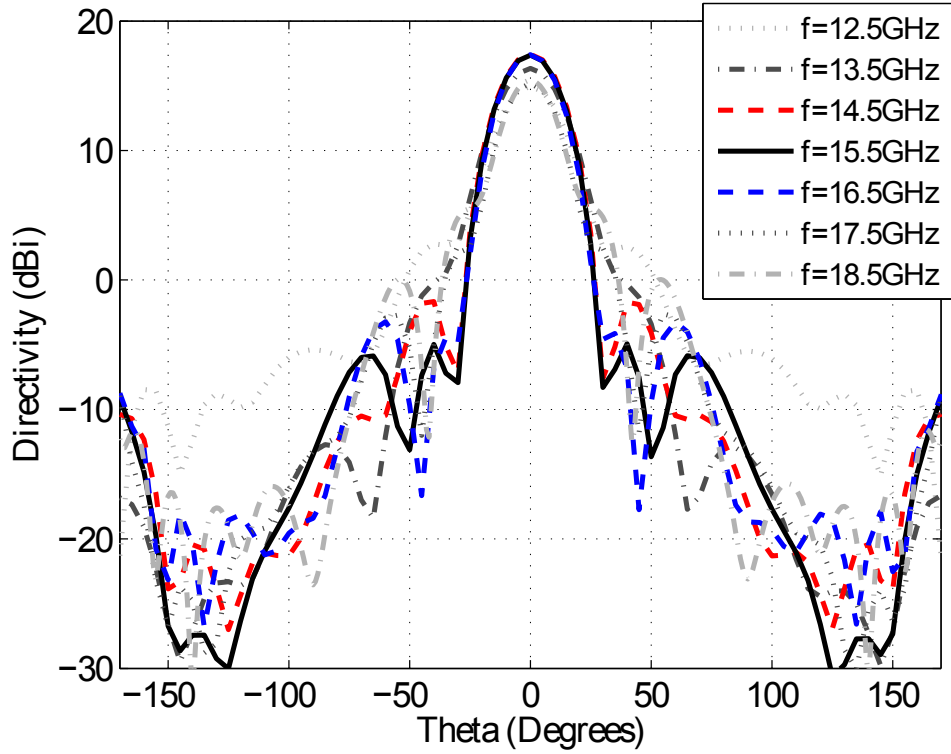


Figure 5.10: E-plane patterns of the ERA proposed in [71] with a larger footprint and fine TPG to achieve low SLL performance. The peak directivity of this ERA is 17.6 dBi.

$R = \lambda_0$, and uses five equi-width sections ($N = 5$) to create the TPG. Thus, the tradeoff to achieve low SLL performance is larger size as well as increased complexity.

5.6.5 Input Matching

To feed the antenna, rectangular slots were individually designed for each ERA prototype. The feeding slot dimensions for the circular and square prototype were $12\text{mm} \times 7.5\text{mm}$ and $13\text{mm} \times 9.5\text{mm}$, respectively. The measured $|S_{11}|$ values of both ERAs are shown in Fig. 6.3. It is found that $|S_{11}|$ remains below -10dB over most of the directivity bandwidth. For the circular ERA, one may notice minor deterioration in $|S_{11}|$, reaching

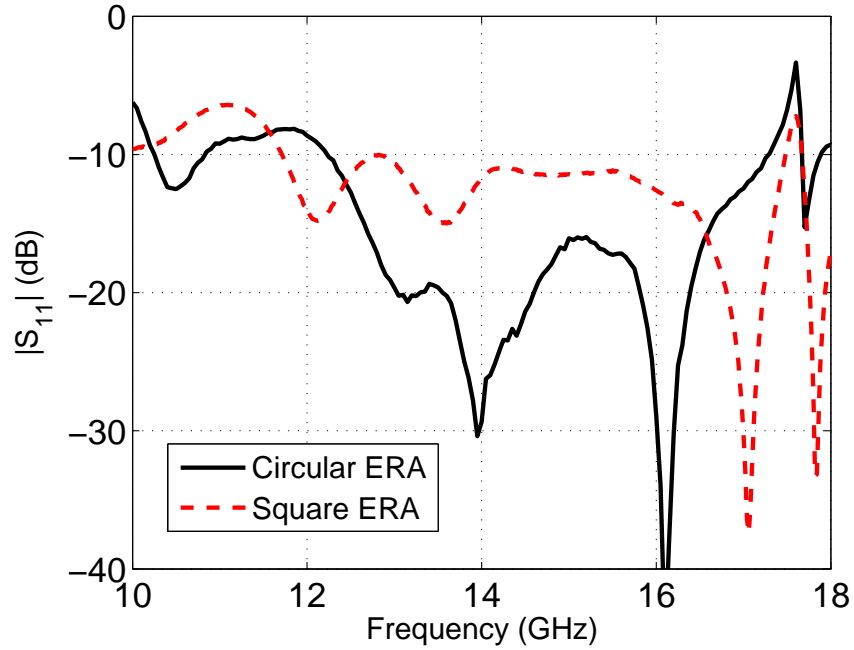


Figure 5.11: Measured input reflection coefficient ($|S_{11}|$) of both ERA prototypes. The input reflection coefficient was measured by an Agilent PNA-X N5242A vector network analyser.

a maximum value of -8.2dB around $11\text{-}12\text{ GHz}$; however, it only reduces the gain of the ERA by approximately 1dB at this frequency. For the square ERA, the $|S_{11}|$ is just above -10dB near the lower limit of directivity bandwidth but remains below -10dB after 11.7 GHz throughout the directivity bandwidth. A sharp spike is observed at 17.55 GHz above the upper end of the bandwidth in Fig. 6.3. This spike is possibly caused by the SMA transition in the commercial WR-75 waveguide adaptor, which was not modelled in the simulations.

5.7 Differentiating ERAs with STPG from Lens-based Antennas

ERAs are an individual class of antennas that is significantly different than lens based antennas (LAs), however, they are commonly confused and compared with LAs as some of the parts look similar in physical appearance. The principle of operation, sizes, heights, and characteristics are so different that the ERAs are not intended to compete with LAs for the same application; rather they are intended for different (e.g. space-critical, topologically-limited) applications. Some key differences between the ERAs proposed in this paper and LAs are discussed below:

5.7.1 Principle of Operation

ERAs require a ground plane and a highly-reflective superstructure, and rely on multiple reflections of EM waves between the ground plane and the superstructure. These multiple reflections result in spreading of the field within the cavity and thus, creating a directive beam towards broadside. Whereas LAs have no ground planes and the lens is often designed to have very low reflection. In LAs, the waves impinging on the surface of the lens are collimated and transmitted through, with minimal or no reflections back towards the feed.

5.7.2 Size and Bandwidth

The ERAs proposed in the manuscript occupy a significantly smaller footprint ($1.54\lambda_0^2$) as compared to lens antennas ($5.39 - 81.2\lambda_0^2$). This is evident by comparing the footprints of the ERA with footprints of LAs in Table 5.4 given below. This compactness leads to a very high directivity-bandwidth product per unit area as shown in Table 5.4 (area is given in terms of λ_0^2 at the lowest operating frequency). “Directivity-Bandwidth-Product per

unit Area” or DBP/A is a figure of merit that judiciously compares an antennas ability to provide high directivity over a wide bandwidth in a certain footprint area. It can be seen from Table 5.4 that the proposed ERAs not only have a very high DBP/Area, but also the widest *measured* directivity bandwidth. This high DBP/A makes the proposed ERAs very suitable for space-limited applications where 15-20 dBi gain is sufficient. On the other hand, LAs can provide higher gains (25-30 dBi) at the expense of larger size, height, and manufacturing cost.

5.7.3 Design Method

In LAs, the lens is often designed such that the air-dielectric interface is well-matched in order to minimize reflection of the incoming waves, and to maximize transmission through the lens. Whereas in ERAs, the superstrates are designed to provide sufficiently high magnitude of reflection that is necessary for spreading the field within the cavity and thus, for achieving directivity enhancement.

5.7.4 Feeding Technique

The feeding technique in ERAs and LAs is usually quite different. LAs are fed using high-directivity feed antennas e.g. horn antennas [113–115], or fed on the surface of the lens for beam-steering e.g. through probes [111,112]. Whereas in ERAs, low directivity simple antennas, e.g. microstrip patch or slot, are used to feed the Fabry-Perot type cavity and the directivity enhancement results solely from the spreading of the field within the cavity due to multiple reflections between the ground plane and the superstrate.

Table 5.4: Differentiating proposed ERAs from lens-based antennas.

	Size	f_{low}	Bandwidth	Height	Peak Directivity	DBP	Footprint Area	DBP/ Λ	Ground Plane	Measured Results
	λ_{low}	GHz	%	λ_{low}	dBi		λ_{low}^2			
This work	Diameter=1.4	10	52.94	0.74	16.4	2,310	1.54	1,501	✓	✓
Ref. [110]	8.2×8.2	51.75	28.75	not avail.	25.5	10,137	67.24	150	-	✓
Ref. [111]	Diameter=4.23	20	76.92	not avail.	20.5	8,630	14.05	614	-	not avail.
Ref. [112]	Diameter=4.46	12.40	36.84	4.30	25	11,650	15.62	754	-	✓
Ref. [113]	Diameter=6.83	8.20	40.78	1.15	29	32,390	36.64	884	-	✓
Ref. [113]	Diameter=10.17	12.2	38.41	1.63	30.5	43,097	81.23	530	-	✓
Ref. [114]	Diameter=6.1	13	32.26	not avail.	27	16,167	29.22	553	-	✓
Ref. [115]	Diameter=2.61	8.2	37.62	1.98	18.2	2,485	5.39	461	-	✓

5.8 Conclusion

We investigated the use of planar, all-dielectric superstrates with transverse permittivity gradients (TPG) to design extremely wideband ERAs. It was found that the 3dB directivity bandwidth can be increased beyond 50% by using appropriately designed single-slab superstrates with TPG. The use of TPG superstrates tremendously enhanced the directivity-bandwidth product also, while providing a sufficiently high level of gain. A measured directivity bandwidth of 52.9% is demonstrated by one of the prototype ERAs, alongside a peak directivity of 16.4 dBi. To the best of our knowledge, no other ERA has such a large directivity bandwidth (52.9%), gain bandwidth (54.2%), directivity-bandwidth product (2,309), or gain-bandwidth product (2,109). The directivity-bandwidth product can be further increased beyond 3,000 using thicker TPG superstrates. The total footprint area of the prototype antenna is very small i.e. only $1.54\lambda_0^2$ at the lowest operating frequency of 10 GHz. A relationship between broadband directivity enhancement of TPG superstrates and their aperture-field phase uniformity was established to provide valuable insight into the underlying principle of operation. ERAs described in [72], made out of multi-layer dielectric slabs, have an axial permittivity gradient (APG) in the superstructure. It is possible to conclude that superstrates with transverse permittivity gradients (TPGs) lead to ERAs with better performance and less height than those with the APGs.

Chapter 6

High Aperture Efficiency Wideband ERAs

6.1 Abstract

An EBG resonator antenna (ERA) with an extremely small footprint is presented. The proposed ERA has a peak measured gain of 15.6 dBi and an excellent measured 3dB gain-bandwidth of 27%. The four-layer composite superstructure used in this ERA takes the shape of a circular disc with the ground plane radius equal to that of the superstructure. Its footprint area is only $1.7\lambda_0^2$ at the lowest operating frequency. The average measured aperture efficiency of this ERA is nearly 90%. The side lobe levels are well below -12dB over most of the operating bandwidth and the cross polarization levels are below -17dB .

Published as: R.M. Hashmi, and K.P. Esselle, "A wideband EBG resonator antenna with an extremely small footprint area," *Microwave and Optical Technology Letters*, vol. 57, No. 7, pp. 1531-1535, 2015.

6.2 Introduction

Data volumes in point-to-point backhaul and subscriber wireless links have significantly increased over the last decade, owing to the dramatic growth of high data-rate internet services. Such wireless links require wideband directive antennas. The space available for these antennas is usually constrained not only by deployment geographies (urban and extra-urban) but also by topological aesthetics. Antennas for such systems require sufficient gain ($>15\text{dBi}$) as well as wide bandwidth. At the same time, some are required to have small footprints. However, achieving high antenna gain in a small footprint area is extremely challenging, especially when it is required over a wide bandwidth.

Electromagnetic band gap (EBG) resonator antennas (ERA) are also known as Fabry-Perot cavity antennas, resonant cavity antennas and 2-D leaky-wave antennas in the research community. These antennas are well known for their simple configuration and highly directive radiation. However, narrow bandwidths (2-14%) [5, 6, 8, 93] and large lateral areas (usually $9 - 36\lambda_0^2$) [6, 8, 10, 12] of conventional ERAs pose a significant limitation for their use in some applications. Though their bandwidth has seen significant improvement during the last decade [10, 12, 13, 72, 116], their large areas have only received limited attention [57, 72, 117]. To obtain best peak directivity from ERAs with conventional superstructures, large footprint areas ($7 - 20\lambda_0^2$) are often employed [10, 12, 13]. However, the all-dielectric composite superstructure, recently introduced in [72], allows dramatic reduction of superstructure area and thereby huge increase in bandwidth without compromising peak directivity.

In this Letter, we present a very small linearly polarized ERA with a total footprint of only 1195mm^2 (i.e. $1.7\lambda_0^2$ at 11.35 GHz, which is the lower limit of the 3dB gain-bandwidth). It has a peak gain of 15.6 dBi and a 3dB gain-bandwidth of 27%. The proposed antenna is suitable for short-to-medium range broadband point-to-point communication systems. Due to the symmetry of superstructure, this antenna can be

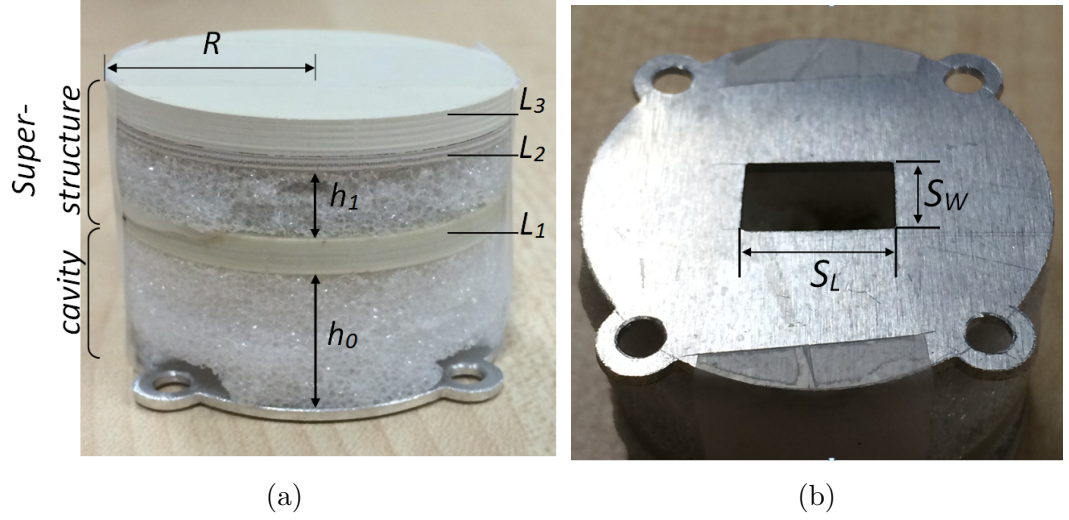


Figure 6.1: Fabricated prototype of the antenna (a) configuration of antenna, and (b) bottom view of antenna showing the feeding slot in ground plane.

extended to dual-linear as well as circularly polarized designs only by replacing the feed.

6.3 ERA Design and Configuration

Small dielectric pucks have been used to improve the gain-bandwidth product of ERAs in [117]. In [57], the contribution of superstructure size in improving the gain-bandwidth product was qualitatively analysed and small areas were found to have better gain-bandwidth products. However, it is common in ERAs to use ground planes which are larger than the superstructure itself. This can still make the footprint of the ERA excessively large, irrespective of the size of the superstructure.

The presented ERA consists of a foam-filled Fabry-Perot cavity, a multi-layer all-dielectric superstructure and an Aluminium ground plane. Its configuration is shown in Fig. 6.1. The cavity height h_0 is 13.5 mm. The superstructure consists of three dielectric layers namely L_1 , L_2 and L_3 , and a foam layer. The foam layer, sandwiched between L_1 and L_2 , has a thickness h_1 of 6.5 mm. The multi-layer superstructure was designed

Table 6.1: *Thickness and relative permittivity of the dielectric layers in the superstrate*

Dielectric Layers	L_1	L_2	L_3
Thickness (mm)	3.175	1.27	3.175
Relative Permittivity (ϵ_r)	3.27	10.2	4.5

using periodic boundary conditions (PBC) in CST Microwave Studio. Following the procedure in [57], superstructure reflection model (SRM) and defect-cavity model (DCM) were used to tune the thickness and relative permittivity of each layer, along with the separation between them. This tuning was done through parametric analyses such that the superstructure provides high reflection magnitude over a wide defect-mode bandwidth. The reflection phase of this superstructure, as seen at the bottom surface of L_1 , exhibited a monotonic, slowly decreasing behaviour. The permittivity and thickness values of each dielectric layer are given in Table 6.1. The gaps h_0 and h_1 are filled with foam instead of air, thus avoiding the need for any additional support to hold the superstructure in its place, contrary to the approach used commonly in [5, 8] and [72]. To minimize the footprint of the ERA, the ground plane and the superstructure are made to have the same radius R of 19.5 mm.

The antenna design was carried out in CST time-domain solver using absorbing boundary conditions. It was followed by prototype fabrication. The materials used to fabricate the prototype were Rogers RT6010.2 LM ($\epsilon_r = 10.2, \tan\delta = 0.002$), Rogers TMM4 ($\epsilon_r = 4.5, \tan\delta = 0.002$) and Rogers TMM3 ($\epsilon_r = 3.27, \tan\delta = 0.002$). Planar discs, having radius R and thicknesses given in Table 6.1, were milled out of each of these materials and were combined together as shown in Fig. 6.1 (a). Adhesive paper tape was used to bind the discs and foam together, and to hold them in plane above the ground plane. A waveguide-fed slot cut in the ground plane was used as the feed, as shown in Fig. 1 (b). The dimensions of the feed slot are $S_{length} = 12.5\text{mm}$ and $S_{width} = 7.5\text{mm}$.

6.4 Numerical and Experimental Results

A prototype of the presented ERA, shown in Fig. 6.1, was measured in a NSI-700S-50 spherical near-field range of Australian Antenna Measurement Facility and Fig. 8.8 shows the measured boresight directivity and gain plotted versus frequency. The gain was measured using the gain comparison method. A maximum gain of 15.6 dBi was measured at 12.75 GHz and the 3dB gain-bandwidth of the ERA spanned from 11.35-14.88 GHz (i.e. 27.7%). It can be seen in Fig. 8.8 that the predicted and measured gain are in good agreement. The simulated gain of a slot antenna, without the ERA superstructure in place, is also shown in Fig. 8.8. An enhancement of nearly 10 dB in the boresight gain is achieved by the presented ERA. The slight variations in the measured gain, specifically, the minor drops at 13 GHz and 13.75 GHz, are attributed to the presence of an acrylic support which was used to mount the antenna in the anechoic chamber.

The input reflection coefficient ($|S_{11}|$) of the ERA, shown in Fig. 6.3, was measured using an Agilent PNA-X N5242A vector network analyser. Fig. 6.3 demonstrates very good agreement between the computed and measured $|S_{11}|$ with a measured impedance bandwidth that extends from 10.65 GHz to beyond 15 GHz. Measured co-polar E - and H -plane patterns are normalized and plotted in Fig. 6.4 for selected frequencies. These patterns clearly show directive beams pointed towards boresight over a wide bandwidth. Although ERA patterns are known to degrade towards the upper limit of the gain-bandwidth, commonly reaching to high values up to -5 dB, it is interesting to note that this ERA demonstrates stable radiation performance over almost the entire gain-bandwidth of 27%. Side lobe levels are found to be below -12.5 dB up to 13 GHz and then rise to -8 dB, only near the high-frequency end. Beam splitting is not observed in the entire bandwidth and cross polarization levels within the main beam were measured to be well below -17 dB.

Table 6.2: Comparison of measured performance parameters of the antenna.

Frequency (GHz)	Gain (dBi)	3dB Beamwidth $E - Plane$	Beamwidth $H - Plane$	Sidelobe Level $E - Plane$	Sidelobe Level $H - Plane$
11.35	12.60	22.5	24.0	-12.90	-13.00
11.80	14.50	31.0	35.5	-13.70	-15.60
12.25	15.26	28.0	26.0	-14.70	-13.40
12.70	15.35	21.0	21.5	-13.20	-14.50
13.45	15.33	22.0	28.0	-8.40	-11.80
14.05	15.05	17.5	19.5	-9.10	-14.60

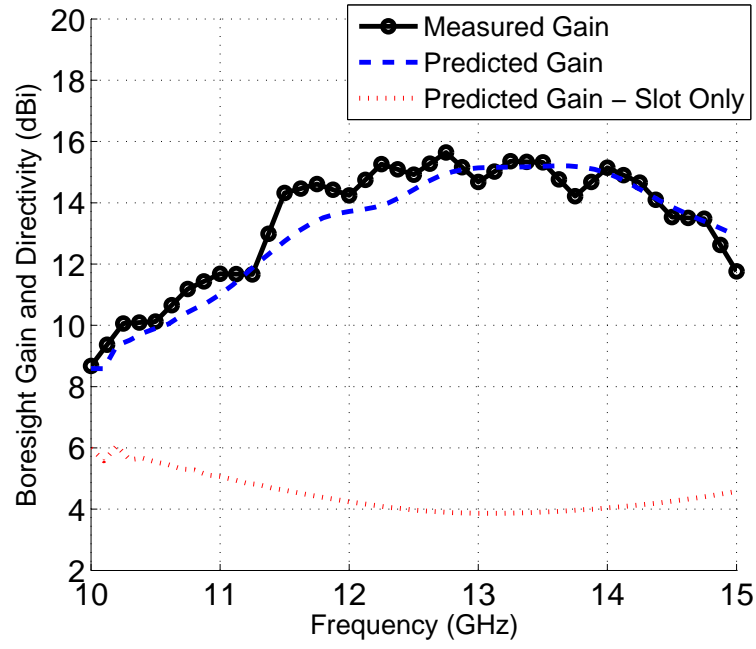


Figure 6.2: Measured directivity and gain of the antenna. The simulated gain of the slot without the ERA superstructure is also shown.

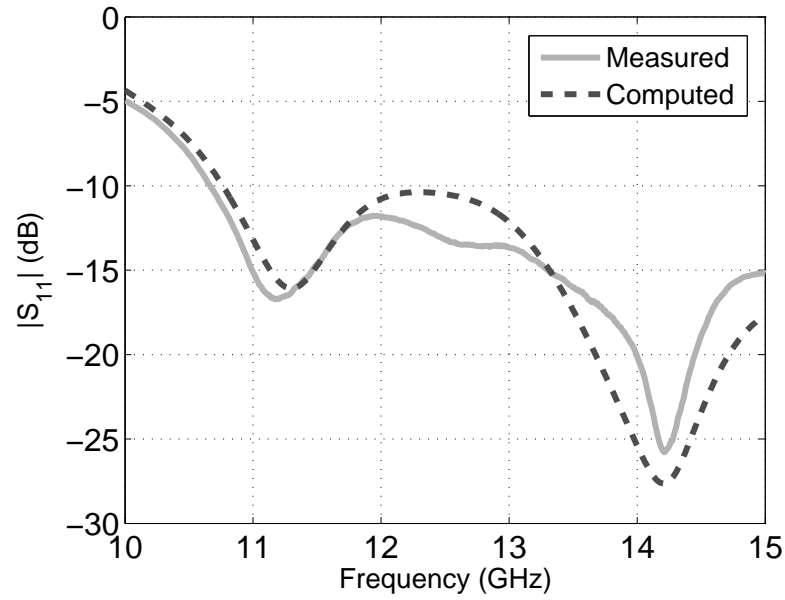


Figure 6.3: Measured and computed input reflection coefficient of the antenna.

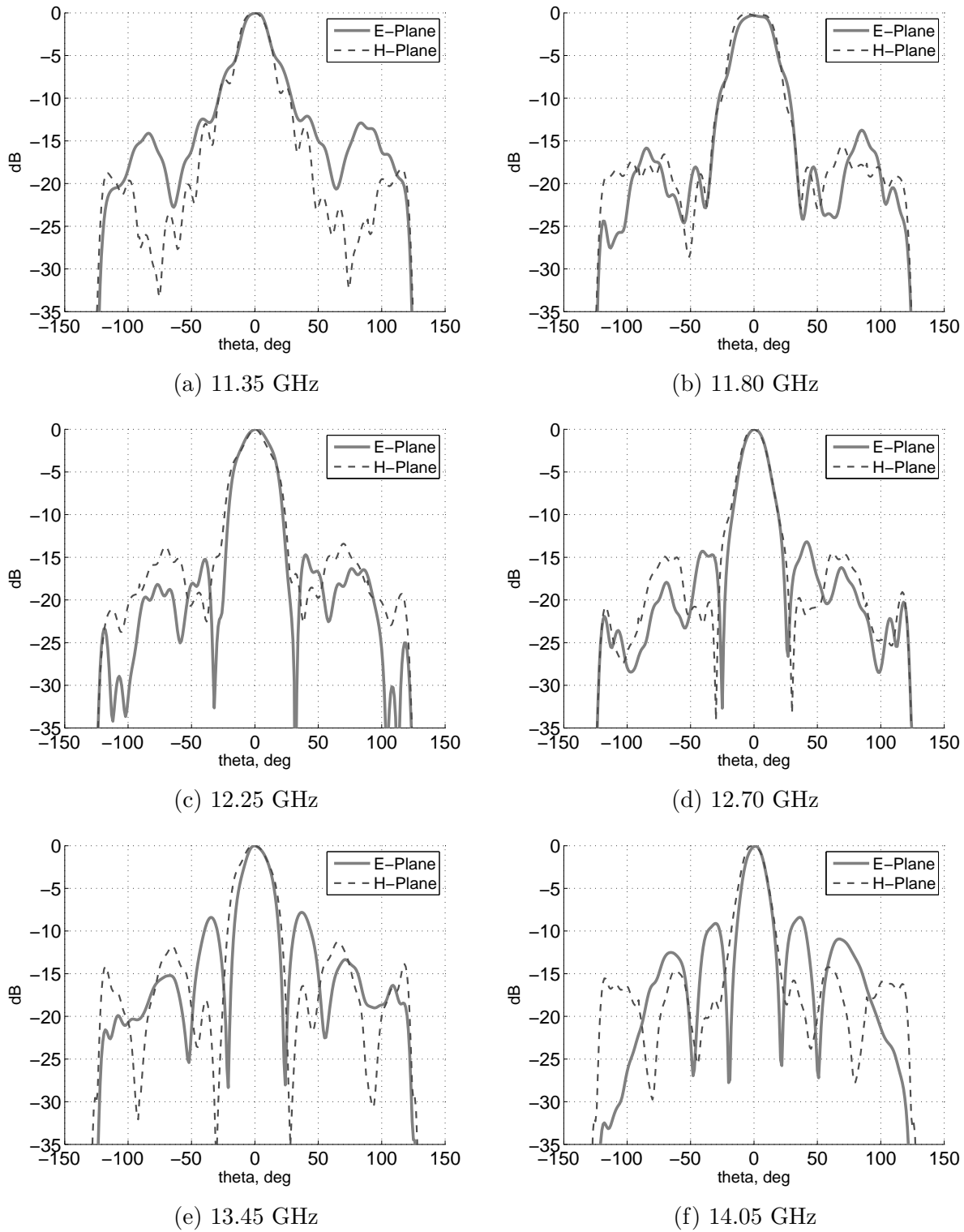


Figure 6.4: Measured radiation patterns of the antenna

6.5 Discussion

An ERA can be considered as a 2-D leaky-wave antenna where a leaky-wave is excited in the centre of the cavity. This leaky-wave propagates radially outwards creating an aperture on the top surface of the superstructure, resulting in a narrow beam at broadside [92]. Classical ERAs often have large lateral areas [5, 6, 8, 12, 13]. In literature, they have often been considered as aperture-type antennas because the radiation from the edges of the superstructure and the ground plane is negligible. On the contrary, the ERA presented here has a strongly truncated superstructure and ground plane, whose footprint area is nearly 38% less than the smallest ERA proposed so far [72]. Radiation from the edges is therefore strong, but it adds coherently to the radiation from the top surface. This creates a strong main beam over a wide bandwidth, instead of creating undesirable minor lobes. For this circular ERA, aperture efficiency η_{ap} is given by

$$\eta_{ap} = \frac{A_{effective}}{A_{physical}} = \frac{\lambda_0^2 G}{4\pi^2 R^2} \quad (6.1)$$

where G is the antenna gain, λ_0 is the free-space wavelength and $A_{physical}$ is the area of the antenna in azimuth plane, which is indeed the area of ground plane or superstructure, given by πR^2 . The peak measured aperture efficiency for this ERA was found to be 135% at 12.75 GHz and the average aperture efficiency over the 3dB bandwidth was approximately 90%. It has been confirmed in the literature that η_{ap} can, in some cases, exceed 100% [118–120]. This occurs because such antennas, for instance the spline profile horn antenna in [118] and the microstrip arrays in [119] and [120], are not pure aperture antennas and their total radiation is the sum of radiation from the aperture and other sources such as structure edges, or flanges. Similarly, unlike the classical ERAs, the ERA proposed in this Letter is not a pure aperture-type antenna due to strong truncation, however, as in the case of the horn antennas in [118], η_{ap} can still be a useful figure of

Table 6.3: Comparison of figures of merit

	Peak η_{ap} (%)	Peak Gain (dBi)	Gain-Bandwidth (%)	$BAEP$ (% ²)
Ref. [119]	105	14.9	18.4	1,932
Ref. [120]	144	11.6	7.1	1,022
This Work	128	15.5	27.7	3,545

merit to quantify its ability to provide high gain in a small lateral area.

Achieving such a high η_{ap} together with a peak gain greater than 15 dBi and a wide 3dB gain-bandwidth is extremely difficult. Maximum measured aperture efficiency achieved from a microstrip array is claimed to be 105% [119]. This E-shaped patch array was realized through powerful evolutionary optimizations. It has a measured peak gain of 14.9 dBi and a bandwidth of 18.4%. A capacitive-loaded printed dipole array, proposed in [120], has a predicted aperture efficiency of 144%, a peak gain of 11.6 dBi and a bandwidth of 7.1%.

Table 6.3 compares some antennas which have exceedingly high values of η_{ap} based on their gain-bandwidth product. However, the gain-bandwidth product only takes into account the peak gain and the 3dB bandwidth of an antenna. Therefore, to put these figures in perspective along with an antenna's ability to provide wide bandwidth with high gain in a small area, let us define another figure of merit, the bandwidth-aperture-efficiency product (BAEP), as

$$BAEP = \eta_{ap} \times Bandwidth(\%) = \frac{\eta_{ap}(f_H - f_L)}{f_H + f_L} \times 100 \quad (6.2)$$

where f_H and f_L are the upper and lower bounds of the 3dB gain-bandwidth and η_{ap} is the percentage aperture efficiency. Being the product of two percentages, the unit of $BAEP$ is squared percentage. In Table 6.3, it can be observed that the presented ERA, in addition to a high gain-bandwidth product, has a very high $BAEP$ due to its good gain

and small footprint area. Moreover, this ERA experimentally demonstrates that a wide 3dB gain-bandwidth can be achieved if a superstrate offers a high reflection magnitude over a wide defect-mode bandwidth.

6.6 Conclusion

An EBG resonator antenna (ERA) with an extremely small footprint has been presented along with its experimental results. The ERA employs a significantly truncated circular composite superstructure, which is made out of unprinted dielectric layers, and a truncated ground plane. To the best of our knowledge, no other planar antenna with such a small footprint presents a broadside gain greater than 15 dBi with a matched 3dB gain-bandwidth exceeding 20%. Although this ERA is taller than microstrip patch and some other planar arrays, its very small lateral area is a great advantage in footprint-limited point-to-point applications. The presented ERA is simple to construct, can provide high gain in a very small lateral area and is able to support linear, dual-linear and circular polarizations, with appropriate modifications to the feed.

Chapter 7

Arrays of High Aperture Efficiency Wideband ERAs

7.1 Abstract

Wideband arrays of high aperture efficiency EBG resonator antennas are proposed and studied in this paper. The performance of these arrays is characterized based on their directivity and the 3dB bandwidth they can provide. Two configurations of ERAs made out of the same superstructure are compared: (a) an array of high aperture efficiency ERAs and (b) a single ERA with multi-point excitation. It is shown that although the footprint of both the configurations is the same, the array is not only more directive but also presents a significantly higher bandwidth potential. Numerical results are presented to demonstrate a configuration approaching a peak directivity of 21.3 dBi over a

Published as: R.M. Hashmi, and K.P. Esselle, "Arrays of high aperture efficiency wideband EBG resonator antennas," (Invited Paper), *17th International Conference on Electromagnetics in Advanced Applications (ICEAA)*, Turin, Italy, 7-11 September, 2015.

3dB bandwidth of 37%.

7.2 Introduction

Recent developments in the field of electromagnetic band gap (EBG) resonator antennas (ERA) have demonstrated excellent potential for their extended use in modern communication systems [72, 121, 122]. ERAs are superstrate based planar antennas that are well-known for their simple configuration and highly directive broadside radiation [8, 9, 72, 121, 122]. In addition to microwave applications, they are promising candidates for millimeter-wave wireless applications [34, 123]. These simple and planar antennas have advantages such as low cost, ease of fabrication, and easy integration in space-limited applications.

ERAs are also known as Fabry-Perot cavity antennas, resonant cavity antennas, and 2D leaky-wave antennas. Since the last decade, ERAs have been the focus of several research groups that have addressed aspects such as profile reduction, bandwidth enhancement, and compactness [9, 15, 72, 121, 122]. Limited bandwidth and large footprint areas the most widely addressed aspects of ERAs. Wide defect-mode EBG structures (so called composite superstructures (CSS)) have been designed to significantly improve the 3dB directivity bandwidth of ERAs [72]. In these CSS-based ERAs, it was found that the peak directivity is unaffected with changes to the superstructure footprint, contrary to the case observed with classical ERAs where the peak directivity increases with an increase in superstructure footprint. This led to the design of extremely small footprint ERAs that offer high gain and wide bandwidth at the same time. Recently, an ERA with a total footprint of only $1.7\lambda_0^2$ demonstrated a measured 3dB bandwidth of 27.7% alongside a peak gain of 15.6 dBi [15]. The average aperture efficiency (η_{ap}) of this ERA was approximately 90% over the 3dB directivity bandwidth with a peak η_{ap} of 135% at

12.75 GHz.

In this work, we investigate the performance of arrays of such high aperture efficiency wideband ERAs (high- η_{ap} ERA). Previously, multi-point excitation of arrays has been proposed to enhance the directivity bandwidth of ERAs while providing high gain [10]. An ERA having a dual-resonator 1D EBG superstructure excited by 4×8 slot array feed demonstrated a measured directivity bandwidth of 13% and a peak gain of 21 dBi. The total footprint of this ERA was $6\lambda_0 \times 6\lambda_0$. Also, sparse arrays have been treated as excitation for multi-layer ERAs in the past [89]. However, the high- η_{ap} ERA proposed in [15], given its small footprint, wide bandwidth and high gain, can be used to design arrays of ERAs. We compare the performance of a multi-point excitation ERA with a 2×2 array of high- η_{ap} ERAs. Both, the multi-point excitation ERA and the elements of high- η_{ap} ERA employ the same CSS as superstrate and occupy the same physical footprint. It is found that while both the multi-point excitation ERA and the high- η_{ap} ERA array offer a peak gain around 20 dBi, the latter offers significantly wideband performance. Moreover, the elements of array are much smaller compared to the multi-point excitation ERA and thus, the array has marked advantages in terms of material and fabrication cost, as well as the total weight.

7.3 Configuration of Antennas

The CSS employed here is designed by unit-cell analyses using the superstructure reflection model (SRM) and defect-cavity model (DCM) described in [72]. It consists of three dielectric layers with thicknesses $t_1 = t_3 = 3.2mm$, and $t_2 = 1.3mm$. The respective permittivity values are $\epsilon_1 = 3.27$, $\epsilon_2 = 10.2$, and $\epsilon_3 = 4.5$. The air-gaps h and h_1 , as shown in Fig. 7.1 and 2, are 13.5mm and 6.5mm, respectively. For the 2×2 array shown in Fig. 7.1, the superstructure and the ground plane take a circular shape and have equal

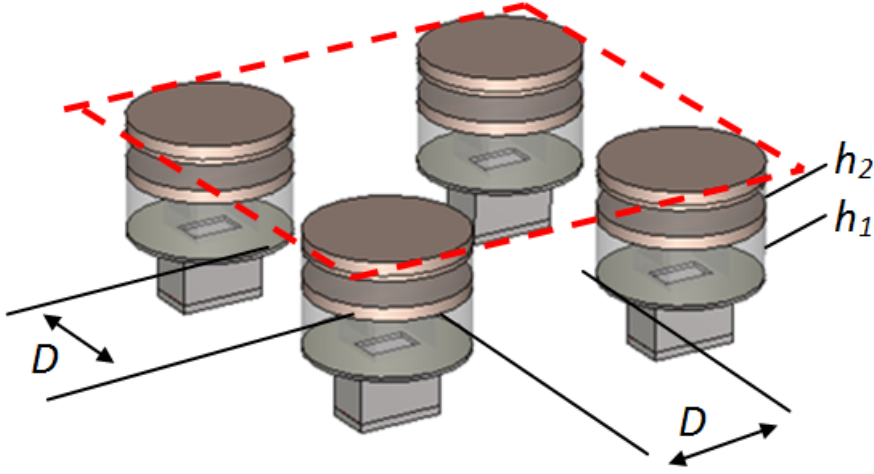


Figure 7.1: The 2×2 array high- η_{ap} ERAs. The spacing between the elements is designated by D . The physical footprint of the array assembly is marked by dashed lines.

radii, $R = 19\text{mm}$ which equals $0.7\lambda_0$ at 11.5 GHz. The dimensions of the slot in ground plane are $11\text{mm} \times 9\text{mm}$, which is fed by WR-75 waveguide. The elements are spaced apart a distance $D = 1\lambda_0$. The multi-point excitation ERA is shown in Fig. 7.2 where the CSS parameters are the same as the high- η_{ap} ERAs. The superstructure and the ground plane have a total footprint of $3.8 \times 3.8\lambda_0$. The slots are excited using WR-75 waveguide.

7.4 Numerical Results

Fullwave time-domain simulations of the multi-point excitation ERA and the high- η_{ap} ERA array were conducted in CST Microwave Studio. Fig. 7.3 shows the broadside directivity of a single high- η_{ap} ERA element, as proposed in [15]. The 3dB directivity bandwidth extends from 11.1 to 16 GHz, with a peak gain of 15.4 dBi. The computed broadside directivity of a 2×2 array of these high- η_{ap} ERAs is also shown in Fig. 7.3. When the separation between the elements is $D = 0.5\lambda_0$, the 3dB directivity bandwidth

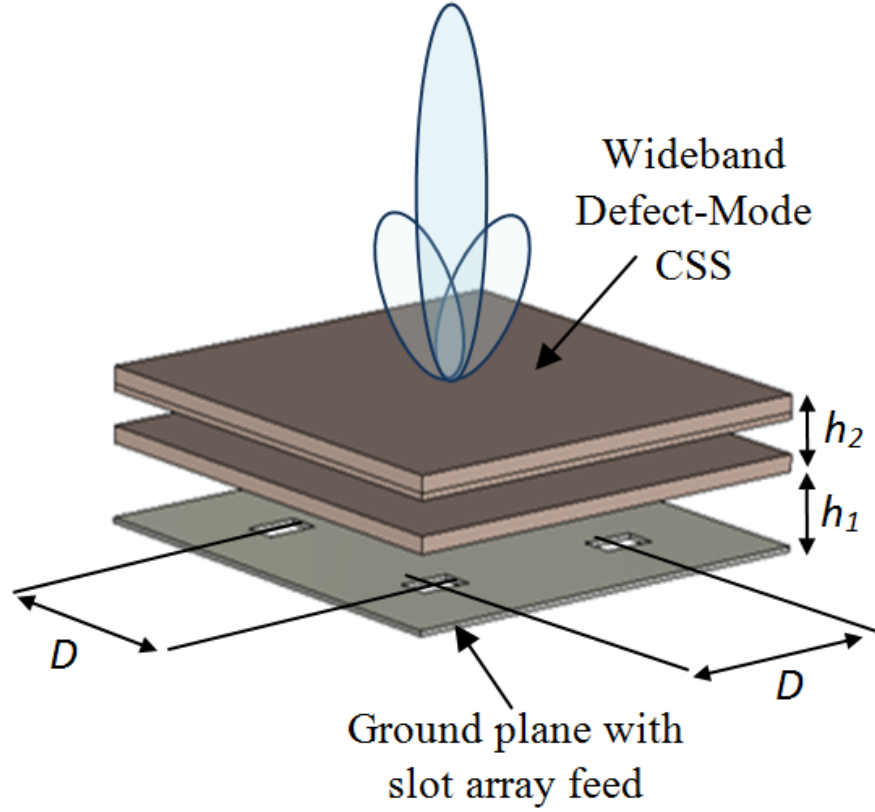


Figure 7.2: An multi-point excitation ERA. The cavity is excited by an array of slot antennas. The CSS has a footprint of $3.8\lambda_0 \times 3.8\lambda_0$ and the spacing between the slots is $D = 0.5\lambda_0$.

of this array spans over 11.12-16.26 GHz with a peak gain of 21.3 dBi whereas when $D = 1\lambda_0$, the bandwidth ranges from 11.1-16 GHz with a peak gain of 21.4 dBi. The feed antennas were found to be well matched throughout these bandwidths with reflection coefficient below -10dB .

Fig. 7.4 shows the broadside directivity of the multi-point excitation ERA when excited using a single slot as compared to when a 2×2 array of slots is used for excitation. Multi-point excitation improves the directivity bandwidth as well as the gain of this ERA, in accordance with the findings reported in [10, 89]. When the inter-element separation between the slots is $D = 0.5\lambda_0$, the bandwidth ranges from 11 GHz to 12.8 GHz, with

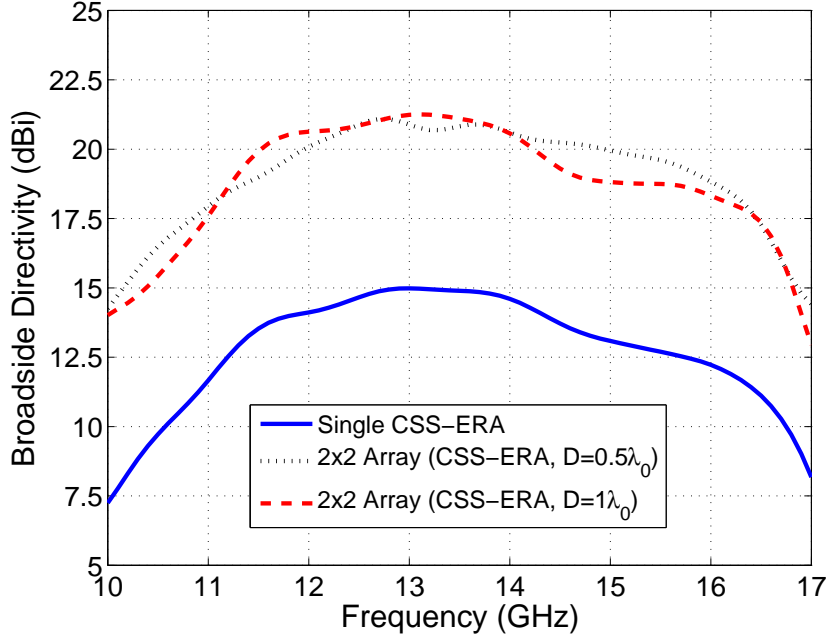


Figure 7.3: Broadside directivity of the high- η_{ap} ERA array shown in Fig. 7.1 for two different configurations. The broadside directivity of a single ERA is also shown for reference.

peak directivity approaching 20.3 dBi. Whereas when $D = 1\lambda_0$, the bandwidth extends from 11 GHz to 14.4 GHz, with peak directivity reduced to 18.7 dBi. The feeding slots showed good impedance match over the respective directivity bandwidths in all the cases, similar to the feeding slots used in the high- η_{ap} ERA array.

7.5 Discussion

It was found that the directivity of the high- η_{ap} ERA was increased by nearly 6dB when arranged to form an array of 2×2 elements, besides, bandwidth remained unaffected. When $D = 0.5\lambda_0$, the directivity bandwidth of the high- η_{ap} array was 37% whereas that of the multi-point excitation ERA was 15%. This represents that the high- η_{ap} array can provide 1.5 times more directivity bandwidth than the multi-point excitation ERA.

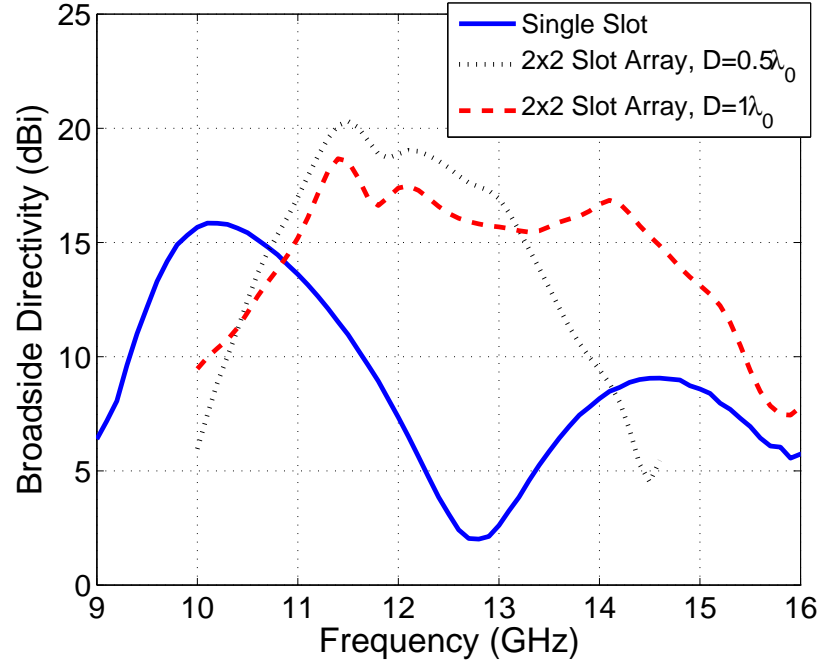


Figure 7.4: *Broadside directivity of the multi-point excitation ERA shown in Fig. 7.2 when a single feed was used, compared with the case when array excitation was used.*

Comparing the results in Fig. 7.3 and Fig. 7.4, it can be seen that the high- η_{ap} ERA array not only has higher bandwidth potential than the multi-point excitation ERA, but also provides nearly a 3dB improvement in directivity. It is interesting to note that total physical footprint occupied by the array and the multi-point excitation ERA is the same, but in the case of the array, 53% of this footprint comprises of free space. This means that the material required for constructing the array is significantly less compared to the classical ERAs that are excited by multi-point feeding. This characteristic is very attractive as it not just reduces the associated fabrication cost of the array, but also the weight of the antenna. Moreover, the directivity enhancement obtained by the array has much flatter response over the bandwidth as opposed to the response of multi-point excitation ERA. A shift in frequency can be noticed in Fig. 7.4 when a single feed is replaced by the array feed, however, the cause of this shift is beyond the scope of this

paper.

7.6 Conclusion

Simple arrays of high aperture efficiency EBG resonator antennas were studied. The performance of such arrays was compared with classical ERAs having multi-point excitation. Such arrays offer significantly higher bandwidth potential and higher peak directivity than classical multi-point excitation ERAs. An enhancement of nearly 1.5 times was obtained in bandwidth alongside a 6 dB enhancement in ERA directivity. These arrays are volumetrically smaller than classical ERAs occupying the same physical footprint and can provide improved performance in terms gain, bandwidth as well as cost of manufacturing.

Chapter 8

Investigation into the Effects of Superstructure Finiteness in ERAs

8.1 Abstract

The role of superstructure finiteness in improving the peak directivity and the directivity bandwidth of electromagnetic band gap (EBG) resonator antennas (ERAs) is studied. Simple one- and two-layer superstructures consisting of unprinted dielectric slabs are used for this purpose. In the latter case, each dielectric slab is truncated individually to improve the ERA performance. Initially, existing analytical models that only take into account the reflection characteristics of the superstructure are used to predict the peak obtainable directivity and the directivity bandwidth. Detailed numerical studies are then conducted to observe the validity of these analytical predictions and to study the ERA performance for various finite sizes of the superstructure.

In review as: R.M. Hashmi and K.P. Esselle, "Enhancing Performance of EBG Resonator Antennas by Individually Truncating Superstructure Layers," *Microwaves, Antennas & Propagation, IET*, 2015.

It is found that directivity bandwidth as well as the peak directivity of the antenna is strongly influenced by the size of the superstructure. Moreover, in case of two-layer superstructures, carefully designing each layer to have a different finite size improved the directivity bandwidth product of an ERA by more than 65%. Experimental results of three ERA prototypes are presented to validate the trends observed in the numerical findings.

8.2 Introduction

A high reflectivity superstrate placed above a simple radiating source backed by a ground plane can significantly enhance its directivity [5, 36, 39]. This enhancement is obtained when the radiated waves undergo multiple reflections within the Fabry-Perot cavity, which is formed between the superstrate and the ground plane [4, 5]. The resulting antenna configurations are known as EBG resonator antennas (ERAs) [4, 7, 8], also well known as resonant cavity antennas (RCAs) [5, 124], or 2D leaky-wave antennas (2D-LWA) [39, 84], depending upon the analytical model used to study their behaviour. The superstrates can be of various types such as a 1D stack of dielectric layers [4, 8], 2D frequency selective surface (FSS)/partially reflecting surface (PRS) [5, 124], or 3D band gap structures [7, 52]. Thus, a more general term “superstructure” is used to encompass all these different types of superstrates. ERAs are simple antennas which are very attractive as they provide an alternative means to achieve high directivity using only a single source, in contrast to conventional methods that are complex as well as expensive. However, classical ERAs suffer from narrow bandwidths usually 1-3%, and large lateral size (referred as footprint or area), often approaching $20-36\lambda_0^2$.

It is well-known that the area of the superstructure determines the “effective aperture” of an ERA, and therefore, its directivity [52]. The total field radiated by an ERA is mainly

composed of two contributions. The first is the field radiated by the effective aperture which is created on the superstructure due to the resonance in the cavity. This contribution is primarily dependent on the characteristics of the superstructure and in part, on the characteristics of the feed antenna. It has been thoroughly studied in the past and various methods have been proposed to maximize the directivity obtained by a particular superstructure [8, 10, 49, 66, 76]. The second contribution is by the field diffracted from the edges of the finite-superstructure. This diffraction may be due to the transverse propagation of waves within the cavity, or by surface waves that exist on the superstructure, and are diffracted as they encounter a discontinuity. These surface waves generally do not contribute to the field radiated by the antenna, except when they undergo diffraction at the edges [95]. Since the conventional ERA superstructures are truncated such that the magnitude of the field reaching the edges has significantly decayed ($\approx -30\text{dB}$), the effects of field diffracted from the edges remain dormant. Moreover, traditional methods to study the performance of ERAs solely rely the reflection or transmission characteristics of their superstructures, employing plane-wave models that assume infinite transverse extent of the superstructures. Thus, to the best of our knowledge, the contribution of the field diffracted from finite sized superstructures is neither accounted for in any of the analytical models, nor has it been studied in the past.

Recently, ERAs having superstructures with significantly reduced areas than conventional designs have been proposed [15, 98, 117]. Their design methodology was based on plane-wave models, followed by parametric analyses of the composite antenna, and was primarily aimed to achieve wide directivity bandwidths. Interestingly, it was observed that when the superstructure areas of these ERAs were reduced, the 3dB directivity bandwidths improved significantly, further beyond the improvement predicted by the plane-wave models. This improvement in directivity bandwidth has been attributed to the reduced size of the superstructure [72]. In this paper, we aim to systematically study

the effect of superstructure-finiteness on the peak directivity and the directivity bandwidth of ERAs. For this purpose, detailed case studies are conducted using simple 1D dielectric superstructures consisting of one- and two-layers. Initially, a plane-wave model is used to predict the performance of ERAs resulting from these superstructures and later on, the effect of varying the superstructure area on performance of ERAs is studied. It is found that even without any special treatment of the superstructure properties, selection of the area notably influences the directivity bandwidth. Particularly intriguing cases are observed when the dielectric layers in the two-layer superstructure are assigned to different finite sizes, i.e., individually truncated. Although, smaller superstructures have been used in the past to yield wider bandwidths with reduced directivity, we experimentally demonstrate that effectively truncating the layers in ERA superstructures to different finite sizes can yield more than 65% improvement in the directivity-bandwidth product, while resorting to the same physical footprint. The rest of the paper is organised as follows: Section II describes the general configuration and characterization of the superstructure and the ERA that is used in the case studies presented in this paper. Analytical predictions are made for the peak directivity and bandwidth of this ERA using the ray-tracing approximation. In Section III, the findings of the case studies are discussed for the one- and two-layer superstructure, respectively. Section IV presents the measurements, experimental results, and discussion, followed by conclusion in Section V.

8.3 Highly Reflective 1-D Dielectric Superstructure

Side view of a typical ERA with a highly-reflective, two-layer superstructure is shown in Fig. 8.1 (a). The superstructure is made out of two dielectric layers L_1 and L_2 , which are separated by an air-gap of $h_2 = \lambda_0/4$, where $\lambda_0 = 25mm$ is the free-space wavelength at 12 GHz. Both L_1 and L_2 have the same thickness $t = \lambda_0/4\sqrt{\epsilon_r}$, and relative permittivity

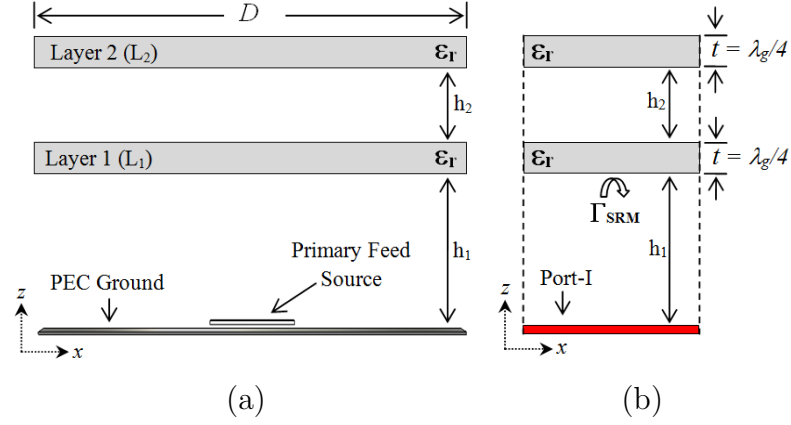


Figure 8.1: Configuration of a typical ERA with a two layer superstructure: (a) side view of the ERA formed by employing the highly reflective 1D superstructure (b) plane-wave model of the two-layer superstructure used to compute reflection characteristics.

$\epsilon_r = 4.3$ (corresponding to commercial FR4 material). In xy -plane, the superstructure has dimensions $D \times D$ whereas the aluminium ground plane is slightly larger with the dimensions $(D + \lambda_0/2) \times (D + \lambda_0/2)$. The superstructure is held at a height $h_1 = \lambda_0/2$ above the ground plane. In the following case studies, a theoretical point source is used to excite the Fabry-Perot type cavity. Instead, for experimental prototypes, waveguide-fed slots cut in the ground plane were used as primary feed antennas.

8.3.1 Superstructure Characterization

To study the effects of superstructure finiteness, a simple 1D EBG structure consisting of two dielectric layers is chosen (see Fig. 8.1 (a)). The idea is to quantify the performance of the ERAs without any special treatment of the superstructures. Although the studies presented here are for one- or two-layer superstructures, the findings can be generalized for multi-layer superstructures as well. A plane wave model (referred as superstructure reflection model (SRM)) of this superstructure is shown in Fig. 8.1 (b). The SRM is used to compute the complex reflection coefficient (Γ_{SRM}) when a linearly-polarized plane wave is

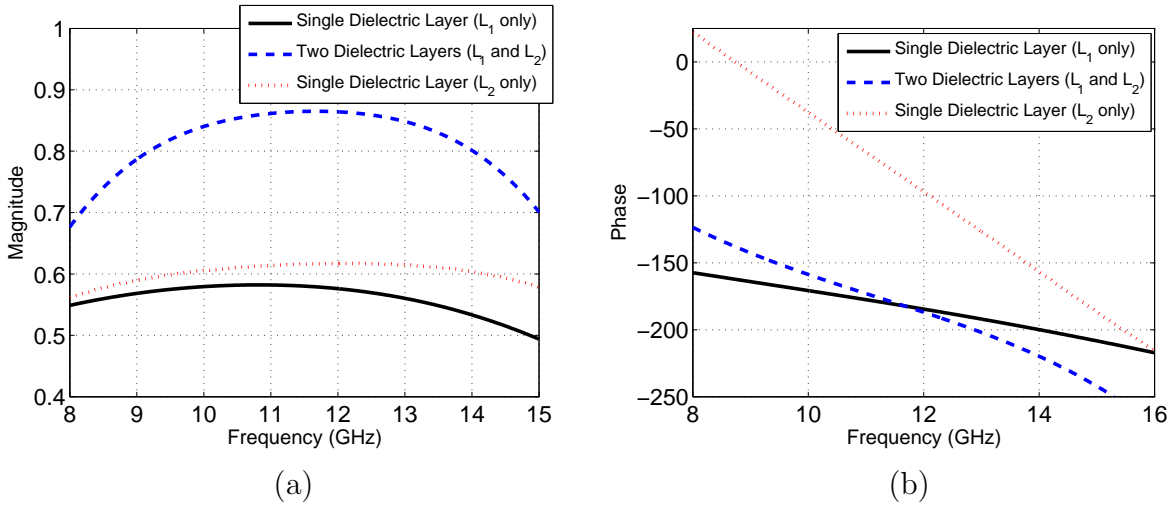


Figure 8.2: Complex reflection coefficient of the superstructure shown in Fig. 8.1 when only L_1 and L_2 are considered individually, and when both L_1 and L_2 are considered together (a) reflection magnitude (b) reflection phase.

incident normally at the bottom surface of L_1 . As shown in Fig. 8.1 (b), Γ_{SRM} is defined at the bottom surface of L_1 . To account for the distance between the feed point and the bottom surface of L_1 in practical ERAs (see Fig. 8.1 (a)), the waveguide port, which simulates the plane wave, is de-embedded to a distance of $-h_1$. Periodic boundary conditions (PBC) are applied to the lateral side walls of the SRM whereas perfectly matched layer (PML) is used for the top surface in $+z$ direction. The reflection characteristics ($|\Gamma_{SRM}|, \angle\Gamma_{SRM}$) of the superstructure, calculated numerically using transient-solver in CST Microwave Studio, are shown in Fig. 8.2 for a relatively large spectrum. The reflection magnitude $|\Gamma_{SRM}|$ for the two-layer superstructure has a maximum value of 0.91 at $f_0 = 12GHz$, and the reflection phase $\angle\Gamma_{SRM} = 183.19^\circ$. For the case of a single dielectric layer in the superstructure (only L_1), $|\Gamma_{SRM}|$ reaches a maximum of 0.64 near $f_0 = 12GHz$ and $\angle\Gamma_{SRM} = 182^\circ$. As expected, $\angle\Gamma_{SRM}$ exhibits a monotonic decrease like other conventional ERA superstructures in both cases.

8.3.2 Analytical Predictions

Analytical formulae based on the ray-tracing approximation have been developed in the past to predict the cavity height h_1 , and the enhancement in peak directivity D_p expected to be achieved by using a particular ERA superstructure [5, 36, 37]. The accuracy of these prediction models for finite superstructures composed of dielectric layers has not been studied in the past. In the last decade, these formulae were further developed to estimate the bandwidth of an ERA having a particular superstructure [5, 85]. The relative directivity enhancement predicted for a particular superstructure is given by

$$D_p(f_0) = \frac{|\Gamma_{SRM}(f_0)| + 1}{1 - |\Gamma_{SRM}(f_0)|} \quad (8.1)$$

which states that for an excitation source such as a slot or dipole, having a typical directivity of 6-7dBi, the directivity of an ERA having the superstructure in Fig. 8.1 (b) will be approximately 17.9-18.9 dB. However, the DBW for this ERA is expected to be nearly 3%, as given by

$$DBW = \frac{\Delta f_{3dB}}{f_0} = \frac{\lambda_0(1 - |\Gamma_{SRM}(f_0)|)}{2\pi h_1 \sqrt{|\Gamma_{SRM}(f_0)|}} \quad (8.2)$$

It is important to note that the ray-tracing approximation assumes the transverse extent of the antenna, i.e., in xy -plane (Fig. 8.1 (a)), to be infinite. In addition, eq. 8.2 does not take into account the reflection phase of the superstructure. In the proceeding sections, let us evaluate how well these analytical predictions hold for ERAs with finite superstructures, and identify the constraints within which this prediction model remains accurate.

8.4 Effects of Superstructure Finiteness

Maximum obtainable directivity by a particular ERA is a characteristic of the superstructure, as seen in Section 2 [5, 37, 89]. Within this limit, the peak directivity of a particular ERA also depends on its footprint. The relation of peak directivity with superstructure

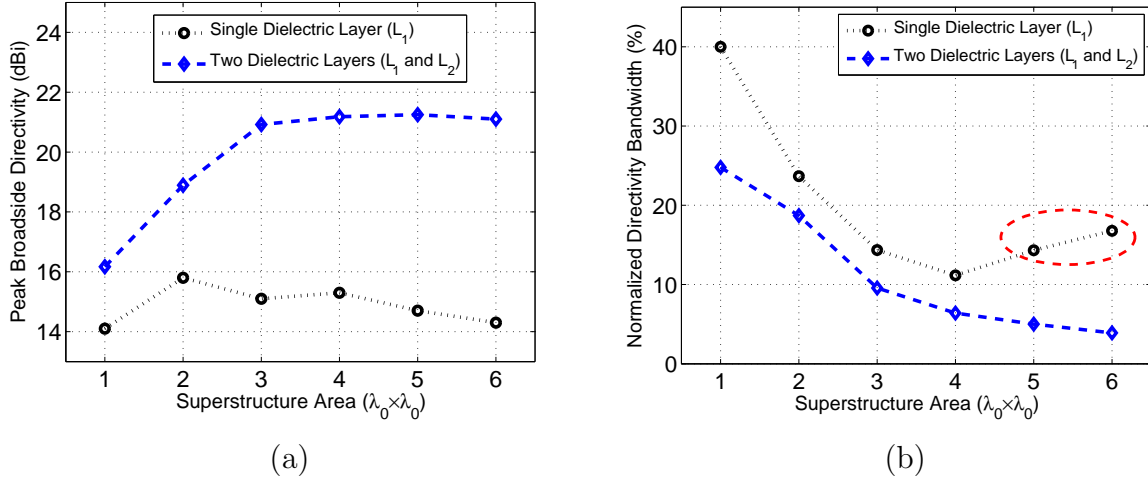


Figure 8.3: Comparing the variation in (a) peak directivity and (b) the directivity bandwidth with the change in footprint for a one- and two-layer superstructure (L_1 and L_2 are assumed to be made out of FR-4, $\epsilon_r = 4.3$).

footprint was studied in [8] through FDTD-simulations. It was found that the peak directivity shows a linear increase with ERA footprint when the footprints are increase from $6\lambda_0^2$ and $36\lambda_0^2$. Above this length, the peak directivity saturates and converges to a value below the maximum. Soon after, a similar trend was reported for a 3D EBG superstructure [7]. Thus in the past, to maximize peak directivity, most of the ERA prototypes were designed with large footprints often ranging between $20 - 36\lambda_0^2$. Moreover, the directivity and footprint of an ERA were assumed to follow an inverse relationship while the bandwidth often increases with a decrease in footprint. Now let us evaluate the possibility of designing ERAs that can provide maximum obtainable directivity with reduced footprints and improved bandwidths.

8.4.1 Equal Area of Superstructure Layers

Fig. 8.3 compares the peak directivity and the directivity bandwidth of an ERA in which the superstructure area is varied from $1\lambda_0^2$ to $36\lambda_0^2$. The results shown here are for two

cases: firstly, when only L_1 is considered in the superstructure, and secondly, with considering both L_1 and L_2 . For each case, the finite ERA was simulated using time domain solver in CST-MWS with PML boundaries in all directions. For all the ERAs, the length of ground planes was maintained $1\lambda_0$ larger than the length of the superstructure in both x - and y - directions. From Fig. 8.3 (a), it is evident that the directivity increases initially, and saturates after reaching a maximum for both the cases. With further increase in superstructure footprint, the peak directivity begins to decrease.

Note that the ERAs with two dielectric layers exhibit higher directivity than the ones with only a single layer. This increase is because of the high value of Γ_{SRM} for the superstructure with two dielectric layers than that of single dielectric layer (see Fig. 8.2 (a)). The bandwidth on the other hand, is found to decrease with the increase in superstructure footprint as shown in Fig. 8.3 (b). An increase in the bandwidth is observed for the ERAs having a single dielectric layer superstructure as the area is increased beyond $4\lambda_0 \times 4\lambda_0$. This apparent increase (marked by a solid ellipse in Fig. 8.3 (b)) is misleading because the corresponding ERAs ($5\text{--}6\lambda_0$ long) radiate conical beams (instead of pencil beams) over most of their 3dB bandwidth; thus, their actual operational bandwidth is quite narrow.

8.4.2 Unequal Area of Superstructure Layers

Following the results in Section 3.1, let us now study the effect of having each layer in the two-layer superstructure truncated individually. To do this systematically, the size of L_2 is varied from $1\lambda_0 \times 1\lambda_0$ to $6\lambda_0 \times 6\lambda_0$, for a fixed size of L_1 . During this process, finite ground planes are considered where the size of the ground plane in xy -plane is always $1\lambda_0$ larger than the size of L_1 or L_2 , whichever is larger. The rest of the parameters, such as t , h_1 , and ϵ_r , remain unchanged. The resulting variation of peak directivity and the directivity bandwidth is shown in Fig. 8.4 (a) and (b), respectively. The fixed sizes considered for L_1 are from $2\lambda_0 \times 2\lambda_0$ to $4\lambda_0 \times 4\lambda_0$, as the variation in the performance of

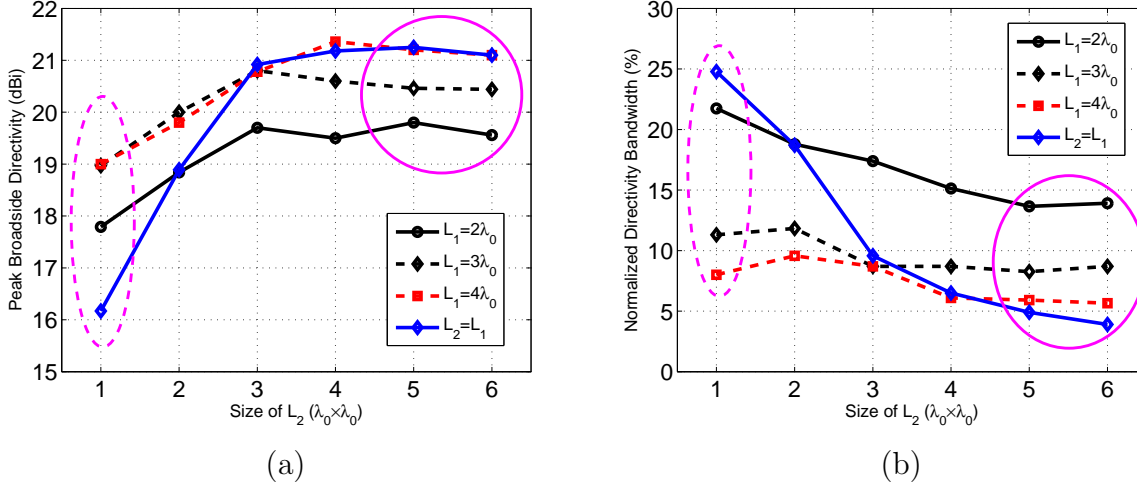


Figure 8.4: Variation in (a) peak directivity and (b) 3dB directivity bandwidth computed using the ERA model shown in Fig. 8.1 for various sizes of L_2 , whereas the size of L_1 was fixed to the values shown in the figure (antenna parameters used are: $h_1 = 12.5\text{mm}$, $h_2 = 6.25\text{mm}$, $t = \lambda_0/\sqrt{\epsilon_r}$ where $\epsilon_r = 4.3$ and $\lambda_0 = 25\text{mm}$).

ERAs was found to be significant within this range (see Fig. 8.3).

When the size of L_1 is fixed to $2\lambda_0 \times 2\lambda_0$, it is seen from Fig. 8.4 that the inverse relationship between peak directivity and directivity bandwidth can be relaxed to obtain reasonably high level of directivity alongside considerably wider bandwidths, compared to the case when superstructure layers are truncated equally (when $L_2 = L_1$). For instance, the case when the size of $L_1 = 2\lambda_0 \times 2\lambda_0$ and the size of $L_2 = 4\lambda_0 \times 4\lambda_0$, the DBW improves from 6.5% (when $L_2 = L_1$) to 15% whereas the peak directivity is decreased by only 1.6 dB, approximately. This effect is found to decrease for larger sizes of L_1 , although the general trend of deviation from the case when $L_2 = L_1$ prevails.

An interesting trend, seen in Fig. 8.4 (a), is the variation of peak directivity when $L_1 = 2\lambda_0$. Initially, when L_1 is larger than L_2 , the directivity is higher compared to the case when $L_1 = L_2$. Later on, when the size of L_2 is increased, whereas L_1 remains fixed to $2\lambda_0$, the directivity is lower compared to the case when $L_1 = L_2$. Another interesting result

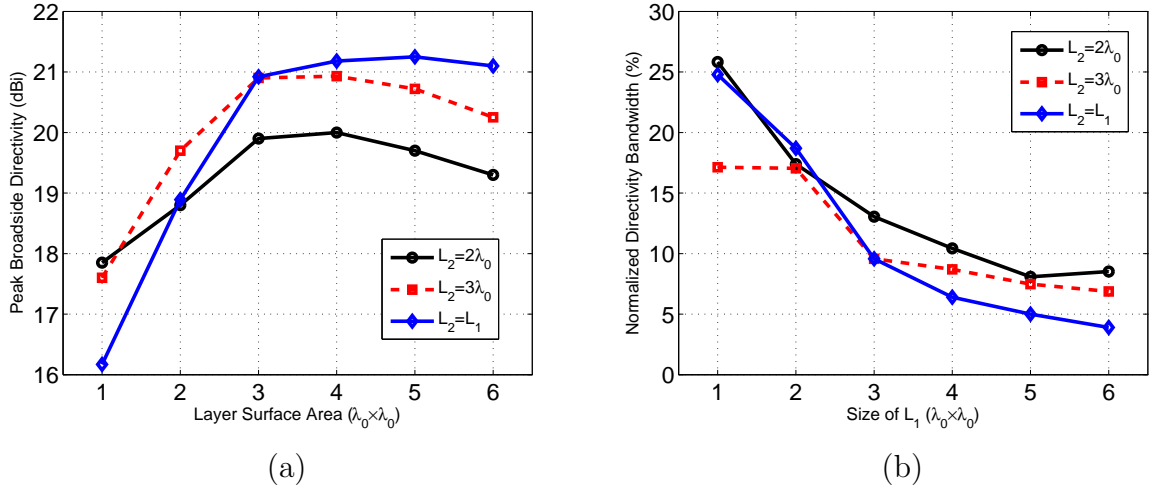


Figure 8.5: Variation in (a) peak directivity and (b) directivity bandwidth computed using the ERA model shown in Fig. 8.1 for various sizes of L_1 , whereas the size of L_2 was fixed to the values shown in the figure (antenna parameters used are: $h_1 = 12.5\text{mm}$, $h_2 = 6.25\text{mm}$, $t = \lambda_0/\sqrt{\epsilon_r}$ where $\epsilon_r = 4.3$ and $\lambda_0 = 25\text{mm}$).

is identified by the dotted ellipse in Fig. 8.4. Despite the small size of $L_2 = 1\lambda_0 \times 1\lambda_0$, the peak directivity increases as the size of L_1 increases, and the corresponding level of bandwidth decreases. This result is in accordance with the classical understanding associated with ERAs that the larger the aperture, the higher the peak directivity, and the lower the bandwidth. However, the results marked by a solid ellipse in Fig. 8.4 exhibit an enhancement in the directivity bandwidth despite the increase in the size of L_2 . This suggests that the size of L_1 has a dominant effect on the bandwidth of the resulting ERA. If L_1 has a small size, as is the case when $L_1 = 2\lambda_0$, significantly wider bandwidths can be obtained, even when the size of L_2 is as large as $6\lambda_0$. However, for larger sizes of L_1 , this effect diminishes and the bandwidths become narrow. This can be attributed to the classical behaviour where the fields reaching the edges of the cavity become weak and their diffraction causes little effect.

For completeness of analysis, a similar case study was conducted in a reciprocal manner

and the corresponding results are shown in Fig. 8.5. In this case, the size of L_1 is varied from $1\lambda_0 \times 1\lambda_0$ to $6\lambda_0 \times 6\lambda_0$, for fixed sizes of L_2 . The dimensions of the ground plane and the parameters t , h_1 , or ϵ_r , remain the same. It can be envisaged by observing the variation of directivity bandwidth in Fig. 8.5 that the effect of area of the first layer in the superstructure is more dominant. Instead, Fig. 8.5 (a) shows that when the L_2 has a greater footprint than L_1 , higher directivity is obtained compared to the vice versa. Thus, the best enhancement in ERA performance can be obtained when L_1 has a smaller relative footprint than L_2 . To consider the effect of permittivity in the superstrate, similar case studies were conducted with $\epsilon_r = 9.2$ (corresponding to commercial Rogers TMM10 material) and associated ERA parameters tuned accordingly. The general trends were found in agreement with the ones presented in this section but higher level of peak directivity was obtained, as expected.

8.5 Experimental Results

To experimentally validate the findings, three ERAs prototypes were manufactured. These prototypes had the same physical footprint, however the layers in the superstructure were truncated individually to different finite values. These prototypes are designated as ERA-I, ERA-II, and ERA-III as shown in Fig. 8.6 (a), (b), and (c), respectively. The waveguide-to-coax adaptor with 50Ω SMA transition used to feed the slot in these prototypes is also shown in Fig. 8.6 (d). Each dielectric layer has thickness $t = 2.94mm$ and is made out of Rogers TMM4 material ($\epsilon_r = 4.5, \tan\delta = 0.0023$). For ERA-I, both the superstructure layers have equal areas of approximately $4\lambda_0 \times 4\lambda_0$ whereas for ERA-II, the bottom layer is set to $3\lambda_0 \times 3\lambda_0$ and the top layer is set to $4\lambda_0 \times 4\lambda_0$. For ERA-III, the reciprocal configuration of superstructure in ERA-II is selected. The size of the ground plane for all three ERAs is the same i.e. $5\lambda_0 \times 5\lambda_0$, resulting in a physical

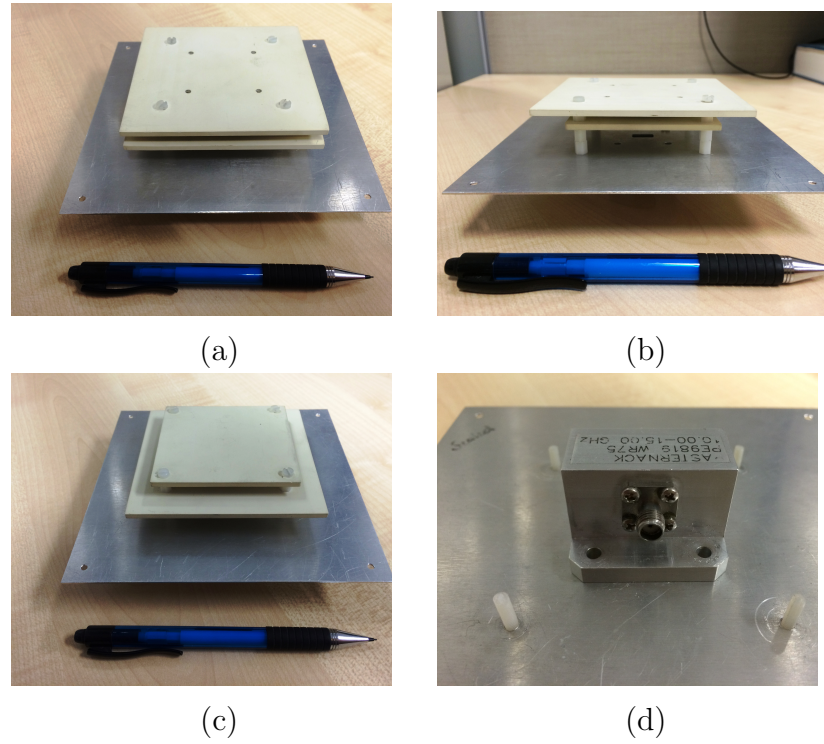


Figure 8.6: Prototypes for experimental validation (a) ERA-I (feed slot dimensions: $10.88\text{mm} \times 7.9\text{mm}$), (b) ERA-II (feed slot dimensions: $11.95\text{mm} \times 5.88\text{mm}$), (c) ERA-III (feed slot dimensions: $11.95\text{mm} \times 5.88\text{mm}$), and (d) Waveguide-to-coax adapter with SMA transition (WR75 grade).

area of $25\lambda_0^2$ where the area of the superstructure itself is $16\lambda_0^2$. The full-wave analyses and feed designs of these ERA prototypes were conducted in CST Microwave Studio (version 2014). Input reflection coefficients were measured by Agilent PNA-X N5242A vector network analyzer and the pattern measurements were carried out in NSI-700S-50 spherical near-field anechoic chamber at the Australian Antenna Measurement Facility (AusAMF).

Fig. 8.7 shows the measured input reflection coefficient for the three prototype ERAs. The impedance bandwidth (where $S_{11} < -10\text{dB}$) for ERA-I ranges from 11.5 GHz to 12.1 GHz. On the other hand, ERA-II and ERA-III demonstrate relatively wideband

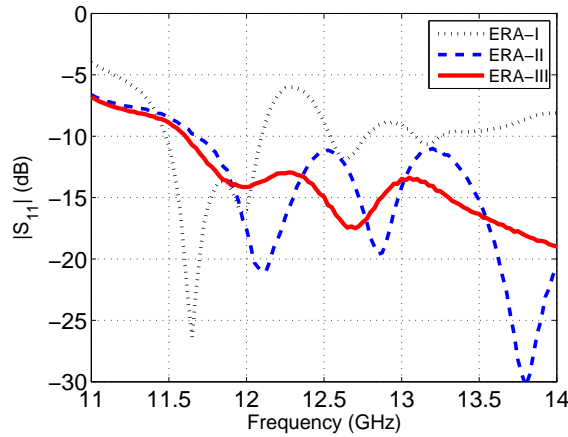


Figure 8.7: Measured reflection coefficient for the three ERA prototypes.

impedance matching extending from 11.75 GHz to beyond 14 GHz. These results demonstrate that the unequally-truncated superstructure layers improve the impedance bandwidth of the ERAs. This improvement can be attributed to reduced strength of waves that are reflected from the edges of the superstructure back towards the centre of the cavity. In the case of equal truncation (e.g. in ERA-I), the laterally propagating waves encounter only a single discontinuity at the perimeter of the superstructure. Whereas in the case of ERA-II and ERA-III, the discontinuity at the perimeter becomes progressive with two steps, thus, creating an improved match of the cavity to free space in the transverse plane.

The measured directivity and gain of the ERA prototypes is shown in Fig. 8.8 (a) and (b), respectively. ERA-I exhibits the highest peak directivity of 20.5 dBi alongside a directivity bandwidth of 3.3%. On the other hand, ERA-II demonstrates the widest directivity bandwidth of 7.01%, alongside a peak directivity of 19.5 dBi. It is worth noting that for 1dB reduction in gain, the bandwidth of the ERA nearly doubled, yet adhering to the same physical footprint. ERA-III also exhibits 65% more directivity bandwidth than ERA-I, however, the peak directivity is clipped at 18.7 dBi, i.e. 1.8dB less than ERA-I. The directivity bandwidths of each of these prototypes are well-complemented by their

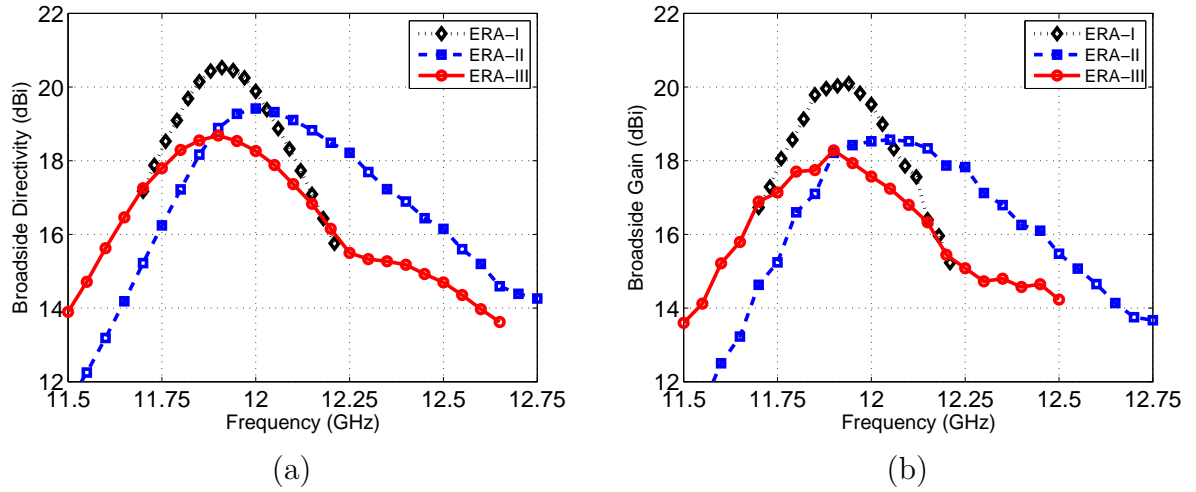


Figure 8.8: Measured broadside directivity and gain of the ERA prototypes.

respective impedance bandwidths, thus resulting in excellent antenna gain (see Fig. 8.8 (b)). Comparing the directivity and gain of the prototypes, one may notice slight variations. These variations can be attributed to structural tolerances such as the variation in the slot dimensions and the placement of spacers to hold the superstructure in place. Moreover, the well-known gain comparison method was employed for gain measurements which can introduce a variation of ± 0.5 dB. NSI-RF-SGH-75 reference horn antenna was used for the comparisons.

Radiation patterns recorded within the respective directivity bandwidths for each of the prototypes are depicted in Fig. 8.9, Fig. 8.10, and Fig. 8.11, respectively. In all cases, the narrow pencil beams are obtained with average sidelobe level below -15 dB. ERA-I exhibits excellent pattern quality with a faster roll off factor as compared to ERA-II and ERA-III. However, since it represents the classical narrowband case, it is limited by its narrow directivity bandwidth. On the other hand, ERA-II and ERA-III demonstrate good quality patterns but the former exhibits better sidelobe levels. In general, ERA-II demonstrates a reasonably good overall performance considering the peak directivity, the directivity bandwidth, and the pattern quality. Cross polarization performance was also

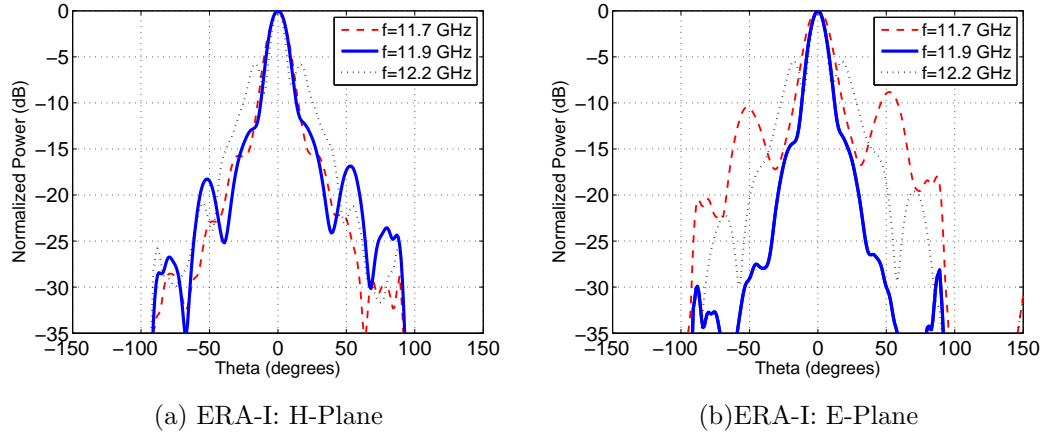


Figure 8.9: *E- and H-plane patterns of ERA-I within the 3dB bandwidth.*

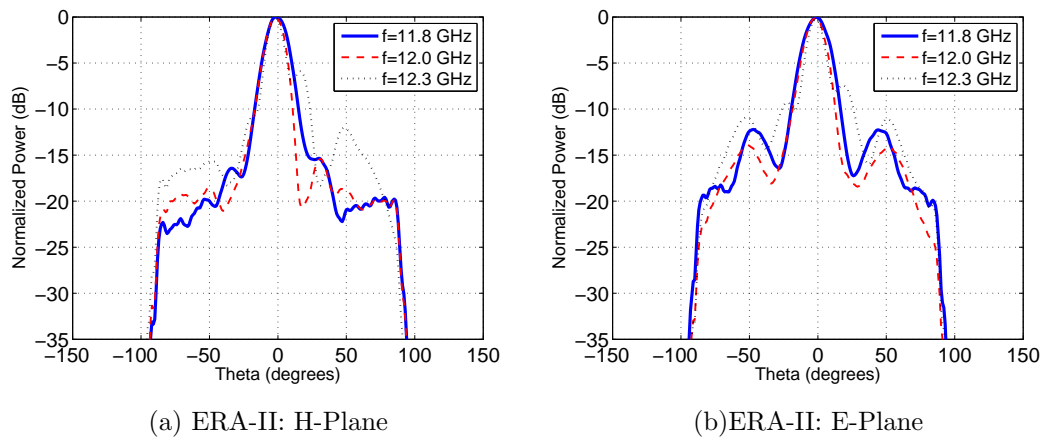


Figure 8.10: *E- and H-plane patterns of ERA-II within the 3dB bandwidth.*

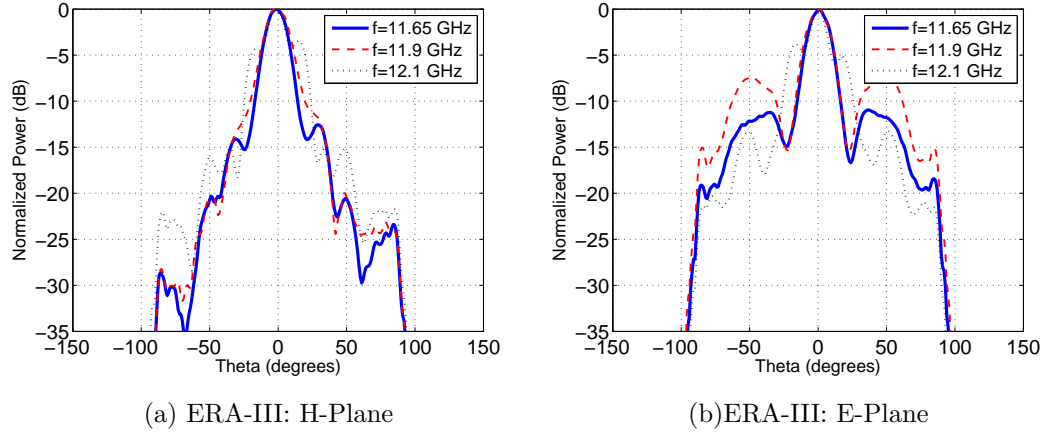


Figure 8.11: *E- and H-plane patterns of ERA-III within the 3dB bandwidth.*

Table 8.1: *Comparison of experimental data for the three prototype ERAs.*

	ERA-I	ERA-II	ERA-III
Size of L_1	$4\lambda_0 \times 4\lambda_0$	$3\lambda_0 \times 3\lambda_0$	$4\lambda_0 \times 4\lambda_0$
Size of L_2	$4\lambda_0 \times 4\lambda_0$	$4\lambda_0 \times 4\lambda_0$	$3\lambda_0 \times 3\lambda_0$
Peak Directivity	20.5 dBi	19.5 dBi	18.7 dBi
3dB Directivity Bandwidth	3.3%	7.01%	5.45%
Directivity-Bandwidth Product	370	625	404

measured for each of the prototypes and was found to be excellent. Average worst-case cross polarization levels recorded within the 3dB beamwidth for ERA-I, ERA-II, and ERA-III were -41dB , -37dB , and -42dB , respectively.

A reasonable figure of merit which has been used in the past to characterize ERAs is directivity-bandwidth product (DBP). The DBP calculated for each of the three prototypes is given in Table 8.1, along with key performance CH07/ch07/Figures. Table 8.1 shows that without any special treatment to the characteristics of the superstructure, the DBP of ERA-II and ERA-III demonstrate an increase of 69% and 9%, respectively. It is worth noting that this worthwhile increase is solely achieved by individually truncating the layers in the superstructure. Thus, such techniques can be combined with other

methods, such as superstrates with positive reflection phase gradients, or those with wide defect-modes, to obtain enhanced performance. Moreover, the predictions made in Section II regarding the directivity bandwidth and the peak directivity seem to hold for ERA-I, which represents the classical case. However, significant deviations from these predictions are observed in the case of ERA-II and ERA-III as the layers in the superstructure are assigned to unequal footprints. These deviations can be attributed to the fact that the prediction models used in Section II do not account for finiteness of the superstructure, and therefore, hold well if the following two conditions are satisfied:

1. The layers of the superstructure are truncated equally, which ensures that the reflection characteristics of the superstructure are uniform within the cavity at all points.
2. The footprint of the superstructure is large enough such that the field at the edges has decayed significantly before it undergoes diffraction and radiation.

8.6 Conclusion

The influence of finiteness in all-dielectric superstructure to enhance the performance of simple EBG resonator antennas (ERAs) was studied. It was found that even without any special treatment of the superstructure, its finiteness significantly affects the peak directivity and the directivity bandwidth of the ERAs. In particular, intriguing cases were observed when the dielectric layers in a two-layer superstructure were assigned to different finite sizes. Conventionally, although smaller superstructures yield wider bandwidths with reduced directivity, modifying the size of individual layers in the superstructure demonstrated more than 65% enhancement in the directivity-bandwidth product, without increasing overall area of the ERA, or that of the superstructure. Such methods are very attractive for improving the 3dB bandwidth as well as the directivity-bandwidth

product of existing ERAs without any significant modification to their design. Moreover, individual truncation of layers in multi-layer dielectric/metallo-dielectric superstructures can be used to improve the antenna characteristics, with practically minimal complexity.

Chapter 9

Effective Truncation of Superstructures in ERAs

9.1 Abstract

Electromagnetic Band Gap (EBG) resonator antennas (ERA), while offering design simplicity and high directivity, are promising candidates for microwave and millimeter wave communication links. Recommendations for effectively truncating the 1-D/2-D periodic structures, designed to act as superstructures in such antennas, are presented. It is shown that the aperture size in such antennas contributes, in part, towards the directivity-bandwidth product. A simple ERA, which uses a two layered 1-D EBG structure as its superstructure, is studied to quantify the effects of aperture size on peak directivity and half-power directivity-bandwidth. Conventional aperture size for such anten-

Published as: R.M. Hashmi, B.A. Zeb, K.P. Esselle, and S.G. Hay, "Effect of truncating the superstructures in broadband Fabry-Perot cavity antennas," *10th IEEE/MTT International Microwave and Optoelectronics Conference (IMOC)*, Rio de Janeiro, Brazil, 4-7 August, 2013.

nas ranges from $25\text{-}36\lambda_0^2$, that results in over-dimensioning as well as narrow-band behaviour. It is shown that comparable performance with existing designs can be achieved by using much smaller aperture sizes and thus reducing the antenna footprint. This work serves as a guide to effectively choose and fine-tune aperture sizes in ERAs, thus reducing the redundant computational load in the composite design process.

9.2 Introduction

High data-rate wireless communications require broadband and directive antennas for point-to-point and backhaul microwave and millimeter wave links. EBG resonator antennas (ERAs)¹, also known as Fabry-Perot cavity antennas, resonant cavity antennas, are promising candidates for such applications. These antennas can enhance the directivity of a single radiating source without the use of antenna arrays and associated complexity of feed networks [36, 37]. However, a major limitation of these antennas is their narrow half-power directivity bandwidth (HPDB: bandwidth where the directivity is 3dB less than the peak value) [5, 8]. Therefore, it is interesting to explore methods to enhance the HPDB of such antennas while preserving their design simplicity.

A common ERA consists of a Fabry-Perot resonant cavity formed between a conducting ground plane and a high reflectivity superstructure [8, 41, 125]. These superstructures can either be partially reflecting surfaces (PRS) with printed patterns, or EBG structures composed of unprinted dielectric slabs. The process to design ERAs consists of two phases: At first, the material for superstructure is designed through unit-cell optimization to achieve positive reflection phase or wide localized transmission [81]. In the second

¹The antennas in this manuscript have been re-named as EBG resonator antennas (ERAs) to maintain consistency with the work presented in this dissertation. However, the name “Fabry-Perot cavity antenna” was used in the original manuscript.

phase, the material is truncated to a finite value and applied as superstructure to form the ERA. The superstructure acts as an effective aperture for the ERA resulting in directivity enhancement of the feed source, whereas the truncation value of the superstructure affects the HPDB. The dimensions of conventional superstructures are $5\lambda_0 \times 5\lambda_0$ to $6\lambda_0 \times 6\lambda_0$, which make a cavity with very high value of Q-factor and thus, a narrow-band antenna.

In this paper, we demonstrate the possibility of using smaller apertures to achieve much wider bandwidth performance compared to existing designs in terms of HPDB with comparable peak directivity. We develop recommendations for effectively truncating the superstructure of ERAs by quantifying the effect of aperture size on their far-field performance. In Section II, we describe the relationship between aperture size of a ERA and its HPDB while in Section III, we present the details of full-wave analysis for this study. In Section IV, we present and discuss the simulation results obtained by using CST-Microwave Studio, comparing them with some of the top notch designs proposed for wideband ERAs. Section V concludes the paper.

9.3 Aperture Size and Directivity-Bandwidth

The designs of ERAs are largely based on unit-cell analysis of the superstructure, which is computationally much less expensive compared to full scale ERA design with a finite superstructure and feed source. However, unit-cell analysis is based on periodic boundary conditions (PBC) and uniform plane wave incidence. Although, the transmission and/or reflection profiles computed through unit-cell models [81] are appropriate, they do not take into account finiteness effects like edge diffraction, effect of having a single source in the cavity instead of a uniform plane wave, and the aperture efficiency of the ERA. It is possible to quantify these effects; however, the only way of doing so is through full-scale analysis. Since full-scale ERA design is computationally and temporally extensive

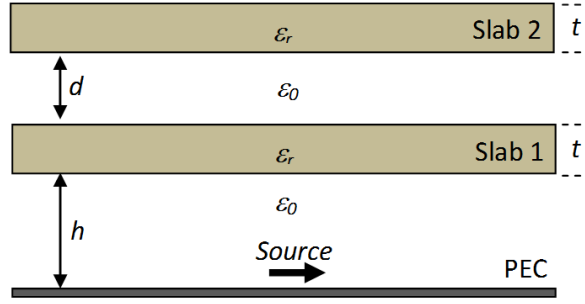


Figure 9.1: Basic ERA with an EBG superstructure composed of dual dielectric slabs with equal permittivity ($\epsilon_r = 9.2$) and thickness ($t = \lambda_g/4$) at $f_0 = 11.5$ GHz.

compared to unit-cell analysis, the designers usually assume conventional value of $5\lambda_0 \times 5\lambda_0$ to $6\lambda_0 \times 6\lambda_0$ for truncating ERA superstructures, followed by limited fine-tuning. Although this choice is governed by the goal of maximizing the peak directivity, it is not independent of HPDB of a ERA.

Basic ERA with an EBG superstructure composed of dual dielectric slabs with equal permittivity ($\epsilon_r = 9.2$) and thickness ($t = \lambda_g/4$) at $f_0 = 11.5$ GHz. Peak directivity for a ERA as a function of aperture size was computed in [8] suggesting that the increase in the level of peak directivity saturates after the aperture size increases above $6\lambda_0 \times 6\lambda_0$. This occurs because an over dimensioned aperture results in a high Q-factor cavity which confines most of the energy in its centre and thus results in a highly directive beam according to the following relationship derived in [42]

$$Q_0 = \frac{1}{2(1 - \cos(\theta_{HPBW}/2))} \quad (9.1)$$

where θ_{HPBW} is the half-power beam-width of the ERA at f_0 , the selected frequency. However, the overall aperture efficiency becomes very low and so does the HPDB.

Recent efforts to increase the HPDB of ERAs include the use of multi-layer dielectric superstructures with multiple sources of excitation to achieve effective illumination of the aperture through a microstrip coupled slot array [10], partially reflecting surfaces (PRS)

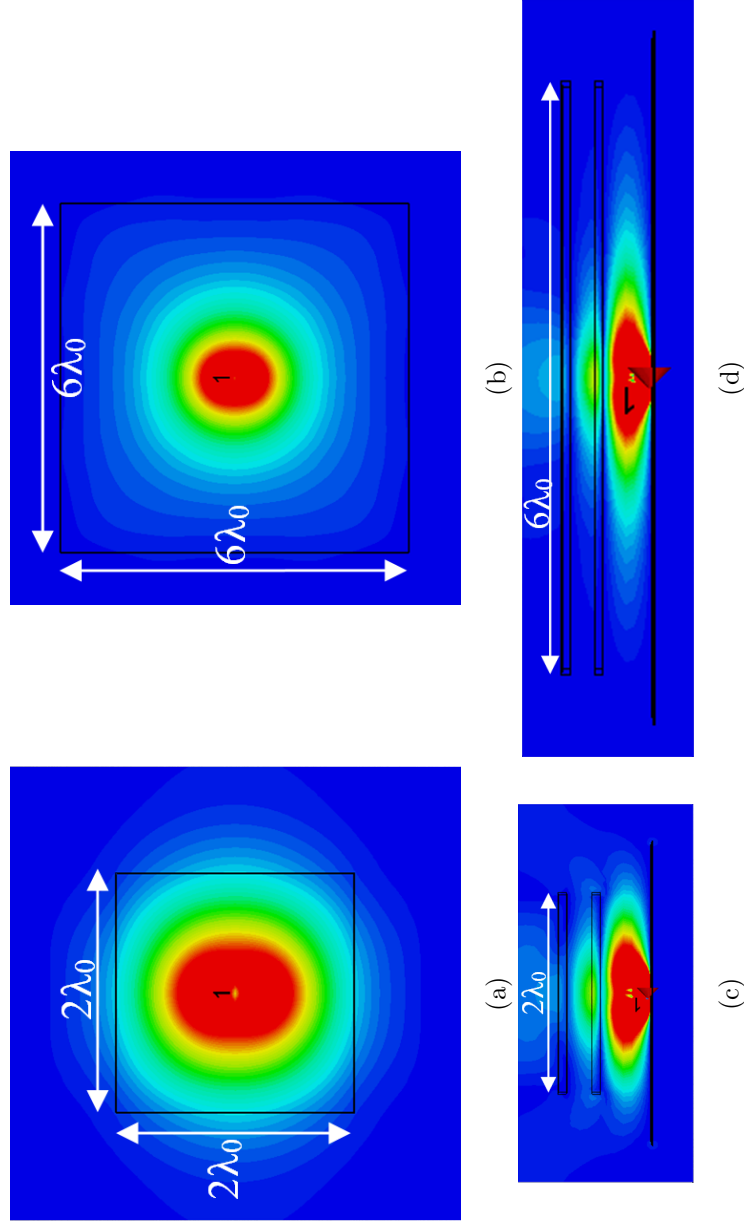


Figure 9.2: Fig. 2. *E*-field shown for horizontal and vertical cuts for the ERA shown in Fig. 9.1 for two aperture sizes at $f_0 = 11.5\text{GHz}$ (a) Top view for aperture size $2\lambda_0 \times 2\lambda_0$ (b) Top View for $6\lambda_0 \times 6\lambda_0$ (c) vertical cross section for $2\lambda_0 \times 2\lambda_0$ (d) vertical cross section for $6\lambda_0 \times 6\lambda_0$.

with tapered periodic patterns [11] and PRS composed of multiple elements with closely spaced resonant frequencies [12]. These designs are largely based on engineering the reflection phase gradient of the superstructure; however, positive reflection phase is not the only contributor towards enhancing HPDB. In part, decreasing the aperture size and thus, increasing aperture efficiency can result in widening the HPDB of ERAs. In past, the use of multiple sources to feed the cavity has been found to increase the directivity bandwidth by uniform illumination of the cavity and thus, increased aperture efficiency. This work aims to establish the basis of using smaller apertures in widening the HPDB along with highlighting the trade-offs associated with the process.

9.4 Full-Wave Analyses

In order to study the characteristics outlined in Section II, related to full-scale ERA design, we study a very simple ERA configuration which is shown in Fig. 9.1 using full-wave analysis in CST Microwave Studio. The ERA has an EBG superstructure which consists of two unprinted dielectric slabs with thickness $t = \lambda_g/4$ and $\epsilon_r = 9.2$. The slabs are placed at height $h = \lambda_0/2$ above the ground plane and the separation between the slabs is $d = \lambda_0/4$. A horizontal electric dipole (HED) is used as the primary feeding source and is placed 0.8mm above the metallic ground plane in the centre of the primary cavity. For this design, the lateral dimensions of the superstructure are varied equally from $1\lambda_0 \times 1\lambda_0$ to $6\lambda_0 \times 6\lambda_0$, and peak directivity, sidelobe levels and HPBW were computed. Moreover, the intensity of E-field in the primary cavity (between the ground plane and the first slab) was also computed. Fig. 9.2 (a) and (b) show the plots of tangential E-field distribution for aperture sizes $2\lambda_0 \times 2\lambda_0$ and $6\lambda_0 \times 6\lambda_0$. The plots reveal that the smaller aperture is much well illuminated compared to the larger one, when a single source is used for feeding the cavity. On the other hand, the vertical cross-section in Fig. 9.2 (c) and

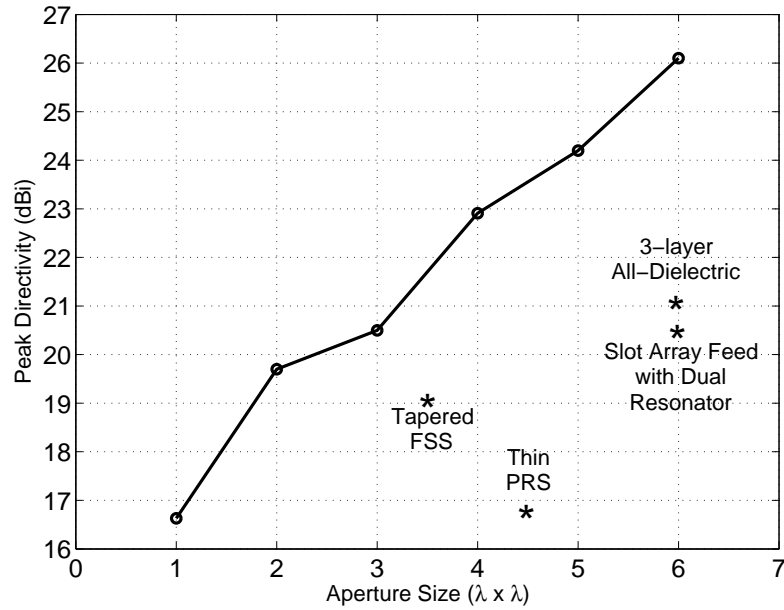


Figure 9.3: Peak directivity of ERA for various aperture sizes of the EBG superstructure. Peak directivity of some designs proposed for HPDB enhancement are also plotted for comparison.

(d), for $2\lambda_0 \times 2\lambda_0$ and $6\lambda_0 \times 6\lambda_0$, respectively, show that the cavity with larger aperture has most of the energy confined in the centre. According to 9.1, the larger cavity has Q-factor $Q_{6\lambda_0 \times 6\lambda_0} = 108.6$, while the smaller cavity has $Q_{2\lambda_0 \times 2\lambda_0} = 32.9$. Therefore, a compromise between the level of peak directivity and HPDB can be obtained depending on the requirements of the design.

9.5 Results and Discussion

To quantify the effect of aperture size on ERA far-field performance during the full-scale design phase, peak directivity, HPDB and side lobe levels were computed for EBG superstructure of the ERA in Fig. 9.1 with lateral dimensions varied from $1\lambda_0 \times 1\lambda_0$ to $6\lambda_0 \times 6\lambda_0$. Above $6\lambda_0 \times 6\lambda_0$, the results were found consistent with those of [8] with the

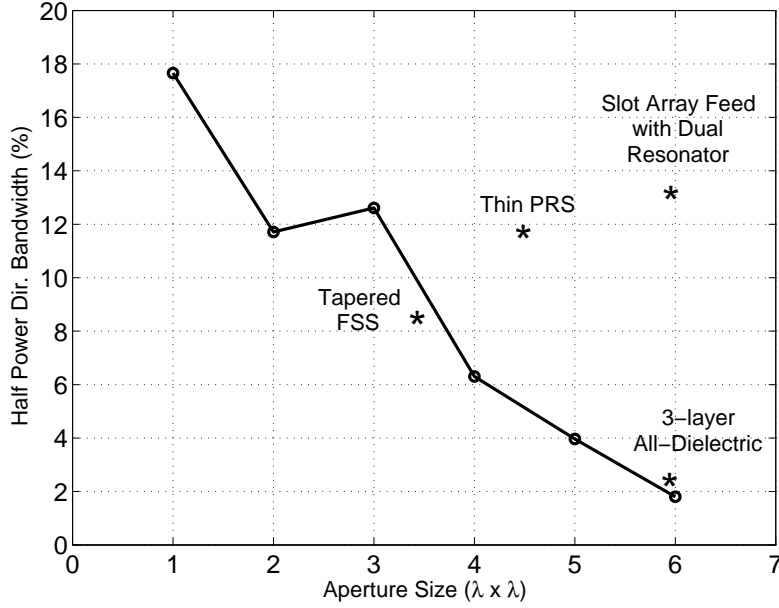


Figure 9.4: *Fig. 4. Computed HPDB of ERA for various aperture sizes of EBG superstructure compared to some key designs proposed for bandwidth enhancement. Note the consistency between results of ERA in Fig. 9.1 and 3 layer all-dielectric ERA when the superstructure size is $6\lambda_0 \times 6\lambda_0$.*

level of peak directivity saturating after 26dBi. Fig. 9.3 shows the level of computed peak directivity for various aperture sizes of the EBG superstructure. The peak directivity of some designs proposed for HPDB enhancement are also plotted for comparison in Fig. 9.3 which include the dual resonator with slot array feed [10], the tapered FSS [11], the printed thin PRS [12], as well as the three layered all-dielectric ERA proposed in [8]. Since the EBG superstructure employed in our study uses high permittivity slabs of Rogers TMM10 ($\epsilon_r = 9.2, \tan\delta = 0.002$), the level of peak directivity obtained is about 4 dB higher than that in [8], which employed Rogers TMM4 slabs ($\epsilon_r = 4.5, \tan\delta = 0.002$). Similar explanation follows for the tapered FSS and the thin PRS which use low permittivity printed superstructures and reach a maximum of 19dBi and 16.5dBi respectively. However, compared to the dual resonator with slot array feed, the peak

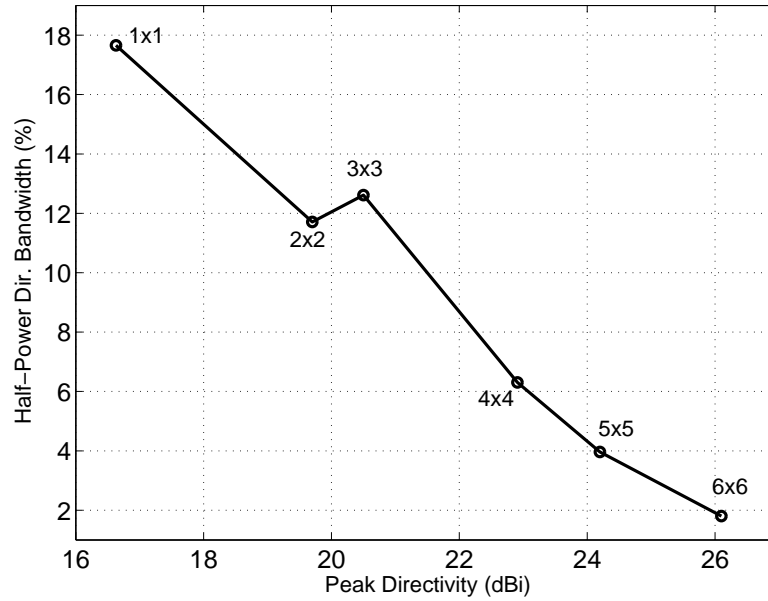


Figure 9.5: *Percentage HPDB versus peak directivity, computed for the ERA shown in Fig. 1.*

directivity for our simple ERA is much higher given the fact that the former uses a 4x8 microstrip coupled slot array as the feed while the latter uses only a single feed. Reflectivity is the governing factor for directivity enhancement and is largely dependent on the permittivity of the material employed for the superstructure. Therefore, it is possible, as seen in Fig. 9.3, that comparable peak directivity can be achieved by the proposed designs if the superstructures can be truncated to a smaller value compared to the existing over-dimensioned sizes. In particular, for the case of slot array feed, comparable directivity performance can be obtained with an aperture that is 50% smaller than its current size. This naturally results in lesser feeding sources and reduced ohmic losses due to removal of the feeding network.

The HPDB values computed for various aperture sizes are plotted in Fig. 9.4 and compared with the above mentioned proposed designs. The trend reinforces the idea presented above that with the superstructures of these designs truncated to a smaller

value, comparable level of directivity with a wider HPDB can be achieved. In this case, the HPDB of the 'three layered all-dielectric ERA' is consistent with our result as the HPDB reaches a minimum value around 2% at $6\lambda_0 \times 6\lambda_0$. The HPDB of the dual resonator with array feed configuration is quite high which is attributed to high aperture efficiency caused by multiple radiating slots. Following this trend, it is predicted that the HPDB be increased for tapered FSS and thin PRS designs by increasing their aperture efficiency which can easily be achieved by reducing the FSS/PRS dimensions.

Although exceedingly wide HPDB can be achieved for apertures as small as $1\lambda_0 \times 1\lambda_0$, sidelobe levels are observed to rise as high as -8dB for aperture sizes below $1.5\lambda_0 \times 1.5\lambda_0$. Significant reduction of footprint can be achieved by the use of smaller apertures despite the enhancement in HPDB, which rules out another major limitation of the ERAs in terms of excessive lateral size. It must be noted that since effective aperture truncation serves as a method to enhance HPDB, in addition to engineering the unit-cell transmission/reflection profiles, the peak values in Fig. 9.4 do not serve as an upper bound for bandwidth enhancement. The peak HPBW can further be improved by combining a superstructure with well engineered positive reflection phase or wide localized transmission, with an effectively truncated aperture.

Fig. 9.5 shows the tradeoff relationship between HPDB and peak directivity for the ERAs, however, with a generalized view with various aperture sizes. It is emphasized that the two phases of ERA design i.e. unit-cell optimization and full-scale modeling, contribute in part towards its final performance and should be carried out in unison. Nevertheless, since the latter can be less efficient computationally, the results presented in this paper can be used to make an educated initial guess towards fine tuning the full-scale design based on the specifications for peak directivity and HPDB being sought. The harmonized use of these design phases can effectively ensure consistent side lobe levels over the entire HPDB as well.

9.6 Conclusion

A novel perspective relating to the design of Fabry-Perot cavity antennas was presented. The importance of full-scale design while highlighting the factors which are overlooked in the conventional design process of ERA is established. The numerical results presented in the paper are generalized to serve as guidelines for ERA design and full scale modeling. The relation of aperture size of ERA superstructure with its half-power directivity bandwidth is introduced. It is shown that significant improvements in half-power directivity bandwidth as well as reduction of footprint can be achieved by effectively truncating the size of ERA superstructures to smaller values, depending on the design specifications being sought.

Chapter 10

Conclusions and Future Work

10.1 Conclusions

This dissertation presented research on bandwidth enhancement of electromagnetic band gap (EBG) resonator antennas (ERAs). Several novel designs were proposed and investigated to achieve high directivity over wide bandwidths, with single feed ERAs. Novel wideband ERAs were designed by utilizing wide defect-mode superstructures produced by multiple, unprinted dielectric slabs having axial permittivity gradients (APGs). The APGs resulted from different permittivity and thickness values of the dielectric slabs. It was found that, provided the reflection from the superstructure ($|\Gamma_{SRM}|$) is strong enough, the defect-mode bandwidth approximately predicts the 3dB directivity bandwidth of finite ERAs with medium superstructures ($\approx 9 - 16\lambda_0^2$). Thus when designing wideband ERAs, increasing the defect mode bandwidth using a unit cell is a reasonable start. However, the ERA directivity bandwidth can be further enhanced significantly by truncating these wideband superstructures to have smaller areas (e.g., $2.25 - 4\lambda_0^2$). It was also shown using defect-cavity analysis how self-resonances within a superstructure limit the 3dB bandwidth of an ERA and an alternative approach was presented to overcome this limi-

tation. Experimental results demonstrated 18.2 dBi peak gain and an excellent 3dB gain bandwidth of 21.7%, which is a significant increase over 3-4% bandwidth of classical 1-D ERAs having a single feed. It is worth noting that this wideband performance is achieved by using a single feed and unprinted dielectric slabs, thus avoiding the need for expensive feeding networks and/or complex to design printed superstrates. These antennas were well matched over the operating bandwidth ($VSWR < 1.6$). To the best of our knowledge, no other planar antenna with an area as small as $2.25\lambda_0^2$ has a measured gain over 15 dBi with a measured bandwidth over 20%. It is interesting to note that though the profile of these ERAs is comparable to classical two layer designs, their overall volume is much smaller, making them highly compact.

In addition to APGs, the use of planar, all-dielectric superstrates with transverse permittivity gradients (TPG) to design extremely wideband ERAs were investigated. It was found that the 3dB directivity bandwidth can be increased to as wide as 50% by using appropriately designed single-slab superstrates with TPG. The use of TPG superstrates tremendously enhanced the directivity-bandwidth product (DBP) as well, while providing a sufficiently high level of antenna gain. A measured directivity bandwidth of 52.9% was demonstrated by one of the prototype ERAs designed using this procedure, alongside a peak directivity of 16.4 dBi. To the best of the author's knowledge, no other ERA has such a large directivity bandwidth (52.9%), gain bandwidth (54.2%), directivity-bandwidth product (2,309), or gain-bandwidth product (2,109). It was shown that the directivity-bandwidth product can be further increased beyond 3,000 using thicker TPG superstrates. The total footprint area of the prototype antenna was only $1.54\lambda_0^2$ at the lowest operating frequency of 10 GHz. A relationship between broadband directivity enhancement of TPG superstrates and their aperture-field phase uniformity was established to provide valuable insight into the underlying principle of operation. It was found that superstrates with transverse permittivity gradients (TPGs) lead to ERAs with better performance and less

height than those with the APGs. However, the side lobe levels (SLL) of ERAs with APGs were found to be lower than the ERAs with TPGs. The ERAs proposed in this dissertation can provide significantly higher “DBP per unit area” compared to alternatives such as lens/flat-lens antennas and reflector antennas. This interesting characteristic makes these ERAs very suitable for space-critical applications where high directivity is required in a small physical area, and simplicity of approach is of essence.

While designing these wideband ERAs, the finiteness of the ERA superstructures was found to be a vital contributor to the DBP as well as the overall antenna performance. The importance of full-wave composite antenna design was studied while highlighting the factors which are overlooked by the analytical ray-tracing model as well as the unit-cell models. These effects were systematically quantified through detailed case studies that were conducted using full-wave analysis of a single layer as well as a two-layer dielectric superstructure with uniform permittivity in single-feed ERAs. It was found that even without any special treatment of the superstructure, the finiteness of the superstructure had a strongly influenced the DBPs. In particular, intriguing cases were observed when the dielectric layers in the two-layer superstructure were truncated to different finite sizes. Despite that the smaller superstructures yield wider bandwidths with reduced peak directivity, the truncation of superstructure layers to different finite sizes allowed for more than 65% enhancement in the DBP while resorting to the same physical footprint. Three ERAs were selected for experimental studies which validated this concept. The detailed empirical relationships between the peak directivity, bandwidth, and the finiteness of the superstructure layers provided valuable physical insights into the operation of superstructures that have non-uniform reflection and transmission profiles, similar to the TPG or APG superstructures.

All the ERAs proposed in this dissertation demonstrated very high efficiencies (mostly average $\eta_{rad} > 90\%$) within their operating bandwidths. It was found that these wideband

ERAs can be used in array configurations to achieve significantly increased antenna gains ($\approx 21\text{dBi}$) over very wide bandwidths ($25 - 35\%$), with only four elements, as opposed to conventional arrays that require several low-directivity sources. The simple configuration of these ERAs makes them highly suitable for directive point-to-point applications, specially in urban areas, considering their aesthetic appeal (small footprint and low profile). Moreover, owing to the symmetrical superstructures, these antennas can be extended to support dual-linear polarization as well as circular polarization over a wide band, just by appropriately modifying the feed antenna.

10.2 Future Work

In future the following aspects of ERAs can be considered for further research and developments:

- Extension of the proposed ERAs at millimeter wave frequencies can be explored for applications in V-band (50-75 GHz) and F-band (90-140 GHz). With such wide bandwidths, ERAs can be used to cover these entire bands and act as switched-beam high gain antennas for terrestrial communications, automotive radar applications, and as reflector feeds for radio astronomical radio-telescopes.
- The proposed designs are polarization versatile and can support linear, dual-linear (DL), and circular polarization (CP). Extensions of the proposed designs to support DL or CP can be a promising direction of research.
- Wideband CP ERAs can prove to be invaluable in various defense and commercial applications. In order to extend the proposed designs to support CP, one of these two options can be pursued: either novel wideband feeds can be designed that are able to provide required axial-ratio performance within the directivity bandwidth

of the ERA; or polarization converter frequency selective surfaces having wideband performance can be used to convert the linearly polarized radiation of the feed antennas to CP.

- At present, the theoretical models used to study ERAs do not take into account superstructure finiteness. Analytical modelling of superstructure finiteness is a future research topic which may be based on quantifying the field diffracted from the edges of the superstructure.
- Evolutionary optimization techniques such as particle swarm optimization or genetic algorithms can be customized for global optimization of the ERAs proposed in this dissertation.
- The design of simple feed antennas that can function as feed for ERAs with wide bandwidths can be a possible future research direction. Common feed antennas like reactively loaded patch antennas and monopoles do not perform well within the ERA cavities. In addition, the waveguide to coaxial transitions employed to feed the proposed ERAs are limited to their designated bands, such as X- or Ku- bands, for which they have originally been designed. These transitions are unable to provide a good match beyond their designated bands and limit the effective gain-bandwidth of the ERAs.
- Optimization of the transverse permittivity gradient (TPG) superstrates can be explored with the objective of achieving certain radiation pattern envelope (RPE) requirements. RPE requirements can be met by adding various degrees of freedom to the TPG superstrates.
- The use of matching layers above the TPG superstrate to improve the VSWR of the ERAs can be explored.

- The empirical data highlighting the relationship between the peak directivity, bandwidth, and the finiteness of the superstructure layers can be used to develop a quantitative analytical model for predicting the performance of ERAs with multi-layer all-dielectric superstructures.
- Small footprint wideband ERAs can be arranged in array configurations. Such arrays can provide low cost, planar means of achieving high aperture efficiency and high directivity over wide bandwidths with a comparatively small number of elements.

Appendix A

Research Outcomes

A.1 Patent Applications

The following are the patent applications which resulted from part of research undertaken during the author's candidature.

1. International (PCT) patent application PCT/AU2015/000354. **Title:** Wideband high-gain resonant cavity antenna. **Inventors:** K.P. Esselle, R.M. Hashmi, date of filling: 17 June 2015.
2. Australian provisional patent application (AU)2014902326. **Title:** Wideband high-gain resonant cavity antenna. **Inventors:** K.P. Esselle, R.M. Hashmi, date of filling: 18 June 2014.

A.2 List of Publications

Following are the lists of peer-reviewed research papers published, accepted or in review, based on the research undertaken during the author's candidature.

A.2.1 Journal Articles

1. R.M. Hashmi, B.A. Zeb, and K.P. Esselle, “Wideband high-gain EBG resonator antennas with a small footprints and all-dielectric superstructures,” *IEEE Transactions on Antennas and Propagation*, vol. 62, No. 6, pp. 2970-2977, 2014.
2. R.M. Hashmi, and K.P. Esselle, “A wideband EBG resonator antenna with an extremely small area,” *Microwave and Optical Technology Letters*, vol. 57, No. 7, pp. 1531-1535, 2015.
3. B.A. Zeb, R.M. Hashmi, and K.P. Esselle, “Wideband gain enhancement of a slot antenna using one unprinted dielectric superstrate,” *Electronics Letters, IET*, vol. 51, No. 15, pp. 1146-1148, 2015.
4. R.M. Hashmi, and K.P. Esselle, “A class of extremely wideband resonant cavity antennas with large directivity-bandwidth products,” *IEEE Transactions on Antennas and Propagation*, accepted in December 2015 (*in press*).
5. R.M. Hashmi, and K.P. Esselle, “Enhancing performance of EBG resonator antennas by individually truncating superstructure layers,” *Microwaves, Antennas & Propagation, IET*, 2015, *in review*.

A.2.2 Invited Articles

1. R.M. Hashmi and K.P. Esselle, “Arrays of high aperture efficiency wideband EBG resonator antennas,” *International Conference on Electromagnetics in Advanced Applications (ICEAA)*, Turin, September, 2015.
2. R.M. Hashmi, B.A. Zeb, K.P. Esselle, and S.G. Hay, “EBG resonator antennas with high aperture efficiencies,” *International Conference on Electromagnetics in Advanced Applications (ICEAA)*, Palm Beach, Aruba, August, 2014.

3. R.M. Hashmi, B.A. Zeb and K.P. Esselle, “Effective techniques for extending the directivity-bandwidth of resonant cavity antennas,” *IEEE International Workshop on Antenna Technology (iWAT)*, Sydney, NSW, Australia, March, 2014.
4. B.A. Zeb, R.M. Hashmi, K.P. Esselle, and Y. Ge, “The use of reflection and transmission models to design wideband and dual-band Fabry-Perot cavity antennas,” *URSI International Symposium on Electromagnetic Theory (EMTS)*, pp. 1084-1087, Hiroshima, Japan, May, 2013.

A.2.3 Conference Articles

1. R.M. Hashmi, B.A. Zeb, and K.P. Esselle, “Composite defect-mode superstructures and wideband EBG resonator antennas,” *European Conference on Antennas and Propagation (EuCAP)*, Lisbon, Portugal, April, 2015.
2. R.M. Hashmi, K.P. Esselle, and S.G. Hay, “Wideband flat-gain performance with electromagnetic band gap (EBG) resonator antennas,” *Fourteenth Australian Symposium on Antennas (ASA)*, Sydney, NSW, Australia, February, 2015.
3. B.A. Zeb, R.M. Hashmi, and K.P. Esselle, “Computational models for bandwidth enhancement of electromagnetic bandgap (EBG) resonator antennas and their limitations,” *IEEE International Conference on Computational Electromagnetics (ICCEM)*, pp.19-21, Hong Kong, SAR, February, 2015.
4. R.M. Hashmi, K.P. Esselle, and S.G. Hay, “Directive beaming with lens-like superstrates for low profile Fabry-Perot cavity antennas,” *International Symposium on Antenna Technology and Applied Electromagnetics (ANTEM)*, Victoria, BC, Canada, July, 2014.
5. R.M. Hashmi, K.P. Esselle, and S.G. Hay, “Achieving high gain-bandwidth through

- flat GRIN superstrates in Fabry-Perot cavity antennas,” *IEEE International Symposium on Antennas and Propagation (AP-S)*, Memphis, TN, U.S.A., July, 2014.
6. R.M. Hashmi, B.A. Zeb, K.P. Esselle, and S.G. Hay, “A simple resonant cavity antenna with improved directivity-bandwidth performance for high-capacity wireless data links,” *IEEE International Conference on Applied Electromagnetics and Communications (ICECom)*, Dubrovnik, Croatia, October, 2013.
 7. R.M. Hashmi, B.A. Zeb, K.P. Esselle, and S.G. Hay, “Effect of truncating the superstructures in broadband Fabry-Perot cavity antennas,” *IEEE/MTT International Microwave and Optoelectronics Conference (IMOC)*, Rio de Janeiro, Brazil, August, 2013.
 8. R.M. Hashmi, B.A. Zeb, and K.P. Esselle, “Wideband high-gain EBG resonator antenna employing an unprinted composite superstrate,” *IEEE International Symposium on Antennas and Propagation (AP-S)*, pp. 278-279, Orlando, FL, U.S.A., July, 2013.
 9. R.M. Hashmi, K.P. Esselle, and S.G. Hay, “Engineering defect-modes in unprinted EBG structures to design high-gain broadband antennas,” *Thirteenth Australian Symposium on Antennas (ASA)*, Sydney, NSW, Australia, February, 2013.

Appendix B

List of Acronyms

1-D, 2-D or 3-D	One-, Two-, or Three-Dimensional
ACMA	Australian Communications and Media Authority
AMC	Artificial Magnetic Conductor
APG	Axial Permittivity Gradient
ARC	Australian Research Council
AusAMF	Australian Antenna Measurement Facility
BAEP	Bandwidth Aperture Efficiency Product
CSIRO	Commonwealth Science and Industrial Research Organization
CSS	Composite Superstructure
CST	Computer Simulation Technology
CST-MWS	CST Microwave Studio
DBP	Directivity Bandwidth Product
DBP/A	Directivity Bandwidth Product per unit Area
DCM	Defect Cavity Model
DMB	Defect-Mode Bandwidth
EBG	Electromagnetic Band Gap
ERA	EBG Resonator Antenna
FAFR	Focal Array-Fed Reflector
FDTD	Finite Difference Time Domain
FEM	Finite-Element Method
FPC	Fabry-Perot Cavity
FPCA	Fabry-Perot Cavity Antenna
FSS	Frequency Selective Surface

HED	Horizontal Electric Dipole
HPDB	Half-Power Directivity Bandwidth
HPBW	Half-Power Directivity Beamwidth
LA	Lens Antenna
LMDS	Local Multi-point Distribution Systems
LWA	Leaky-wave Antenna
NBN	National Broadband Network
PBC	Periodic Boundary Condition
PML	Perfectly Matched Layer
PRS	Partially Reflecting Surface
RCA	Resonant Cavity Antenna
SGH	Standard Gain Horn
SLL	Sidelobe Level
SMA	SubMiniature Version A
SRM	Superstructure Reflection Model
STPG	Superstrate with Transverse Permittivity Gradient
TLM	Transmission Line Model
TMM	Thermoset Microwave Material
TPG	Transverse Permittivity Gradient
VSWR	Voltage Standing Wave Ratio
WLANs	Wireless Local Area Networks

Bibliography

- [1] Kymeta Corporation. (2012) Kymeta demonstrates ka-band satellite link. [Online]. Available: <http://www.kymetacorp.com/kymeta-demonstrates-ka-band-satellite-link-using-metamaterials-msa-t-antenna/>
- [2] ——. (2013) First-ever transmit/receive using metamaterial antenna. [Online]. Available: <http://www.kymetacorp.com/kymeta-rxtx-milestone/>
- [3] J. A. Bowers, R. A. Hyde, J. T. Kare, N. Kundtz, B. M. McWilliams, J. B. Pendry, D. Schurig, D. R. Smith, A. F. Starr, C. T. Tegreene, and L. L. Wood, “Metamaterial surfaces,” U.S. Patent 8 988 759, 2014.
- [4] M. Thevenot, C. Cheype, A. Reineix, and B. Jecko, “Directive photonic-bandgap antennas,” *IEEE Trans. Microw. Theory Techn.*, vol. 47, no. 11, pp. 2115–2122, 1999.
- [5] A. P. Feresidis and J. C. Vardaxoglou, “High gain planar antenna using optimised partially reflective surfaces,” *Microwaves, Antennas and Propagation, IEE Proceedings*, vol. 148, no. 6, pp. 345–350, 2001.
- [6] C. Serier, C. Cheype, R. Chantalat, M. Thèvenot, T. Monédière, A. Reineix, and B. Jecko, “1-D photonic bandgap resonator antenna,” *Microw. Opt. Tech. Lett.*, vol. 29, no. 5, pp. 312–315, 2001.

- [7] A. Weily, L. Horvath, K. Esselle, B. Sanders, and T. Bird, "A planar resonator antenna based on a woodpile EBG material," *IEEE Trans. Antennas Propag.*, vol. 53, no. 1, pp. 216–223, 2005.
- [8] A. R. Weily, K. P. Esselle, B. C. Sanders, and T. S. Bird, "High-gain 1D EBG resonator antenna," *Microw. Opt. Tech. Lett.*, vol. 47, no. 2, pp. 107–114, 2005.
- [9] A. P. Feresidis and J. C. Vardaxoglou, "A broadband high-gain resonant cavity antenna with single feed," in *Eur. Antennas Propag. Conf.*, 2006, pp. 1–5.
- [10] A. R. Weily, K. P. Esselle, T. S. Bird, and B. C. Sanders, "Dual resonator 1-D EBG antenna with slot array feed for improved radiation bandwidth," *Microwaves, Antennas & Propagation, IET*, vol. 1, no. 1, pp. 198–203, 2007.
- [11] Z. Liu, W. Zhang, D. Fu, Y. Gu, and Z. Ge, "Broadband Fabry-Perot resonator printed antennas using fss superstrate with dissimilar size," *Microw. Opt. Tech. Lett.*, vol. 50, no. 6, pp. 1623–1627, 2008.
- [12] G. Yuehe, K. P. Esselle, and T. S. Bird, "The use of simple thin partially reflective surfaces with positive reflection phase gradients to design wideband, low-profile EBG resonator antennas," *IEEE Trans. Antennas Propag.*, vol. 60, no. 2, pp. 743–750, 2012.
- [13] M. Al-Tarifi, D. Anagnostou, A. Amert, and K. Whites, "Bandwidth enhancement of the resonant cavity antenna by using two dielectric superstrates," *IEEE Trans. Antennas Propag.*, vol. 61, no. 4, pp. 1898–1908, 2013.
- [14] N. Wang, Q. Liu, C. Wu, L. Talbi, Q. Zeng, and J. Xu, "Wideband Fabry-Perot resonator antenna with two complementary FSS layers," *IEEE Trans. Antennas Propag.*, vol. 62, no. 5, pp. 2463–2471, May 2014.

- [15] R. M. Hashmi and K. P. Esselle, "A wideband EBG resonator antenna with an extremely small footprint area," *Microw. Opt. Tech. Lett.*, vol. 57, no. 7, pp. 1531–1535, 2015.
- [16] J. Joannopoulos, *Photonic Crystals: Molding The Flow Of Light*. Princeton University Press, 2008.
- [17] C. Elachi, "Waves in active and passive periodic structures: A review," *Proc. IEEE*, vol. 64, no. 12, pp. 1666–1698, Dec 1976.
- [18] V. Veselago, "The electrodynamics of substances with simultaneously negative values of permittivity and permeability," *Soviet Phys. Uspekhi*, vol. 10, pp. 509–514, 1968.
- [19] E. Yablonovitch, "Inhibited spontaneous emission in solid-state physics and electronics," *Phys. Rev. Lett.*, vol. 58, pp. 2059–2062, May 1987.
- [20] S. John, "Strong localization of photons in certain disordered dielectric superlattices," *Phys. Rev. Lett.*, vol. 58, pp. 2486–2489, Jun 1987.
- [21] J. B. Pendry, "Negative refraction makes a perfect lens," *Phys. Rev. Lett.*, vol. 85, no. 18, pp. 3966–3969, 2000.
- [22] J. B. Pendry, D. Schurig, and D. R. Smith, "Controlling electromagnetic fields," *Science*, vol. 312, no. 5781, pp. 1780–1782, 2006.
- [23] P. de Maagt, R. Gonzalo, Y. Vardaxoglou, and J.-M. Baracco, "Electromagnetic bandgap antennas and components for microwave and (sub)millimeter wave applications," *IEEE Trans. Antennas Propag.*, vol. 51, no. 10, pp. 2667–2677, 2003.

- [24] F. Yang and Y. Rahmat-Samii, *Electromagnetic Band Gap Structures in Antenna Engineering*, ser. The Cambridge RF and Microwave Engineering Series. Cambridge University Press, 2009.
- [25] I. Ederra, R. Gonzalo, B. Alderman, P. Huggard, B. de Hon, M. Van Beurden, A. Murk, L. Marchand, and P. de Maagt, “Sub-millimeter-wave imaging array at 500 GHz based on 3-D electromagnetic-bandgap material,” *IEEE Trans. Microw. Theory Techn.*, vol. 56, no. 11, pp. 2556–2565, Nov 2008.
- [26] N. Engheta and R. Ziolkowski, *Metamaterials: Physics and Engineering Explorations*. Wiley-Interscience, 2006.
- [27] C. Caloz and T. Itoh, *Electromagnetic Metamaterials: Transmission Line Theory and Microwave Applications*. Wiley, 2005.
- [28] K. Fuchi, J. Tang, B. Crowgey, A. Diaz, E. Rothwell, and R. Ouedraogo, “Origami tunable frequency selective surfaces,” *IEEE Antennas Wireless Propag. Lett.*, vol. 11, pp. 473–475, 2012.
- [29] Y. Dong and T. Itoh, “Promising future of metamaterials,” *IEEE Microw. Mag.*, vol. 13, no. 2, pp. 39–56, March 2012.
- [30] L. Brillouin, *Wave Propagation in Periodic Structures: Electric Filters and Crystal Lattices*. Dover Publications, 2003.
- [31] D. Sievenpiper, L. Zhang, R. F. J. Broas, N. Alexopolous, and E. Yablonovitch, “High-impedance electromagnetic surfaces with a forbidden frequency band,” *IEEE Trans. Microw. Theory Techn.*, vol. 47, no. 11, pp. 2059–2074, 1999.

- [32] D. Sievenpiper, J. H. Schaffner, H. J. Song, R. Y. Loo, and G. Tangonan, "Two-dimensional beam steering using an electrically tunable impedance surface," *IEEE Trans. Antennas Propag.*, vol. 51, no. 10, pp. 2713–2722, 2003.
- [33] M. Qiu and S. He, "High-directivity patch antenna with both photonic bandgap substrate and photonic bandgap cover," *Microw. Opt. Tech. Lett.*, vol. 30, no. 1, pp. 41–44, 2001.
- [34] R. Sauleau, P. Coquet, and T. Matsui, "Low-profile directive quasi-planar antennas based on millimetre wave Fabry-Perot cavities," *Microwaves, Antennas and Propagation, IEE Proceedings*, vol. 150, no. 4, pp. 274–278, Aug 2003.
- [35] H. Yang and N. Alexopoulos, "Gain enhancement methods for printed circuit antennas through multiple superstrates," *IEEE Trans. Antennas Propag.*, vol. 35, no. 7, pp. 860–863, 1987.
- [36] G. Trentini, "Partially reflecting sheet arrays," *IRE Trans. Antennas Propag.*, vol. 4, no. 4, pp. 666–671, 1956.
- [37] D. R. Jackson and N. Alexopoulos, "Gain enhancement methods for printed circuit antennas," *IEEE Trans. Antennas Propag.*, vol. 33, no. 9, pp. 976–987, 1985.
- [38] D. Jackson and A. Oliner, "A leaky-wave analysis of the high-gain printed antenna configuration," *IEEE Trans. Antennas Propag.*, vol. 36, no. 7, pp. 905–910, Jul 1988.
- [39] D. R. Jackson, A. A. Oliner, and A. Ip, "Leaky-wave propagation and radiation for a narrow-beam multiple-layer dielectric structure," *IEEE Trans. Antennas Propag.*, vol. 41, no. 3, pp. 344–348, 1993.

- [40] C. Cheype, C. Serier, M. Thevenot, T. Monediere, A. Reineix, and B. Jecko, "An electromagnetic bandgap resonator antenna," *IEEE Trans. Antennas Propag.*, vol. 50, no. 9, pp. 1285–1290, 2002.
- [41] A. R. Weily, K. Esselle, B. C. Sanders, and T. S. Bird, "Antennas based on 2-D and 3-D electromagnetic bandgap materials," in *IEEE Int. Antennas Prop. Symp.*, vol. 4, 2003, pp. 847–850 vol.4.
- [42] T. Akalin, J. Danglot, O. Vanbesien, and D. Lippens, "A highly directive dipole antenna embedded in a Fabry-Perot type cavity," *IEEE Microw. Wireless Compon. Lett.*, vol. 12, no. 2, pp. 48–50, 2002.
- [43] F. Zhu, Q. Lin, S. He, J. Hu, and Z. Ying, "A high directivity patch antenna using a PBG cover together with a PBG substrate," in *Int. Symp. Antennas Prop. Electromag. Theory*, 2003, pp. 92–95.
- [44] Y. J. Lee, J. Yeo, K. D. Ko, R. Mittra, Y. Lee, and W. S. Park, "A novel design technique for control of defect frequencies of an electromagnetic bandgap (EBG) superstrate for dual-band directivity enhancement," *Microw. Opt. Tech. Lett.*, vol. 42, no. 1, pp. 25–31, 2004.
- [45] Y. J. Lee, J. Yeo, R. Mittra, and W. S. Park, "Design of a high-directivity electromagnetic band gap (EBG) resonator antenna using a frequency-selective surface (FSS) superstrate," *Microw. Opt. Tech. Lett.*, vol. 43, no. 6, pp. 462–467, 2004.
- [46] L. Leger, T. Monediere, M. Thevenot, and B. Jecko, "Multifrequency and beam steered electromagnetic band gap antennas," in *IEEE Int. Antennas Prop. Symp.*, vol. 2, 2004, pp. 1151–1154.
- [47] R. Gardelli, M. Albani, and F. Capolino, "EBG superstrates for dual polarized sparse arrays," in *IEEE Int. Antennas Prop. Symp.*, vol. 2, 2005, pp. 586–589.

- [48] B. Jecko, T. Monediere, and L. Leger, "High gain EBG resonator antenna," in *IEEE Int. Applied Electromag. Comm. Conf.*, 2005, pp. 1–3.
- [49] L. Leger, R. Granger, M. Thevenot, T. Monediere, and B. Jecko, "Multi-frequency dielectric EBG antenna," *Microw. Opt. Tech. Lett.*, vol. 40, pp. 420–423, 2005.
- [50] L. Moustafa and B. Jecko, "Design of a wideband highly directive EBG antenna using double-layer frequency selective surfaces and multifeed technique for application in the Ku-band," *IEEE Antennas Wireless Propag. Lett.*, vol. 9, pp. 342–346, 2010.
- [51] R. M. Hashmi, B. A. Zeb, and K. P. Esselle, "Wideband high-gain EBG resonator antenna employing an unprinted composite superstrate," in *IEEE Int. Antennas Prop. Symp.* IEEE, 2013.
- [52] Y. J. Lee, J. Yeo, R. Mittra, and W. S. Park, "Application of electromagnetic bandgap (EBG) superstrates with controllable defects for a class of patch antennas as spatial angular filters," *IEEE Trans. Antennas Propag.*, vol. 53, no. 1, pp. 224–235, 2005.
- [53] A. R. Weily, K. P. Esselle, T. S. Bird, and B. C. Sanders, "High gain circularly polarised 1-D EBG resonator antenna," *Elect. Lett.*, vol. 42, no. 18, pp. 1012–1013, 2006.
- [54] S. Muhammad, R. Sauleau, and H. Legay, "Small-size shielded metallic stacked Fabry-Perot cavity antennas with large bandwidth for space applications," *IEEE Trans. Antennas Propag.*, vol. 60, no. 2, pp. 792–802, 2012.
- [55] D. Kim, J. Ju, and J. Choi, "A mobile communication base station antenna using a genetic algorithm based Fabry-Perot resonance optimization," *IEEE Trans. Antennas Propag.*, vol. 60, no. 2, pp. 1053–1058, 2012.

- [56] R. M. Hashmi, K. P. Esselle, and S. G. Hay, "Engineering defect-modes in unprinted EBG structures to design high-gain broadband antennas," in *Thirteenth Australian Symp. Ant.* CSIRO, 2013.
- [57] R. M. Hashmi, B. A. Zeb, K. P. Esselle, and S. G. Hay, "Effect of truncating the superstructures in broadband fabry-perotot cavity antennas," in *Int. Microw. Optoelect. Conf.* IEEE/MTT, 2013.
- [58] A. R. Weily, T. S. Bird, and Y. J. Guo, "A reconfigurable high-gain partially reflecting surface antenna," *IEEE Trans. Antennas Propag.*, vol. 56, no. 11, pp. 3382–3390, 2008.
- [59] B. Zeb, Y. Ge, K. Esselle, Z. Sun, and M. Tobar, "A simple dual-band electromagnetic band gap resonator antenna based on inverted reflection phase gradient," *IEEE Trans. Antennas Propag.*, vol. 60, no. 10, pp. 4522–4529, Oct 2012.
- [60] B. Zeb, Y. Ge, K. Esselle, and M. Tobar, "A simple EBG resonator antenna for dual-polarized, dual-band wireless links," in *Asia-Pacific Microw. Conf.*, 2011, pp. 433–436.
- [61] A. Ourir, S. N. Burokur, and A. D. Lustrac, "Phase-varying metamaterial for compact steerable directive antenna," *Elect. Lett.*, vol. 43, no. 9, pp. 493–494, 2007.
- [62] H. Nakano, J. Miyake, Y. Oishi, and J. Yamauchi, "Radiation from antenna systems with homogeneous and inhomogeneous loops," in *IEEE Int. Antennas Prop. Symp.*, 2011, pp. 2239–2241.
- [63] F. Costa and A. Monorchio, "Design of subwavelength tunable and steerable Fabry-Perot/leaky wave antennas," *Prog. Electromag. Research*, vol. 111, pp. 476–481, 2011.

- [64] A. Edalati and T. Denidni, "Reconfigurable beamwidth antenna based on active partially reflective surfaces," *IEEE Antennas Wireless Propag. Lett.*, vol. 8, pp. 1087–1090, 2009.
- [65] L. Moustafa and B. Jecko, "Broadband high gain compact resonator antennas using combined FSS," in *IEEE Int. Antennas Prop. Symp.*, 2008, pp. 1–4.
- [66] —, "EBG structure with wide defect band for broadband cavity antenna applications," *IEEE Antennas Wireless Propag. Lett.*, vol. 7, pp. 693–696, 2008.
- [67] Y. F. Lu and Y. C. Lin, "Design and implementation of broadband partially reflective surface antenna," in *IEEE Int. Antennas Prop. Symp.*, 2011, pp. 2250–2253.
- [68] M. A. Al-Tarifi, D. E. Anagnostou, A. K. Amert, and K. W. Whites, "Bandwidth enhancement of the cavity resonance antenna (CRA) using multiple dielectric superstrate layers," in *IEEE MTT-S Int. Microw. Symp. Dig.*, 2011, pp. 1–4.
- [69] H. Yi, S.-W. Qu, K. B. Ng, and C. Chan, "3-D printed discrete dielectric lens antenna with matching layer," in *Int. Symp. Antennas Prop.*, 2014, pp. 115–116.
- [70] R. M. Hashmi, K. P. Esselle, and S. G. Hay, "Directive beaming with lens-like superstates for low profile Fabry-Perot cavity antennas," in *Intl. Symp. Antenna Tech. Applied Electromag.*, July 2014, pp. 1–2.
- [71] —, "Achieving high directivity-bandwidth through flat GRIN superstrates in Fabry-Perot cavity antennas," in *IEEE Int. Antennas Prop. Symp.*, July 2014, pp. 1748–1749.
- [72] R. Hashmi, B. Zeb, and K. Esselle, "Wideband high-gain EBG resonator antennas with small footprints and all-dielectric superstructures," *IEEE Trans. Antennas Propag.*, vol. 62, no. 6, pp. 2970–2977, June 2014.

- [73] T. Zhao, D. R. Jackson, and J. T. Williams, “2-D periodic leaky-wave antennas—part II: slot design,” *IEEE Trans. Antennas Propag.*, vol. 53, no. 11, pp. 3515–3524, 2005.
- [74] Z. C. Ge, W. X. Zhang, Z. G. Liu, and Y. Y. Gu, “Broadband and high-gain printed antennas constructed from Fabry-Perot resonator structure using EBG or FSS cover,” *Microw. Opt. Tech. Lett.*, vol. 48, no. 7, pp. 1272–1274, 2006.
- [75] Y. Ge and K. P. Esselle, “A resonant cavity antenna based on an optimized thin superstrate,” *Microw. Opt. Tech. Lett.*, vol. 50, no. 12, pp. 3057–3059, 2008.
- [76] K. Konstantinidis, A. Feresidis, and P. Hall, “Dual subwavelength Fabry-Perot cavities for broadband highly directive antennas,” *IEEE Antennas Wireless Propag. Lett.*, vol. 13, pp. 1184–1186, 2014.
- [77] L. C. Kretly and A. M. P. A. Silva, “The influence of the height variation on the frequency bandgap in an amc, artificial magnetic conductor, for wireless applications: an EM experimental design approach,” in *Int. Microw. Optoelect. Conf.*, vol. 1, 2003, pp. 219–223.
- [78] L. Yading, “Investigation of minimum cavity height of small EBG resonator antennas for maximum directivity,” in *Asia-Pacific Microw. Conf.*, 2009, pp. 2687–2690.
- [79] L. Zhen Guo, “Design of broadband Fabry-Perot resonator antenna using quasi-periodic structure,” in *Int. Workshop on Metamaterials*, 2008, pp. 259–262.
- [80] L. Zhen Guo, R. Qiang, and Z. xin Cao, “A novel broadband Fabry-Perot resonator antenna with gradient index metamaterial superstrate,” in *Proc. IEEE Int. Antennas Prop. Symp.*, July 2010, pp. 1–4.

- [81] B. A. Zeb, R. M. Hashmi, K. P. Esselle, and Y. Ge, "The use of reflection and transmission models to design wideband and dual-band Fabry-Perot cavity antennas (invited paper)," in *URSI Int. Symp. on Electromagnetic Theory*, 2013, pp. 1084–1087.
- [82] B. A. Zeb, K. P. Esselle, and R. M. Hashmi, "Computational models for bandwidth enhancement of electromagnetic bandgap (EBG) resonator antennas and their limitations," in *Int. Comp. Electromag. Conf.*, 2015, pp. 19–21.
- [83] N. Alexopoulos and D. R. Jackson, "Fundamental superstrate (cover) effects on printed circuit antennas," *IEEE Trans. Antennas Propag.*, vol. 32, no. 8, pp. 807–816, Aug 1984.
- [84] G. Lovat, P. Burghignoli, and D. Jackson, "Fundamental properties and optimization of broadside radiation from uniform leaky-wave antennas," *IEEE Trans. Antennas Propag.*, vol. 54, no. 5, pp. 1442–1452, May 2006.
- [85] H. Boutayeb, K. Mahdjoubi, A. C. Tarot, and T. A. Denidni, "Directivity of an antenna embedded inside a Fabry-Perot cavity: Analysis and design," *Microw. Opt. Tech. Lett.*, vol. 48, no. 1, pp. 12–17, 2006.
- [86] Z.-G. Liu, Z.-C. Ge, and X.-Y. Chen, "Research progress on Fabry-Perot resonator antenna," *Science A*, vol. 10, no. 4, pp. 583–588, 2009.
- [87] Z. G. Liu, "Quasi-periodic structure application in Fabry-Perot resonator printed antenna," in *Asia-Pacific Microw. Conf.*, 2008, pp. 1–4.
- [88] T. Zhao, D. R. Jackson, J. T. Williams, H.-Y. D. Yang, and A. A. Oliner, "2-D periodic leaky-wave antennas-part I: metal patch design," *IEEE Trans. Antennas Propag.*, vol. 53, no. 11, pp. 3505–3514, 2005.

- [89] R. Gardelli, M. Albani, and F. Capolino, "Array thinning by using antennas in a Fabry-Perot cavity for gain enhancement," *IEEE Trans. Antennas Propag.*, vol. 54, no. 7, pp. 1979–1990, 2006.
- [90] S. A. Hosseini, F. Capolino, F. De Flaviis, P. Burghignoli, G. Lovat, and D. R. Jackson, "Improved method to estimate the 3dB power bandwidth of a Fabry-Perot cavity antenna covered by a thin frequency selective surface," in *IEEE Int. Antennas Prop. Symp.*, 2011, pp. 1281–1284.
- [91] H. Boutayeb and T. Denidni, "Internally excited Fabry-Perot type cavity: Power normalization and directivity evaluation," *IEEE Antennas Wireless Propag. Lett.*, vol. 5, no. 1, pp. 159–162, 2006.
- [92] D. R. Jackson, P. Burghignoli, G. Lovat, F. Capolino, C. Ji, D. R. Wilton, and A. A. Oliner, "The fundamental physics of directive beaming at microwave and optical frequencies and the role of leaky waves," *Proc. IEEE*, vol. 99, no. 10, pp. 1780–1805, 2011.
- [93] G. Lovat, P. Burghignoli, F. Capolino, and D. Jackson, "Bandwidth analysis of highly-directive planar radiators based on partially-reflecting surfaces," in *Eur. Antennas Propag. Conf.*, Nov 2006, pp. 1–6.
- [94] A. Ip and D. Jackson, "Radiation from cylindrical leaky waves," *IEEE Trans. Antennas Propag.*, vol. 38, no. 4, pp. 482–488, 1990.
- [95] A. Ip, D. Jackson, and A. Oliner, "An improved calculation procedure for the radiation pattern of a cylindrical leaky-wave antenna of finite size," *IEEE Trans. Antennas Propag.*, vol. 40, no. 1, pp. 19–24, 1992.

- [96] R. M. Hashmi, B. A. Zeb, and K. P. Esselle, "Effective techniques for extending the directivity-bandwidth of resonant cavity antennas," in *Int. Workshop Antennas Tech.*, March 2014, pp. 270–272.
- [97] R. M. Hashmi, B. A. Zeb, K. P. Esselle, and S. G. Hay, "EBG resonator antennas with high aperture efficiencies," in *Int. Conf. Elect. Adv. App. (ICEAA)*, 2014.
- [98] —, "A simple resonant cavity antenna with improved directivity-bandwidth performance for high-capacity wireless data links," in *IEEE Int. Applied Electromag. Comm. Conf.*, 2013.
- [99] L. Yading and K. P. Esselle, "A height-reduced, slot-array-fed EBG resonator antenna with high gain and large bandwidth," in *IEEE Int. Antennas Prop. Symp.*, 2007, pp. 4417–4420.
- [100] M. S. Toubet, R. Chantalat, M. Thevenot, T. Monediere, and B. Jecko, "Conception of a low-profile and high-gain EBG resonator antenna with wide bandwidth," in *Int. Workshop Antennas Tech.*, 2010, pp. 1–4.
- [101] M. S. Toubet, M. Hajj, R. Chantalat, E. Arnaud, B. Jecko, T. Monediere, Z. Hongjiang, and J. Diot, "Wide bandwidth, high-gain, and low-profile EBG prototype for high power applications," *IEEE Antennas Wireless Propag. Lett.*, vol. 10, pp. 1362–1365, 2011.
- [102] Australian Communications and Media Authority. (2013) Wireless access services future needs. [Online]. Available: <http://www.acma.gov.au/Industry/Spectrum/Five-Year-Spectrum-Outlook/Future-spectrum-needs/wireless-access-services-future-needs-fyso-59>
- [103] F. Yang and Y. Rahmat Samii, *Electromagnetic Band Gap Structures in Antenna Engineering*. Cambridge University Press, 2009.

- [104] N. Guerin, S. Enoch, G. Tayeb, P. Sabouroux, P. Vincent, and H. Legay, "A metallic Fabry-Perot directive antenna," *IEEE Trans. Antennas Propag.*, vol. 54, no. 1, pp. 220–224, 2006.
- [105] G. Yuehe, K. P. Esselle, and H. Yang, "Design of low-profile high-gain EBG resonator antennas using a genetic algorithm," *IEEE Antennas Wireless Propag. Lett.*, vol. 6, pp. 480–483, 2007.
- [106] Y. Ge and K. P. Esselle, "Designing high gain microwave antennas by optimising a FSS superstrate," in *Eur. Microw. Conf.*, 2007, pp. 412–415.
- [107] A. Foroozesh and L. Shafai, "Investigation into the effects of the patch-type FSS superstrate on the high-gain cavity resonance antenna design," *IEEE Trans. Antennas Propag.*, vol. 58, no. 2, pp. 258–270, 2010.
- [108] A. Feresidis, G. Goussetis, S. Wang, and J. Vardaxoglou, "Artificial magnetic conductor surfaces and their application to low-profile high-gain planar antennas," *IEEE Trans. Antennas Propag.*, vol. 53, no. 1, pp. 209–215, Jan 2005.
- [109] L. Zhou, H. Li, Y. Qin, Z. Wei, and C. Chan, "Directive emission from subwavelength metamaterial-based cavities," *Appl. Phys. Lett.*, vol. 86, p. 1, 2005.
- [110] H. Yi, S.-W. Qu, K. B. Ng, and C. H. Chan, "3-D printed discrete dielectric lens antenna with matching layer," in *Intl. Symp Antennas Propag.*, 2014, pp. 115–116.
- [111] R. Yang, W. Tang, and Y. Hao, "Broadband dielectric zone plate antenna from transformation electromagnetics," in *Eur. Antennas Propag. Conf.*, 2011, pp. 3463–3465.

- [112] W. X. Jiang, W. X. Tang, and T.-J. Cui, "Transformation optics and applications in microwave frequencies (invited paper)," *Progress In Electromagnetics Research*, vol. 149, pp. 251–273, 2014.
- [113] H. X. Yang, Z. X. Ying, Y. Yan, M. A. H. Feng, and T.-J. Cui, "Three-dimensional large-aperture lens antennas with gradient refractive index," *Science China*, vol. 56, no. 12, pp. 120–140, 2013.
- [114] H. F. Ma, B. G. Cai, T. X. Zhang, Y. Yang, W. X. Jiang, and T. J. Cui, "Three-dimensional gradient-index materials and their applications in microwave lens antennas," *IEEE Trans. Antennas Propag.*, vol. 61, no. 5, pp. 2561–2569, 2013.
- [115] C. Mateo-Segura, A. Dyke, H. Dyke, S. Haq, and Y. Hao, "Flat luneburg lens via transformation optics for directive antenna applications," *IEEE Trans. Antennas Propag.*, vol. 62, no. 4, pp. 1945–1953, 2014.
- [116] L. Moustafa and B. Jecko, "EBG structure with wide defect band for broadband cavity antenna applications," *IEEE Antennas Wireless Propag. Lett.*, vol. 7, pp. 693–696, 2008.
- [117] M. A. Al-Tarifi, A. K. Amert, D. Anagnostou, and K. W. Whites, "Application of a dielectric puck for a high gain-bandwidth resonant cavity antenna," in *IEEE Int. Antennas Prop. Symp.*, July 2012, pp. 1–2.
- [118] T. Bird and C. Granet, "Optimization of profiles of rectangular horns for high efficiency," *Antennas and Propagation, IEEE Transactions on*, vol. 55, no. 9, pp. 2480–2488, Sept 2007.
- [119] Z. Ma and G. Vandenbosch, "Low-cost wideband microstrip arrays with high aperture efficiency," *IEEE Trans. Antennas Propag.*, vol. 60, no. 6, pp. 3028–3034, 2012.

- [120] N. Zhu and R. Ziolkowski, “Photoconductive THz antenna designs with high radiation efficiency, high directivity, and high aperture efficiency,” *IEEE Trans. THz Sci. Technol.*, vol. 3, no. 6, pp. 721–730, 2013.
- [121] K. Konstantinidis, A. Feresidis, and P. Hall, “Broadband sub-wavelength profile high-gain antennas based on multi-layer metasurfaces,” *IEEE Trans. Antennas Propag.*, vol. 63, no. 1, pp. 423–427, Jan 2015.
- [122] S. Kabiri, S. A. Hosseini, F. Capolino, and F. De Flaviis, “Gain-bandwidth enhancement of 60GHz single-layer Fabry-Perot cavity antennas using sparse-array,” in *IEEE Int. Antennas Prop. Symp.*, 2014, pp. 739–740.
- [123] S. Hosseini, F. Capolino, and F. De Flaviis, “Single-feed highly-directive Fabry-Perot cavity antenna for 60GHz wireless systems: Design and fabrication,” in *IEEE Int. Antennas Prog. Symp.*, 2010, pp. 1–4.
- [124] Y. Ge and K. P. Esselle, “A resonant cavity antenna based on an optimized thin superstrate,” *Microw. Opt. Tech. Lett.*, vol. 50, no. 12, pp. 3057–3059, 2008.
- [125] —, “Designing high gain microwave antennas by optimising a FSS superstrate,” in *Eur. Microw. Conf.*, 2007, pp. 412–415.